

Technische Universität München
Fakultät für Maschinenwesen
Lehrstuhl für Mikrotechnik und Medizingerätetechnik
Univ.-Prof. Dr. Tim C. Lüth

Diplomarbeit

Interactive Graph-Based Segmentation of the Rectosigmoid Colon in MRI Data for Image Guided Gynecological Brachytherapy

Tobias Lüddemann

Matr.-Nr.: 3090720

Betreuender Hochschullehrer:	Univ.-Prof. Dr. Tim C. Lüth
Betreuer:	Dipl.-Inf. Jan Gumprecht, Dr. Dr. Jan Egger
Ausgegeben am:	16.11.2013
Abgegeben am:	15.05.2013

Ehrenwörtliche Erklärung

Ich erkläre hiermit ehrenwörtlich, dass ich die vorliegende Arbeit selbstständig und ohne Benutzung anderer als der angegebenen Hilfsmittel angefertigt habe; die aus fremden Quellen (einschließlich elektronischer Quellen) direkt oder indirekt übernommenen Gedanken sind ausnahmslos als solche kenntlich gemacht.

Garching bei München, den 15.05.2013

Tobias Lüddemann

Abstract

Among all types of cancer, gynecological malignancies belong to the 4th most frequent type of cancer among women. Besides chemotherapy and external beam radiation, brachytherapy is the standard procedure for the treatment of these malignancies. In the progress of treatment planning, localization of the tumor as the target volume and adjacent organs at risk by segmentation is crucial to accomplish an optimal radiation distribution to the tumor while simultaneously preserving healthy tissue. Segmentation is performed manually and represents a time-consuming task in clinical daily routine. This thesis focuses on the segmentation of the rectum/sigmoid colon as an Organ-At-Risk in gynecological brachytherapy. The proposed segmentation method uses an interactive, graph-based segmentation scheme with a user-defined template. In summary, the scheme creates a directed two dimensional graph, followed by the minimal cost closed set computation on the graph, resulting in an outlining of the rectum. The graph's outline is dynamically adapted to the last calculated cut. Evaluation was performed by comparing manual segmentations of the rectum/sigmoid colon to results achieved with the proposed method. The comparison of the algorithmic to manual result yielded a Dice Similarity Coefficient value of 83.85 ± 4.08 , in comparison to $83.97 \pm 8.08\%$ for the comparison of two manual segmentations of the same physician. Utilizing the proposed methodology resulted in a median time of 128 seconds per data set, compared to 300 seconds needed for pure manual segmentation.

Zusammenfassung

Unter allen Krebsarten sind gynäkologische Tumore die vierthäufigste Art karzinogener Krankheiten. Neben Chemotherapie und externer Bestrahlung ist die Behandlung durch Brachytherapie eine Standardbehandlung für Krankheiten dieser Art. Im Verlauf der Therapieplanung ist es nötig die relative Lage des Tumors und benachbarter Organe durch Segmentierung zu erfassen um die verabreichte Strahlung möglichst genau planen zu können, wobei der Tumor zerstört sowie umliegende Organe geschont werden sollen. Die Segmentierung wird manuell durchgeführt und stellt einen höchst zeitaufwendigen Schritt im Verlauf der Therapieplanung da. Diese Arbeit konzentriert sich auf die Segmentierung des Rektum/Sigmoid colons als ein Risikoorgan in der gynäkologischen Brachytherapie und beschreibt einen interaktiven, graph-basierten Ansatz aufgebaut auf einer benutzerdefinierten Schablone. Es wird dabei ein zwei dimensionaler Graph aufgebaut, worauf die Berechnung eines minimalen Schnitts in der Umrandung des Rektums resultiert. Die Form des Graphen wird dabei dynamisch an die Form des Schnitts angepasst. Der präsentierte Algorithmus wurde durch den Vergleich manueller und algorithmischer Segmentierungen evaluiert. Für den Vergleich zwischen Algorithmus und Manuell wurde ein mittlerer Dice Similarity Coefficient von $83.85 \pm 4.08\%$ erreicht. Für den Vergleich zweier manueller Segmentierungen wurde ein mittlerer Dice Similarity Coefficient von $83.97 \pm 8.08\%$ ermittelt. Unter Verwendung des Algorithmus konnte eine Zeit (median) von 128 Sekunden pro Datensatz erreicht werden im Vergleich zu 300 Sekunden für eine manuelle Segmentierung.

Acknowledgement

This thesis concludes my studies of mechanical engineering at the Technical University of Munich (TUM), Munich, Germany. It was partly conducted at the Surgical Planning Laboratory (SPL) of Brigham & Women's Hospital, a teaching affiliate of Harvard Medical School in Boston, USA and supervised by the Institute of Micro Technology and Medical Device Technology (MiMed) of TUM.

First, I would like to thank Prof. Tim Lüth of MiMed at TUM and Prof. Ron Kikinis of the SPL at Brigham & Women's Hospital for their openness and the possibility they gave me to conduct this thesis and take part in cutting-edge medical imaging research.

Above all I am deeply thankful for the supervision of Jan Egger at the SPL, his ongoing trust and the knowledge he shared with me. Moreover, I am especially thankful for his guidance through this work beyond my time at the SPL. Without his enthusiasm and willingness this thesis would have not been possible to conduct partly in Boston and partly in Munich. Additionally, I am thankful for the support and advice he offered me beyond all university obligations. I also want to thank Jan Gumprecht of MiMed for his openness to supervise this thesis on behalf of TUM and the help and trust I received in all situations.

I am also greatly indebted to Tina Kapur, who not only provided me with a warm welcome to the SPL and the introduction to her research group, but also for her continuous effort to create a stimulating research environment. I also want to thank Akila Viswanathan for the publication of her gynecological MRI data sets, which laid the groundwork for this thesis.

I would also like to thank all other members of the SPL who make the creative and rich environment I found unforgettable to work in, especially Neha Agrawal for her help in all medical questions but also Steve Piper, Guillaume Pernelle, Alireza Mehrtaash, Rie Oyama, Atsushi Yamada, Sonia Pujol, Junichi Tokuda and Tobias Penzkofer.

Finally, I would like to thank my friends and family for their relentless support. I am especially grateful to my parents for enabling me to worriless conduct and finish my studies. I am also indebted to my brother Markus and his talent in drawing who went through the trouble and provided me with the highly artistic drawings of the anatomical structures of the female pelvis. Above all I am thankful to my girlfriend Juri and her continuous love and patience in all situations we have been through over the last years.

Contents

Ehrenwörtliche Erklärung	II
Abstract	III
Zusammenfassung	III
Acknowledgement	IV
Contents	5
1 Introduction	7
2 Preliminaries	9
2.1 Problem Statement	9
2.1.1 Anatomy of the Female Pelvis	10
2.1.2 Image Guided Interstitial Brachytherapy	12
2.1.3 Treatment Planning	15
2.1.4 MRI Depiction of the Lesser Female Pelvis & Rectum/Sigmoid Colon	18
2.2 State of Clinical Applications	22
2.2.1 Manual Segmentation	22
2.2.2 Commercial Segmentation Tools	24
2.3 State of Research	25
2.3.1 Region Growing	25
2.3.2 Active Appearance Models	29
2.3.3 Active Contours	30
2.3.4 Graph Cuts	31
2.3.5 Interactive Methodologies	32
2.4 Overview	34
3 Interactive Graph-Based Segmentation	39
3.1 Task Definition	39
3.2 Expected Advantages and Characteristics	39
3.3 Solution Structure	40
3.4 Solution Processes	41
3.4.1 User Workflow	41
3.4.2 System Overview	45
3.4.3 Network	46
3.4.4 InteractiveCut Module	49
3.4.5 Graph Networks	51
3.4.6 Graph-Cut Implementation	56
3.5 Distinguishing Characteristics	71
4 Evaluation	73
4.1 Approach	73
4.2 Experiments	77
4.2.1 Rectum/Sigmoid Colon	79
4.2.2 Bladder	83
4.3 Discussion	86

5 Conclusion.....	89
Figures	90
Glossary.....	95
Publication.....	96
Bibliography.....	97

1 Introduction

It is estimated that in 2012 cancer related illnesses will account for the death of approximately 577,190 Americans. Cancer is thus the second most common cause of death in the United States only exceeded by heart disease which accounts for almost 1 of 4 deaths. Numbers of the National Institutes of Health (NIH) state overall costs of \$226.8 billion for cancer related illnesses in 2007. Thereby \$103.8 billion account for direct medical treatment expenses and \$123.0 billion for indirect cost due to lost productivity (Siegel, 2012).

Additionally, the frequency of cancer related illnesses increases over proportionally since the beginning of the last century and continuously affects all age groups (Kauffmann et al., 2006). Despite these facts it was observed that the 5-year relative survival rate among all types of cancers treated between 1975 and 1977 increased from 49% to 67% in the years from 2001 to 2007 (Siegel, 2012). These numbers clearly indicate the need for improved treatment strategies and technologies but they also show that medical research efforts put into the field can make an impact on patient's lives and the overall socioeconomic costs caused by tumor related illnesses.

In the progress of cancer treatment 60-70% of all patients will at one point in time come in contact with radiotherapy procedures (Kauffmann et al., 2006). Besides the acquisition of medical images themselves, one key step in radiotherapy treatment is computer assisted segmentation of those acquired medical images. Thereby, valuable information about the acquired images is retrieved by separating them into meaningful anatomical regions (Babalola et al., 2008). This step is a crucial requirement for every computer-assisted radiotherapy treatment plan which the optimization of dose distribution regarding the tumor and organs-at-risk (OAR) strongly depend on. Without exact knowledge about the location of the tumor and adjacent organs, precise local tumor control with simultaneous sparing of healthy tissues cannot be achieved (Lechsel, 2007).

The technological progress in medical imaging technologies over the last decades led to a broader use into fields such as diagnosis, treatment planning and clinical studies. At the same time the technology enabled the acquisition of large amounts of image data in short periods of time. This trend causes the amount of data acquired consistently exceeding the amount of data used in succeeding treatment procedures. Because manual segmentation is until today regarded as gold standard, not all theoretically available information can be retrieved due to limited human capacities (Babalola et al., 2008). Furthermore, this practice is time consuming and not resource efficient and therefore demands the development of reliable computer assisted systems to support physicians in their evaluation of medical image data (Lechsel, 2007).

Various fully automatic segmentation methods have been proposed and are being constantly improved. However few of these automatic analysis tools can guarantee robust results or are in clinical usage (Birkbeck et al., 2009, Vezhnevets and Konouchine, 2005). Although commercial tools can exhibit sufficient results for the prostate or urinary bladder, the rectum is still problem prone and needs further improvements (Haas et al., 2008) (Huyskens et al., 2008).

As none of the current fully automatic approaches provides sufficient results for the rectum and sigmoid colon, manual refinement of the computed segmentation is desirable and the

motivation for the development of interactive segmentation approaches (Egger et al., 2012b). They can speed up the segmentation process but yet give the physician enough control over the algorithm to directly influence and improve the segmentation result (Birkbeck et al., 2009).

Gynecological malignancies which include endometrial, vaginal/vulvar and cervical cancers represent the 4th most frequent type of cancer among women and a major cause of death around the world (Siegel, 2012). The standard procedure for primary or recurrent treatments of these types of cancer consists of external-beam radiation (EBR) followed by brachytherapy. During the brachytherapy procedure needle like catheters carrying a radiation source are inserted into the patient in close proximity to the tumor in order to directly irradiate the malignant tissue (Viswanathan and Erickson, 2010). A crucial step in planning the applied amount and distribution of radiation is the segmentation of the tumor and adjacent organs-at-risk potentially exposed to radiation. The most common OAR segmented in gynecological brachytherapy include the urinary bladder and the rectum/sigmoid colon (Viswanathan, 2011).

This thesis focuses on the segmentation of the rectum/sigmoid colon as an organ-at-risk in the context of MR images for Image Guided Gynecological Brachytherapy. The rectum/sigmoid colon has due to its mostly inhomogeneous appearance proven to be challenging for current segmentation tools (Haas et al., 2008) (Egger et al., 2012a). A novel interactive segmentation algorithm for the segmentation of the rectum/sigmoid colon based on graph theory is presented.

2 Preliminaries

2.1 Problem Statement

In the course of Image Guided Interstitial Gynecological Brachytherapy a crucial preliminary step to treatment is the segmentation of the tumor as the target-volume (TV) and adjacent organs potentially exposed to radiation as the organs-at-risk (Viswanathan, 2011). With the 3D information about the tumor and OARs, the positioning of each interstitial needle are controlled and the radiation loading and dwell time of each needle is determined in order to optimize the dose distribution applied to the tumor, while sparing the OARs from radiation as much as possible. This delineation of anatomical structures is mostly conducted manually by a physician by drawing outlines of the structure on a slice by slice basis and represents a time-consuming task in the progress of planning radiological treatments (Bille and Schlegel, 2002, Pasquier et al., 2007).

In general cases the performing physician might have to outline several structures in more than 80 slices (Bille and Schlegel, 2002). Regarding the specific given problem of treatment planning in Image Guided Brachytherapy (IGBT) at Brigham & Women's Hospital (BWH) in Boston, USA, manual segmentation of the rectum/sigmoid colon by outlining the object contour has to be conducted in more than a dozen slices and is a tedious task.

Over the last decades various fully automatic segmentation methods have been proposed to support this segmentation process. However, the development of fully automatic segmentation tools remains problematic due to variability in pelvic organ shape and poor soft tissue depiction. None of these automatic analysis tools can guarantee robust results or achieved clinical approval. Moreover, they mostly lack necessary intervention methodologies and provide little final control by the medical doctor over the segmentation (Birkbeck et al., 2009, Vezhnevets and Konouchine, 2005), (Pasquier et al., 2007). As none of the current fully automatic approaches provides sufficient results, manual refinement of the computed segmentation is desirable and the motivation for the development of interactive segmentation approaches (Egger et al., 2012b). In summary, they can speed up the segmentation process yet give the physician enough control over the algorithm to directly influence and improve the segmentation result (Birkbeck et al., 2009).

A major research effort was being put into brain tumor segmentation (e.g. (Corso et al., 2008), (Wels et al., 2008), (Khotanloua et al., 2009)), but only some research effort has been focused on segmentation algorithms for pelvic structures regarding the urinary bladder, rectum/sigmoid colon or malignant tumor volumes. Most of these approaches were either fully automatic or applied to Computer Tomography images (e.g. (Pasquier et al., 2007), (Pekar et al., 2004), (Mazonakis et al., 2001)). While both CT and MRI are used for image guided radiotherapy of gynecological malignancies, CT represents the standard imaging technology for treatment with external radiation therapy (EBRT), MRI the technology widely used for image guided brachytherapy (Viswanathan, 2011).

Conditioned by the lack of methodologies for MR-guided IGBT applications, the standard of time-consuming manual segmentations and problems of fully automatic tools, there is a strong desire for the development of interactive segmentation algorithms to assist physicians in the course of interstitial gynecological radiotherapy treatment planning.

2.1.1 Anatomy of the Female Pelvis

This chapter generally follows the structure given in (Drake et al., 2005), (Greene et al., 2006) and (Schünke et al., 2005) and provides an overview of the anatomical structures of the female pelvis which will be used in the following chapters.

In human anatomy the pelvis is defined by the pelvic bones and the terminal parts of the vertebral column. It is generally regarded as two separate regions, the superiorly lying false pelvis (greater pelvis) which is considered part of the abdomen and the inferiorly lying true pelvis (lesser pelvis) which is associated with the pelvic bones and lower vertebral column (sacrum and coccyx). The pelvic cavity is a space enclosed by the pelvic girdle and the pelvic brim as well as the pelvic inlet and the pelvic floor. It contains anatomical structures of the urinary, gastrointestinal and reproductive system (see Figure 1).

The urinary system is located anteriorly, the reproductive system along the midline and the rectum posteriorly. The bladder and the urethra represent the urinary system.

Beginning caudal, the reproductive system consists of the vagina and uterus as well as two pairs of uterine tubes and ovaries.

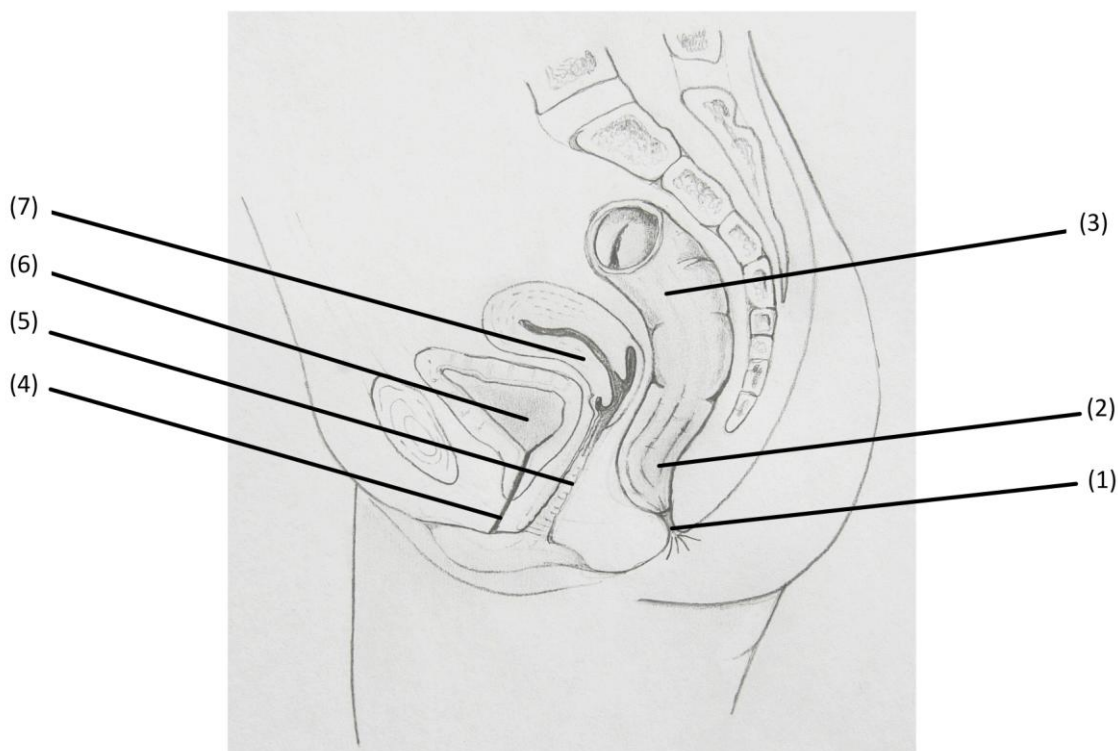


Figure 1: Illustration of the female pelvis: (1) anal canal (2) rectum, (3) sigmoid colon, (4) urethra, (5) vagina, (6) bladder, (7) uterus. Illustration based on (Drake et al., 2005)

The gastrointestinal system begins with the stomach, continues with the intestine and ends caudal with the penetration of the floor of the pelvic cavity by the anal aperture. The intestine consists of the small and large intestine, whereby the small intestine represents the longest part of the gastrointestinal tract.

In the small intestine most of the digestion and absorption of food takes place. Its average length varies between 6m - 7m in adults, its diameter between 2.5 – 3.0cm. It can be further divided into the anatomical structures of the duodenum, the jejunum and the ileum.

Following the small intestine continues the large intestine. It extends from the end of the ileum to the anal canal and is approximately 1.5m in length and approximately 3.5cm in diameter. Its main function comprises the absorption of remaining fluids and salts from the gut content. Its distinct anatomical structures are the cecum, appendix, colon, rectum and anal canal (see Figure 2).

The appendix and cecum represent the beginning structures of the large intestine in the right groin, whereby the cecum measures 6cm - 9cm. Thereafter, the large intestine continues upward by the ascending colon through the right flank and into the right hypochondrium, measuring about 15cm – 20cm. The right colic flexure represents the location below the liver where the intestine bends to the left. Crossing the abdomen as the transverse colon, it proceeds into the left hypochondrium, where it bends downwards at the left colic flexure. From there it continues as the descending colon through the left flank into the left groin, measuring about 10cm – 15cm. There it proceeds into the pelvic cavity in form of the sigmoid colon which expands about 12cm – 15cm. The rectosigmoid junction is generally described to be located around the level of the vertebra SIII and is marked by the fusion of the tenia of the sigmoid colon to form the circumferential longitudinal muscle of the rectum. The rectum measures roughly about 12cm in length and ends with the anal canal.

All parts of the large intestine are covered by the peritoneum, a serous membrane, which secretes lubrication fluids. The peritoneum can be further distinguished depending on the part of the large intestine. Parts of the small intestine, in particular the first part of the duodenum, jejunum and ileum as well as the first parts of the large intestine, cecum, appendix, transverse colon, sigmoid colon and upper third of the rectum are covered by the intraperitoneal. The rest of the duodenum, ascending colon, descending colon and middle third of the rectum are covered by retroperitoneal. The last third of the rectum is covered in infraperitoneal (Tortora and Derrickson, 2008). Depending on the MR pulse sequence, the tissues' osmotic water content and possible giving of contrast media, their depiction in MR can vary (Paley and Ros, 1997) (Elsayes et al., 2006). All parts of the large intestine are covered by layers of outer longitudinal and inner circular smooth muscles.

One of the main characteristics of the large intestine is its large diameter compared to the small intestine. Accumulations of fat in form of the omental appendices are in particular associated with the colon. Primarily visible in the cecum and colon are the taeniae coli which are segregations of longitudinal muscles in its wall into three bands. Moreover, the large intestine is characterized by sacculations of the colon in form of the haustra of colon.

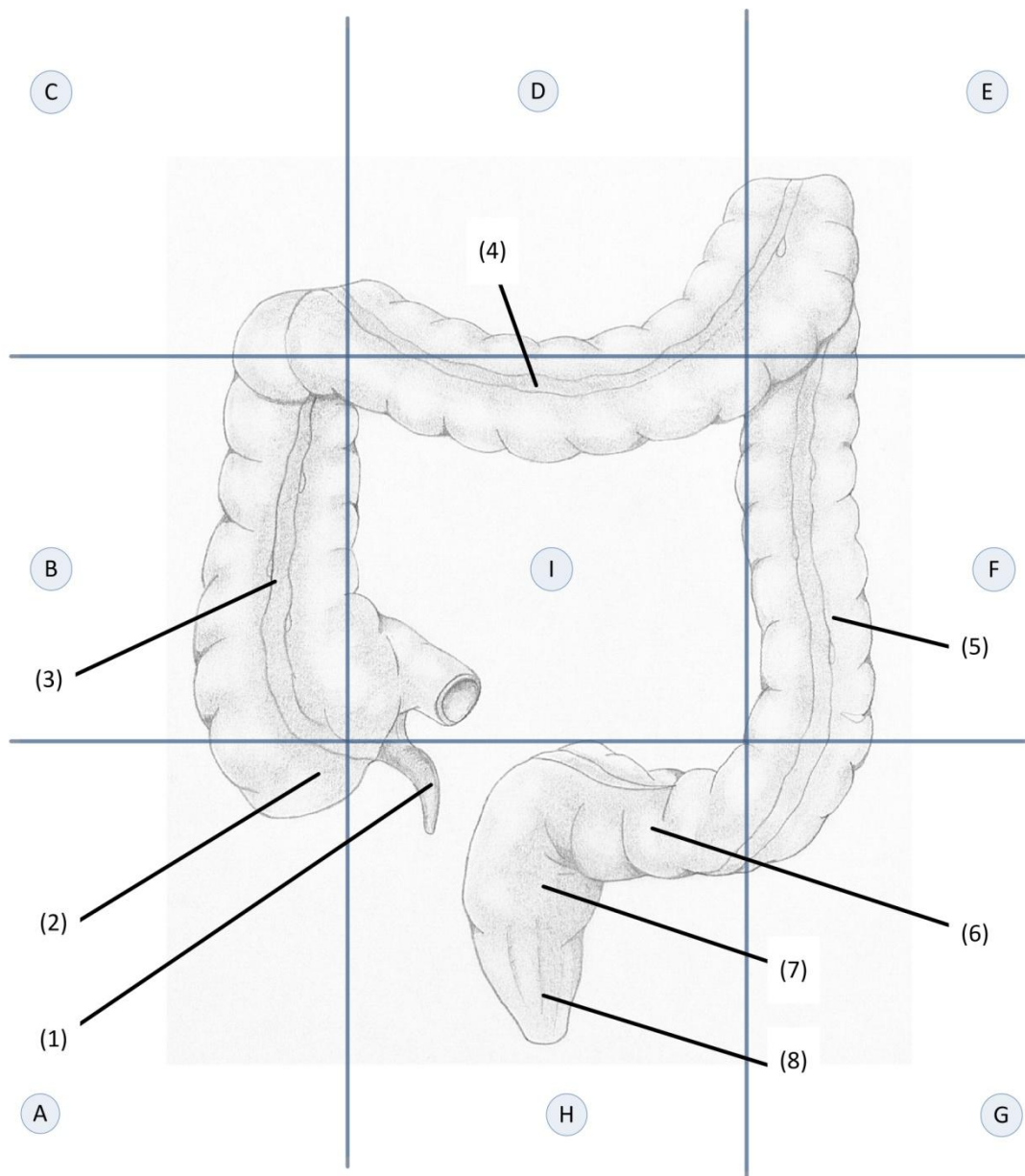


Figure 2: Illustration of the large intestine. It starts with the appendix (1) and cecum (2) in the right groin(A), continues as ascending colon (3) into the right flank (B) and right hypochondrium (C), crosses the abdomen (D) as transverse colon (4) into the left hypochondrium (E) and continues into the left flank (F) and left groin (G) as descending colon (5). From there it continues as sigmoid colon (6) and expands as rectum (7) into the anal canal (8) in the pubic (H). The umbilical (I) is not transversed by the large intestine. Illustration based on (Drake et al., 2005)

2.1.2 Image Guided Interstitial Brachytherapy

Treatment of tumor related illness through the application of radiation is one of the most effective therapies besides resection of the affected area and chemotherapy, and is only deployed in combination with other forms of therapy. The object of today's radiotherapy is an improved distribution of the radiation dose. Ensuring the medically necessary concentration of radiation on the affected carcinogenic cells while harmful side effects on healthy tissues are

avoided by sparing them from radiation is pivotal for an accurate tumor treatment (Lechsel, 2007).

For gynecologic cancers the standard-of-care treatment begins with external-beam radiation and is succeeded by brachytherapy. The term brachytherapy origins from the Greek word brachys (“βραχυς”), meaning “short-distance” and describes a radiology treatment procedure where a radiation source is brought in short distance to the tumor as the target volume. Close proximity of the radiation source to the target volume is advantageous to other forms of radiotherapy as it allows accurate local distribution of the radiation dose through sharp dose gradients. Simultaneously to a high integral dose in the target volume, low exposure to radiation of the patient’s healthy tissue can be accomplished (Kauffmann et al., 2006). Usually, only considerably small and easily accessible volumes are treated with brachytherapy (Morris, 1998).

Moreover, brachytherapy can, compared to EBRT, take organ movements as well as alterations in patient setups into account. It also has the potential to reduce radiotherapy related morbidity and enhance quality-of-life if imaging technologies are repetitively used to support the procedure (Viswanathan, 2011).

In clinical usage three types of brachytherapy can be discriminated. *Mold treatment* describes a treatment of carcinogen skin malignancies where the radioactive source is externally placed on the patient’s skin area. In *Intracavitary treatment* the radioactive source is placed into the human body through a natural body orifice, e.g. the uterine or anal canal. *Interstitial treatment* is characterized by direct insertion of a sealed radioactive source into the target volume to be treated, e.g. tongue, brain or gynecological structures (Morris, 1998).

The following description of MR-guided interstitial brachytherapy strongly refers to the workflow at Brigham & Women’s Hospital described in (Kapur et al., 2012).

Prior to radiation application, various MR image data is acquired according to a diagnostic MR protocol. This includes a T2-weighted fast spin echo (Siemens TSE), T1-weighted fast spin echo (Siemens TSE) before and after injection of contrast medium, single-shot half-Fourier fast spin echo (Siemens VIBE), diffusion-weighted echo planar imaging, as well as RF-spoiled gradient echo (GRE) sequences. After these preliminary image acquisitions follows external-beam radiation succeeded by interstitial brachytherapy in BWH’s state-of-the-art Advanced Multimodality Image Guided Operating (AMIGO) suite.

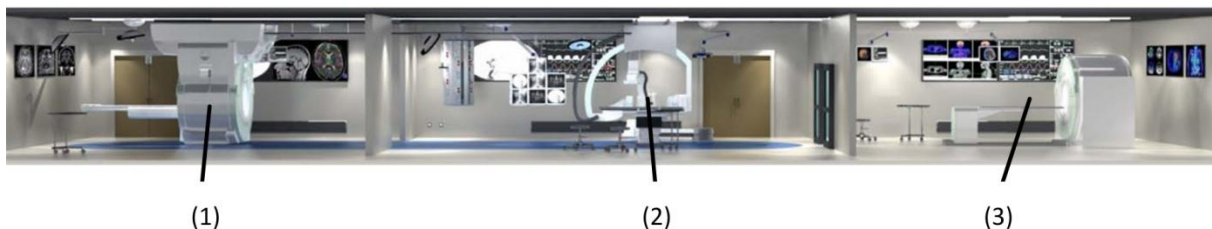


Figure 3: Overview of the AMIGO suite: (1) MRI room, (2) Operating room, (3) PET-CT room (NCIGT, 2013)

To this date, three categories of gynecological procedures have been performed in the AMIGO suite depending on the type of applicator. The first type consists of a MR-compatible tandem coupled with ovoids (T&O) or a ring (T&R). The second type is a hybrid T&O

applicator with needle-bearing ovoids (Utrecht Applicator) or T&R with needle-bearing ring (interstitial ring or Vienna Applicator). The third type of applicator consists of a Syed-Neblett template and plastic needles with central tungsten alloy obturators. The procedure involving the last type of applicator will be described in further detail (see Figure 5).

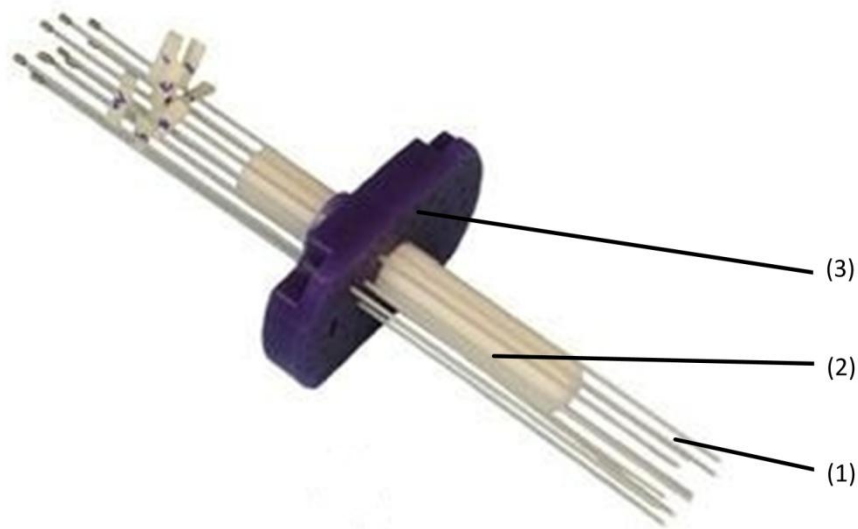


Figure 4: Applicator used in gynecological brachytherapy: (1) needles, (2) obturator, (3) template (© BWH-SPL, 2012)

The first step in interstitial brachytherapy is the insertion of a sterile speculum into the vaginal canal to provide sufficient visualization of the vagina and the tumor to be treated. Thereafter a single suture is threaded into the apex which assists in retracting the vaginal apex as inferiorly as possible. The obturator is then inserted against the vaginal apex and over the suture. The template is put over the already inserted plastic obturator. At all four corners the template is sutured to the patient's skin. Before the placement of the template, its holes are filled with sterile contrast agent for enhanced visibility of the subsequently inserted needles. With the obturator and template inserted and sutured, an initial three-plane (sagittal, axial and coronal) T2-weighted MR localizer is conducted.

Although CT and MRI are both used for image-guided radiotherapy of gynecological malignancies, CT is widely seen as modality of choice for treatment planning of external-beam radiation and assists in diagnosis. MRI stands for the standard modality for image guided brachytherapy and is regarded as the gold standard for the assessment of gynecological malignancies. In contrast to the less precise information about tumor extension, tumor regression and internal organ movements CT delivers, MRI accomplishes accurate depiction. For IGBT in particular T2-weighted MRI sequences are considered as the gold standard. The use of MRI-compatible applicator and probes as well as contrast agent impregnated vaginal packing facilitates clear depiction of all relevant anatomical structures in the acquired images. Although only limited data about the correlation between image orientation and quality of object outlining is available, the orientation of image acquisition is suggested to be conducted in a "brachytherapy oriented view" displaying the applicator from an orthogonal and parallel orientation (Viswanathan, 2011).

After image acquisition, tungsten alloy central obturator needles are inserted into 24cm - 29 cm long hollow plastic catheters (ProGuide, Nucletron Co.) and both are inserted together into

the patient through the template's holes. After the first needles are inserted, a 3D-balanced steady-state free precession (bSSFP) sagittal image is acquired to localize the catheters and enable adjustments. This prevents unintended insertion of the needles into adjacent organs and improves full tumor circumvallation. Thereafter, subsequent needles are inserted in a way that the visualized area of the tumor is fully covered and healthy tissue is spared. In the progress of needle insertion, a series of T2-weighted MR scans are acquired for quick-monitoring purposes. After all needles are inserted, final T2-weighted MR images with a slice thickness of 1.6 mm are acquired in the sagittal, axial and coronal planes (see Figure 5).

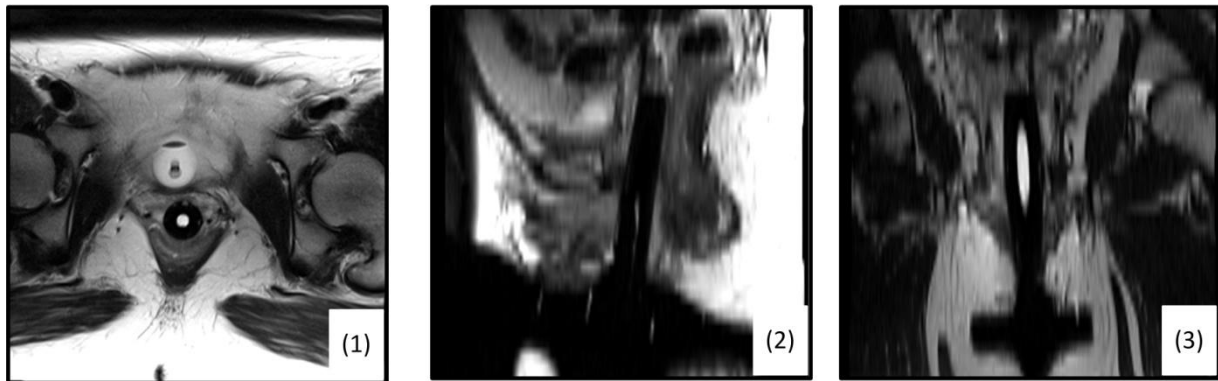


Figure 5: T2-weighted MR images recorded in the course of gynecological brachytherapy: (1) axial view, (2) sagittal view, (3) coronal view (© TUM-MIMED, 2012, MRI data from (Egger et al., 2012e))

Afterwards, those images are transferred to the treatment-planning system (Ocentra Brachy, Nucletron Co.) via the internal BWH network. The first step in treatment-planning consists of manual contouring the tumor as well as adjacent organs-at-risk represented by the bladder and rectum/sigmoid colon. To support segmentation of the bladder a Foley catheter filled with contrast media is applied through the urethra prior image acquisition which leads to contrast rich depiction. In the last step of treatment-planning, dosimetric calculations are conducted to determine the medically necessary amount of radiation. The results are used as basis for the patient individual treatment plan.

Thereafter, radiological brachytherapy is administered based on the treatment plan.

2.1.3 Treatment Planning

For every radiology treatment a patient individual therapy plan has to be compiled. A general workflow description applying both to EBRT and IGBT is given in Figure 6. In the process of treatment planning the segmentation of the tumor and adjacent organs-at-risk is performed and the amount of applied radiation is estimated.

After image acquisition, the first step of treatment planning consists of the determination of the target volume to be treated. According to the International Commission on Radiation Units and Measurements (ICRU) ((Measurements, 1999)) various target volumes are defined. Those volumes can be distinguished into oncological volumes and radiotherapeutic volumes.

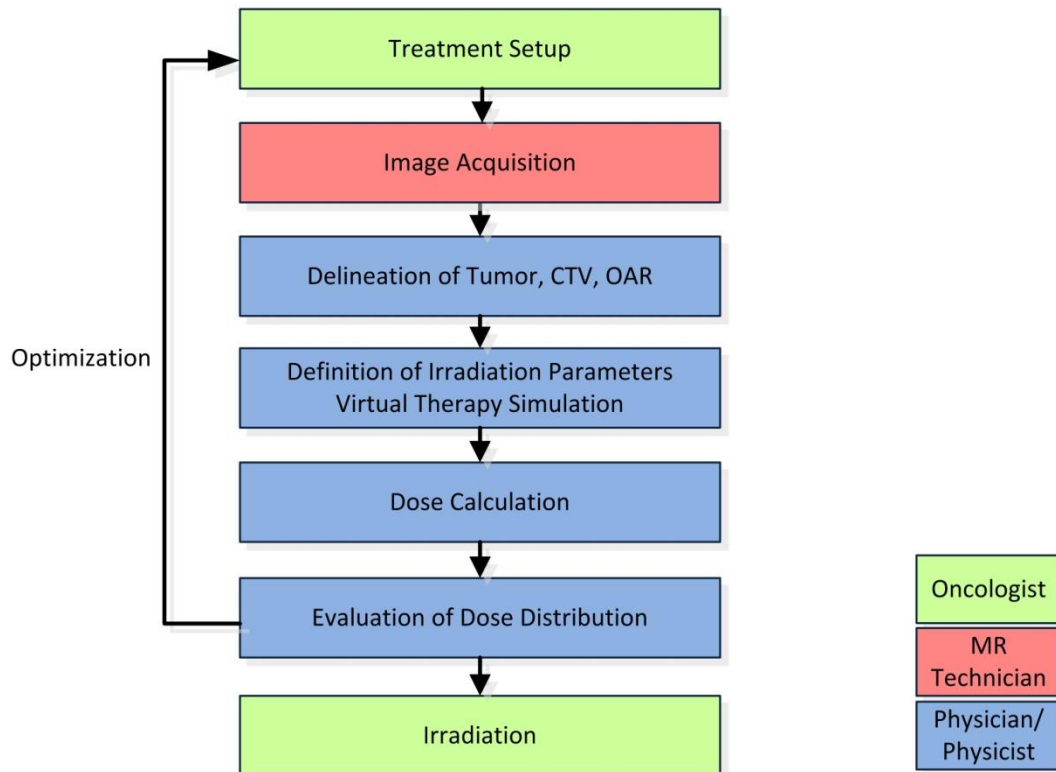


Figure 6: General workflow of a radiology treatment plan; Clinical Target Volume (CTV), Organ-At-Risk (OAR); altered from (Bille and Schlegel, 2002)

Oncological volumes consist of the gross tumor volume (GTV) and the potential tumor spread area.

The GTV can be described by visibility in different image slices and encompasses an area where tumor cells were diagnostically or surgically verified. Further indirect indications for GTV determination are deformations of adjacent healthy structures. The potential tumor spread area encompasses an area surrounding the GTV where no tumor cells have been verified, proliferation into this area has to be assumed however. The clinical target volume (CTV) has to fully encompass the GTV as well as the potential tumor spread area.

Radiotherapeutic volumes are represented by several volumes taking alterations of the patient position, dose distribution and exposition of radiation into account.

The clinical target volume (CTV) has to fully encompass the GTV as well as the potential tumor spread area. The planning target volume (PTV) comprises the CTV and an additional safety area to take alteration in the progress of therapy into account, e.g. non reproducibility of patient positions, different filling levels of organs and organ movement or weight loss.

In case the PTV is covered by an isodose area which is sufficient for the treatment target, the treated volume (TV) equals the PTV. The TV has to equal or be larger than the PTV.

The irritated volume (IV) describes areas where exposition to radiation is undesirable, however, inevitable and effects of radiation cannot be precluded.

In case healthy tissues prone to side effects of radiation are found in the area where radiation is applied, those tissues or organs have to be denoted and segmented as organs-at-risk.

According to their respective sensitivity to radiation these OAR have to be spared from radiation exposition or at least be taken into account for dose distribution (Kauffmann et al., 2006), (Bille and Schlegel, 2002).

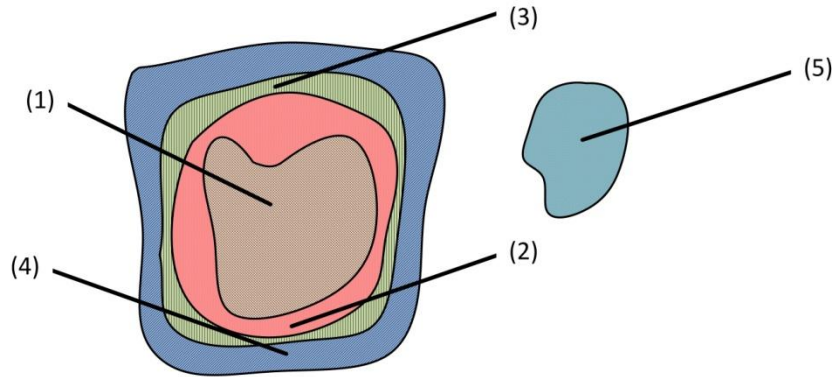


Figure 7: Schematic depiction of oncological and radiotherapeutic volumes in treatment planning: (1) Gross Tumor Volume (GTV), (2) Clinical Target Volume (CTV), (3) Irrigated Volume (IV), (4) Planning Target Volume (PTV), (5) Organ-At-Risk, illustration based on (Kauffmann et al., 2006)

Regarding radiation sensitivity, the stomach has the highest risk of long-term effects due to exposition to radiation of all organs of the digestive system. After exposition of 40 Gy serious symptoms appear in form of stomach pain, nausea, loss of appetite and vomiting. Exceeding 40 Gy chronic side effects are prone to appear in form of ulcers and bleeding. The upper limit for the stomach is considered to be approximately 50 Gy. Sensitivity to radiation decreases continuously from the stomach to the rectum. The risk of chronic after-effects to exposition of 50 Gy decreases from 50% at the stomach, to 35% at the small intestine, to 20% at the colon and 5% at the rectum. However, these values strongly correlate with dose fraction (Kauffmann et al., 2006)

The specific workflow of treatment planning of IGBT at BWH will be described in further detail and refers to details given in (Kapur et al., 2012). At BWH treatment planning for IGBT comprises radiation distribution confined by the template and dose calculation. It can also comprise the step of applicator selection and inserted needle arrangement. As described in chapter 2.1.2 all patients undergo axial, sagittal and coronal T2-weighted MR imaging with a slice thickness of 1.6mm after applicator insertion. To ensure the applicator can be localized additional CT scans are performed and a rigid registration with the MR images is computed

Thereafter follows manual contouring of the normal tissue in the CT/MR merged images. Contouring of CTV as well as OAR is performed in MR images since MR provides clearer depiction of the soft tissue regions of interest.

With high dose gradients in state-of-the art brachytherapy, the applicator needs to be reconstructed to ensure exact dose delivery and distribution. This step can either be performed manually or model-based.

The actual 3D planning is iterative and starts with a standard 2D plan. For T&O as wells as T&R treatments the preliminary designed plan is normalized to point A. Thereby Point A describes a point in 2cm distance from the tandem and 2cm superior to the upper surface of the vaginal applicator and is often used as a reference in IGBT (Mundt et al., 2011). For

interstitial treatment all needles are loaded symmetrically in the preliminary standard planning, however point A is not defined.

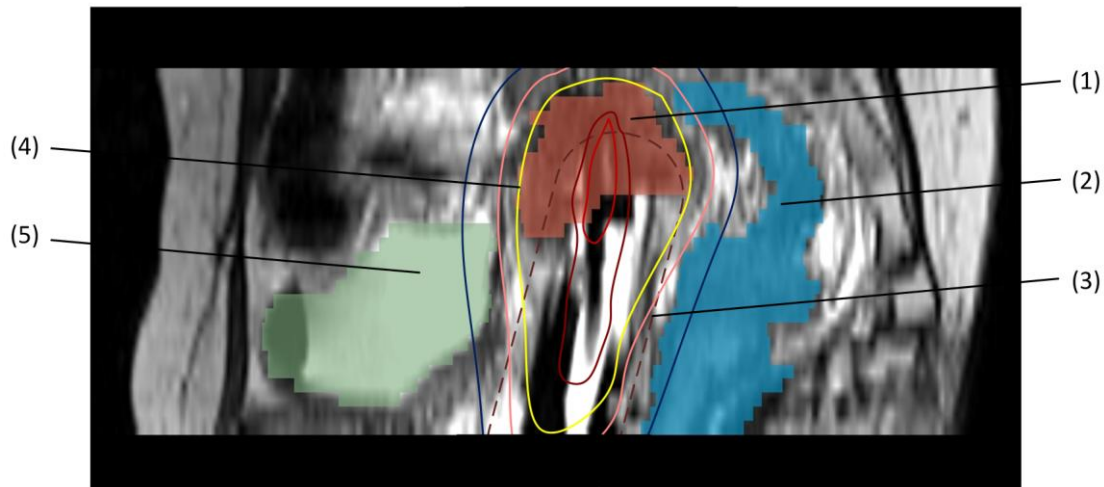


Figure 8: Interstitial treatment planning: slice-by-slice optimization of radiation dose distribution on tumor (CTV) and sparing adjacent Organs-At-Risk, (1) Tumor, (2) Rectum/sigmoid colon, (3) Brachytherapy obturator, (4) 100% isodose line, (5) urinary bladder (illustrated from Kapur et al. (2012), data from Egger et al. (2012e))

After preliminary planning based on a standard 2D distribution follows optimization in 3D. Figure 8 illustrates how based on the segmentations performed in CT and MR the standard plan is altered to satisfy case specific constraints and parameters for each specific case. This is done by manually altering dwell times in various locations to achieve optimal coverage of the CTV while dose exposition to OAR is simultaneously minimized. Radiation coverage is evaluated by the CTV D90 parameter which represents a standard parameter for treatment planning evaluation (Jürgenliemk-Schulz et al., 2010). Ideally, the CTV D90 should exceed 100% of the prescribed dose to the CTV. This estimation is conducted manually by slice by slice comparison of dose distribution and CTV. The final 3D adjustment of dose distribution further increases CTV radiation coverage and decreases the dose applied to OAR.

2.1.4 MRI Depiction of the Lesser Female Pelvis & Rectum/Sigmoid Colon

As described in chapter 2.1.2, CT and MRI are both in usage for image-guided radiotherapy of gynecological malignancies. However, CT is widely seen as gold standard for diagnosis and treatment planning of external-beam radiation performances. In contrast to the less precise information about tumor extension or regression and internal organ movements that CT delivers, MRI images present a more accurate depiction and discrimination of tumor and soft tissue. Direct comparisons between object contouring in CT and MR for IGBT treatment planning showed a significant overestimation of contour width in CT images compared to MR (Viswanathan, 2011).

State-of-the-art MR scanners in clinical usage operate in a range of 1.5T – 3T and exhibit an advantageous signal-to-noise ratio. Open low field 0.2T – 0.5T MRI scanners can offer advantages for claustrophobic patients and easier patient handling, however, disadvantages regarding image quality compared to MRI scanners of 1.5T or higher let to increased usage of

scanners of 1.5T and higher in the radiology community. For IGBT T2-weighted MR imaging is considered the gold standard. Its staging accuracy of cervical carcinoma has been evaluated to be between 75% up to 96% (Kapur et al., 2012).

In order to deliver an optimal depiction of all surgical instruments (needles, obturator and template) as well as the tumor and organs-at-risk, image acquisition in a “brachytherapy oriented view” is performed. For optimal outlining of the tumor and OAR, images in axial view are used and are therefore recorded in the highest resolution. (Viswanathan, 2011)

For illustration purposes of the latter following MRI images, Figure 9 shows the same axial anatomical cross section of the lower female pelvis as depicted in axial MR images used for IGBT.

In the center of Figure 9 an anatomical cross-section of the urinary, gastrointestinal and reproductive system can be seen. Anteriorly lies the urinary bladder, followed by the vagina in the center and the rectum posteriorly, all covered in serous peritoneum membrane (see section 2.1.1) and layers of outer longitudinal and inner circular smooth muscles.

Lateral from the center, the anatomical structure of the tuber ischiadicum as part of the pelvis bone can be seen. Further lateral a cross section of the os femoris as the thigh bone is to be found. In relation to these bones are the muscles of the various inner pelvic muscles. Further posterior lays the muscle gluteus maximus which represents a large part of the buttocks. The fossa ischianalis represents a body fat compartment lateral to the anal canal and inferior to the pelvic floor.

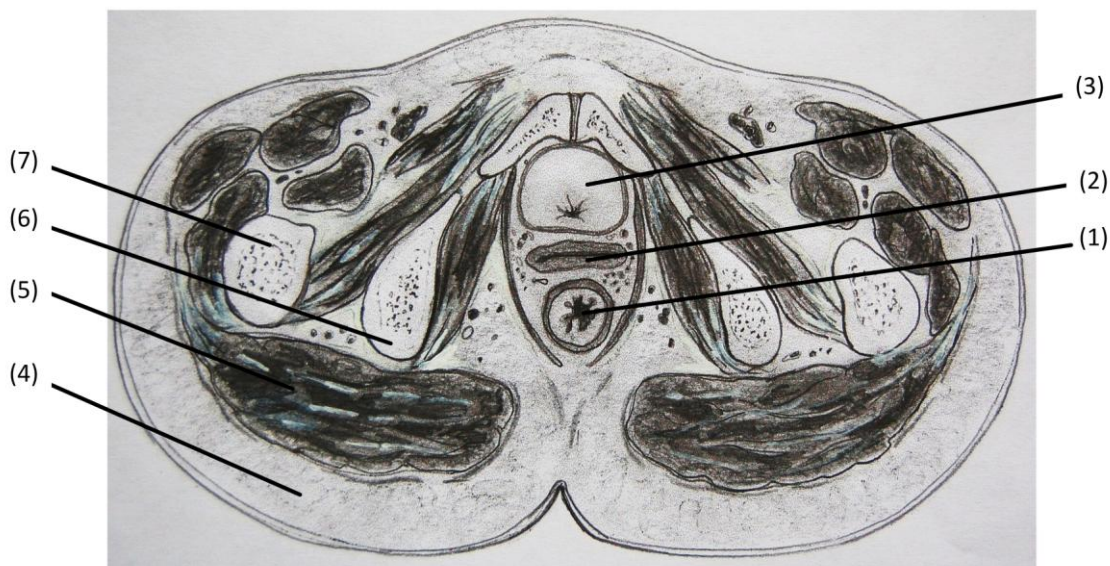


Figure 9: Axial cross section of the anatomical structure of the lower female pelvis: (1) Rectum, (2) Vagina, (3) Urinary Bladder, (4) Fossa Ischionanalis, (5) Gluteus Maximus, (6) Tuber Ischiadicum, (7) Os Femoris. Illustration based on (Schünke et al., 2005)

Figure 10 shows a T2-weighted Turbo Spin Echo (TSE) image in a resolution matrix of 320 x 256.

Besides the illustrated anatomical structures of muscles, bones and body fat compartments, Figure 10 shows, accordingly to Figure 9, several anatomical structures of greater importance

to this thesis. Anteriorly the urinary bladder can be seen, characterized by a high grey value (GV) relative to the whole image. This is due to given contrast media prior to image acquisition to facilitate depiction and delineation. In the center of the bladder the inserted catheter is visible. In the given slice only a limited cross section of the bladder is visible and will expand to an approximate shape marked by the dashed line in further slices.

Below the bladder the vaginal canal and the inserted brachytherapy obturator can be distinguished. The gynecological tumor encompasses parts of the obturator and is located in close proximity to the urinary bladder and rectum, which leads to potential radiation and thus classifies them as organs-at-risk. In close proximity to the tumor and obturator several brachytherapy needles are found, depicted as dark, round dots.

Posteriorly of the vagina and obturator lays the anatomical structure of the rectum and sigmoid colon. In T2-weighted TSE MR images the rectum/sigmoid colon is mostly characterized by a medium level grey value relative to the whole image. In several cases it can also be characterized by a dark border which roughly distinguishes it from adjacent structures.

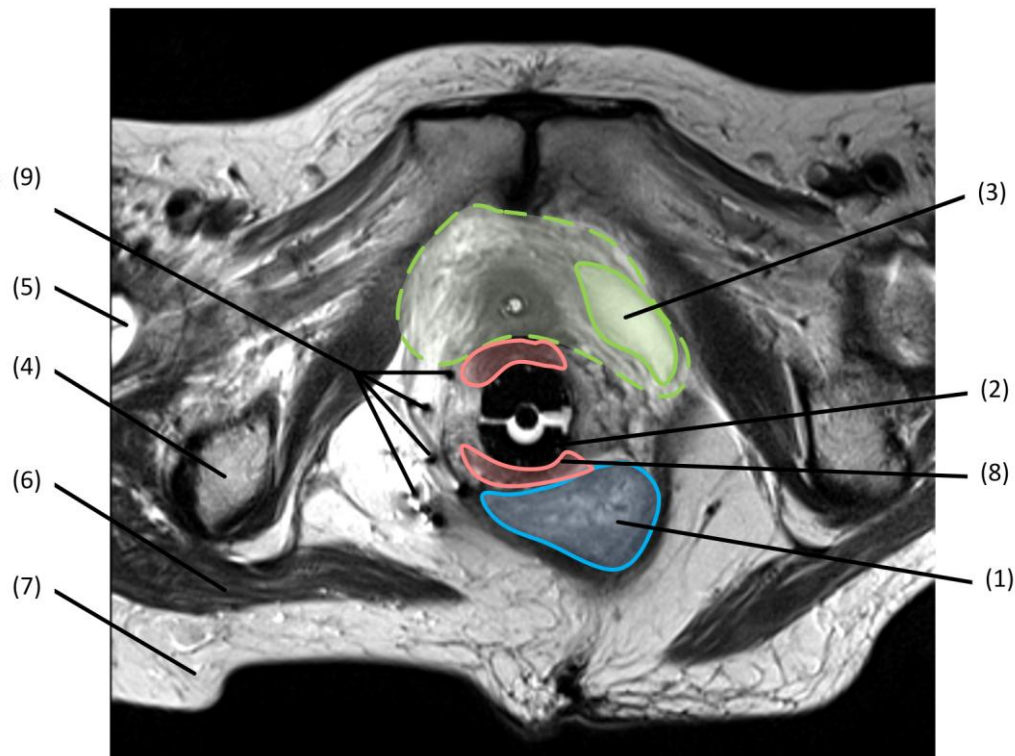


Figure 10: Axial cross section of the lower female pelvis in a T2-weighted TSE image with anatomical structures: (1) Rectum, (2) Vagina & Obturator, (3) Urinary Bladder, (4) Tuber Ischiadicum, (5) Os Femoris, (6) Gluteus Maximus, (7) Fossa Ischionalis, (8) Gynecological Tumor, (9) Brachytherapy Needles (© TUM-MIMED, 2012, MRI data from (Egger et al., 2012e))

In the publicly available MR data sets which have been used for this thesis (Egger et al., 2012e), the depiction of the rectum/sigmoid colon strongly varies as can be seen in Figure 11. From each data set to another, its shape, size, slice thickness and grey value distribution alter in no predictable manner.

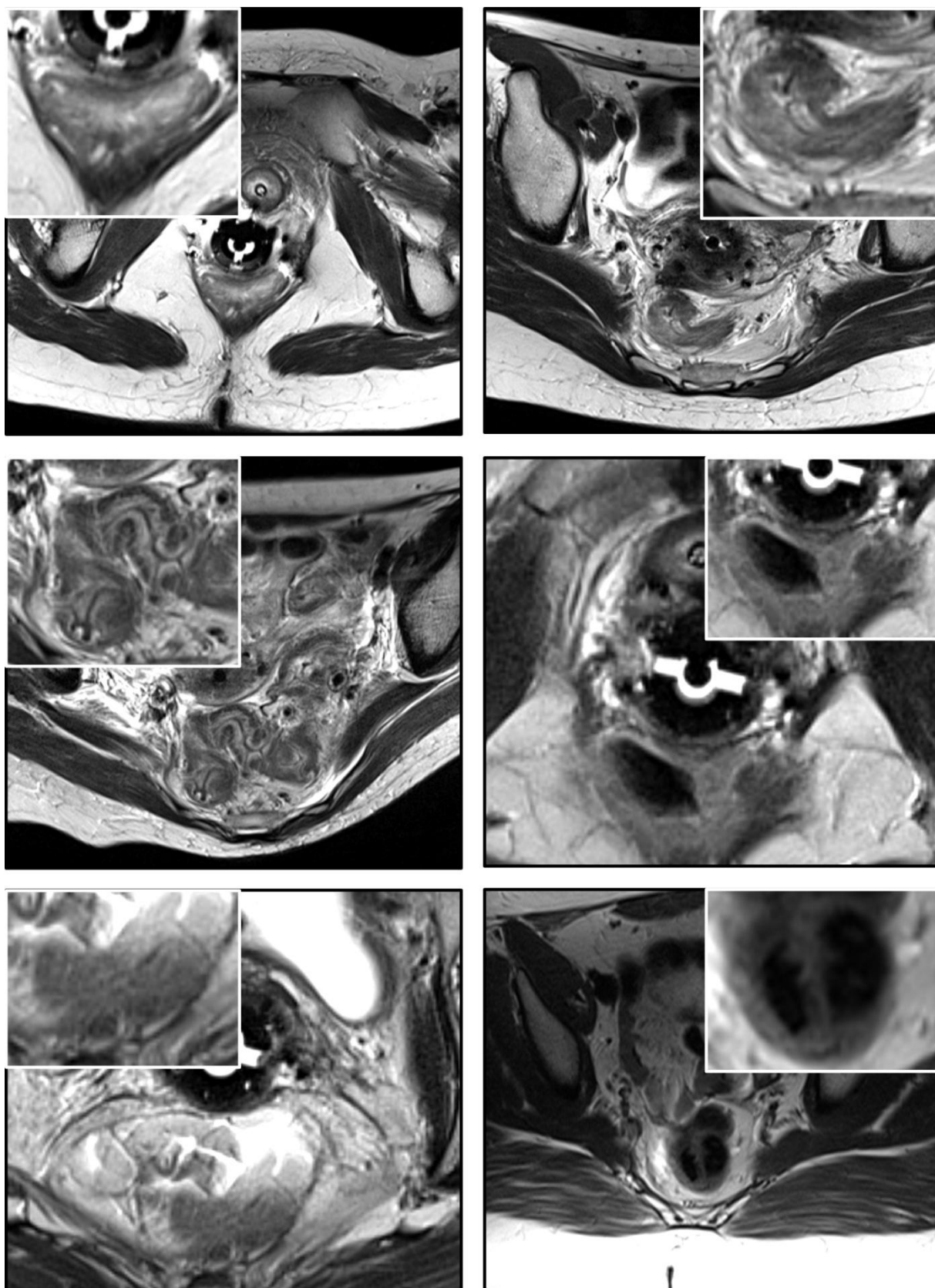


Figure 11: Depiction of the rectum/sigmoid colon in several different data sets of T2-weighted TSE MR images. Its appearance alters in shape, contrast and grey value distribution in no predictable manner (© TUM-MIMED, 2012, MRI data from (Egger et al., 2012e))

Outlining of a tumor and the adjacent organs-at-risk, in particular the bladder and rectum/sigmoid colon, is manually performed in axial view oriented T2-weighted MR images. As mentioned in chapter 2.1, patient-individual pelvic organ shape and partly poor soft tissue discrimination by current imaging technologies prevents computer-based segmentation and makes it a difficult task for physicians (Pasquier et al., 2007). This inevitably leads to inter- as well as intra-personal variances regarding segmented volumes. Since every segmentation performance is a subjective task, the segmentation result, besides imaging quality, strongly depends on clinical experience of the performing physician (Bille and Schlegel, 2002).

2.2 State of Clinical Applications

In the clinical routine manual segmentation is still considered the gold standard for segmentation of anatomical structures in general and also the rectum/sigmoid colon (Chang et al., 2011) (Elsa et al., 2010) (Birkbeck et al., 2009). Its workflow and usage will be shortly described in this chapter. Currently available commercial tools which provide segmentation tools include the Smart SegmentationTM Tool of the Varian, Inc.

2.2.1 Manual Segmentation

Slice by slice manual outlining of anatomical structures with little computer assistance is the standard methodology for clinical segmentation tasks. In some cases it can be necessary to outline as many as 10 anatomical structures in more than 50 image slices, making it a tedious time consuming task (Bille and Schlegel, 2002).

Moreover, manual segmentation is still considered the gold standard and the widely accepted reference method for comparisons between different segmentation methodologies. Although manual segmentation is time consuming and prone to high inter- and intra-observer variability, until today no computer-assisted methodology exhibits sufficient robustness and reproducibility to be taken as a standard reference instead (Chang et al., 2011) (Elsa et al., 2010) (Birkbeck et al., 2009). This lack of an objective computer-based segmentation standard causes manual segmentations continuously used as the only methodology at hand to compare segmentation algorithms, although manual segmentation itself is highly subjective, strongly depends on individual clinical experience of the performing physicians and exhibits difficult reproducibility (Bille and Schlegel, 2002).

Egger et al. compared manual segmentations of glioblastoma multiforme brain tumors in MR images performed by three different physicians to estimate inter- and intra-variability. To estimate intra-variability a physician was asked to perform the same segmentation within a period of two weeks. The result revealed a DSC of $90.29 \pm 4.48\%$ for the same physician's different segmentations. The segmentation of two other physicians was compared to the segmentation of the first and revealed a inter-variability in the DSC values of $88 \pm 6.08\%$ and $86.63 \pm 6.87\%$ (Egger et al., 2013). These results show the difficulty that lies within manual segmentation being used in clinical daily routine and its use as reference method to evaluate segmentation algorithms.

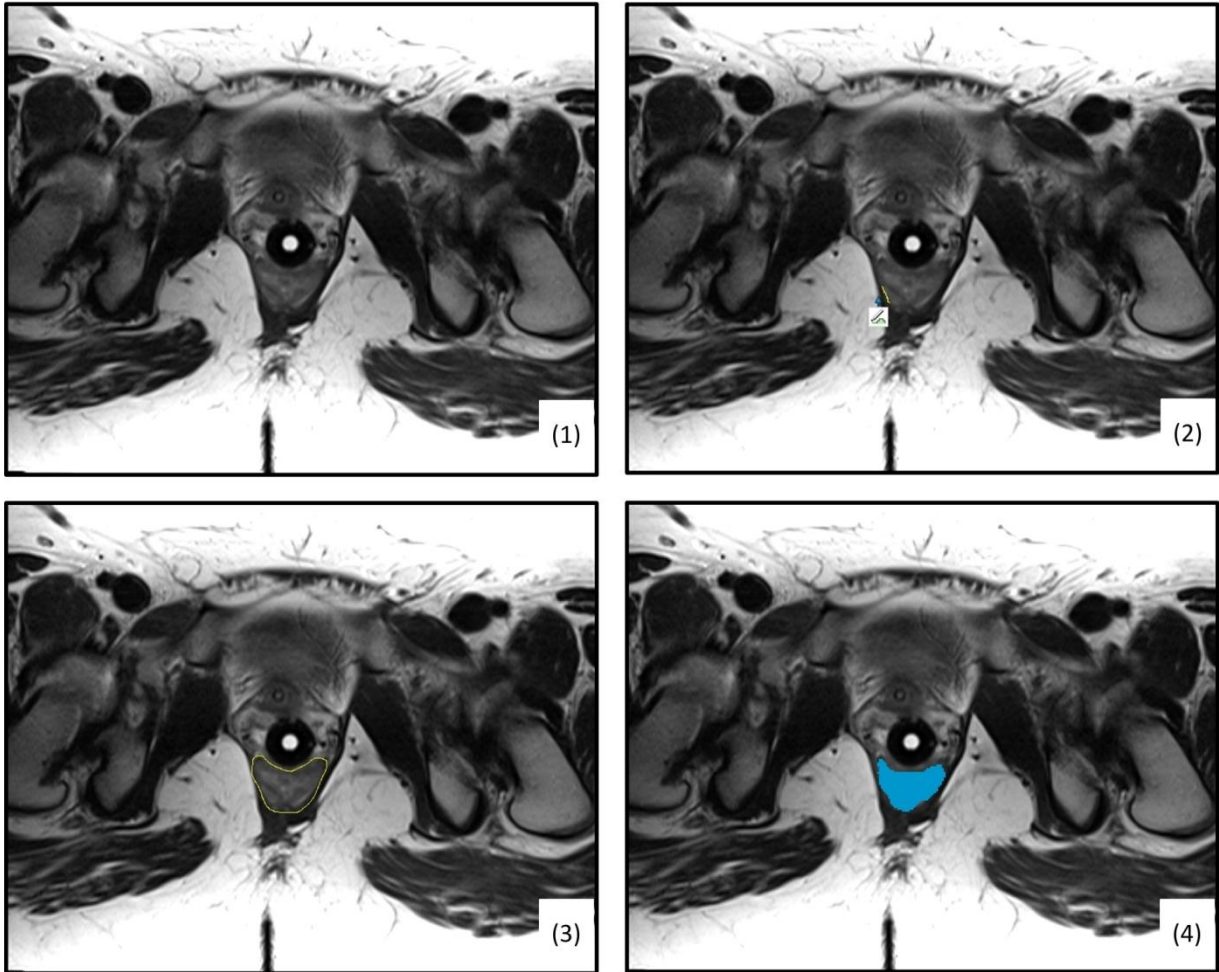


Figure 12: Sequence of a manual segmentation of the rectum/sigmoid colon by using the Draw Effect Tool included in 3D Slicer. The object in (1) is outlined slice by slice by a draw effect tool (2), (3) and the enclosed area is stored (4) (© TUM-MIMED, 2012, MRI data from (Egger et al., 2012e))

As an example, manual segmentation will be shortly illustrated by the Draw Effect Tool of the open source software package 3D Slicer (Slicer-Community, 2013a) which is used for research purposes at the Brigham & Women's Hospital (see Figure 12).

Figure 12 illustrates a sequence of a manual segmentation in a single slice. The user outlines the object contour and the enclosed pixel area is stored. After all slices are segmented and organ contours are stored separately, the 3D volume of all objects is calculated. Figure 13 shows the calculated volume of the relevant organs-at-risk in gynecological brachytherapy, rectum/sigmoid colon (blue) and urinary bladder (green), as well as the tumor (red).

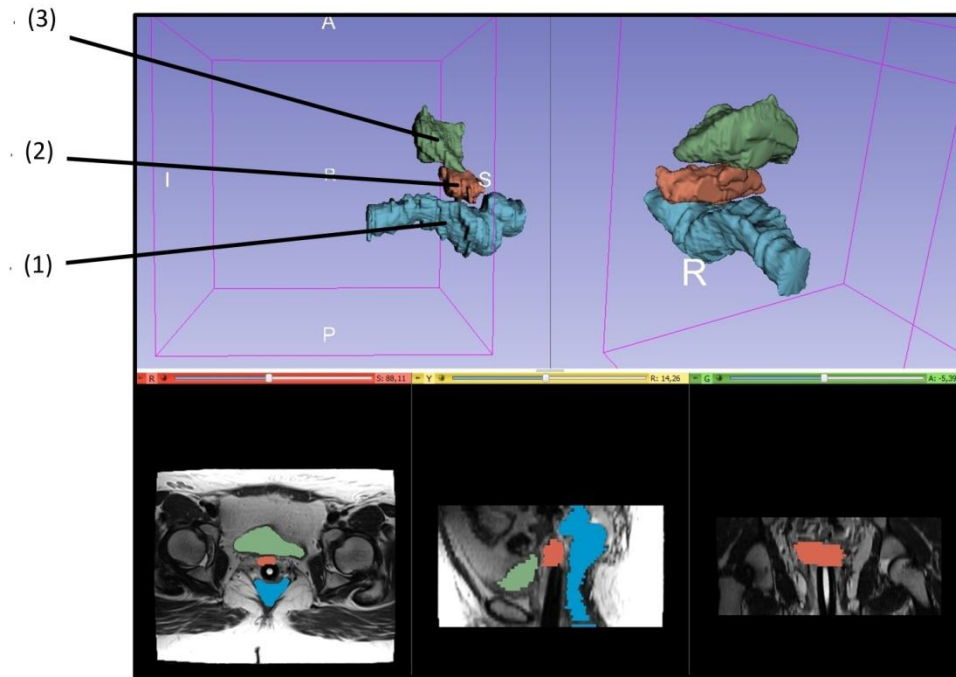


Figure 13: After outlining of all respective organ slices, the volume is calculated and displayed: (1) Rectum/Sigmoid colon in blue, (2) Tumor in red, (3) Urinary Bladder in green (© BWH-SPL, 2012, MRI data from (Egger et al., 2012e))

2.2.2 Commercial Segmentation Tools

Smart SegmentationTM Tool of Varian, Inc.

The Varian Medical Systems, Inc. offers a software package EclipseTM. It is a treatment planning software for radiation therapy planning, including electron-, proton- and brachytherapy (Varian, 2013). It is also used at BWH for treatment planning of interstitial brachytherapy treatment planning described in detail in section 2.1.3. Within the EclipseTM software package the software tool Smart Segmentation[®] for contouring applications can be found. This tool is an automatic segmentation tool for anatomical structures and uses a rule-based algorithm approach with anatomical reference points and organ-specific segmentation methods. It was specifically developed for the evaluation of CT-based images. The course of segmentation is as following. First a pre-segmentation step finds body outlines as well as bones and lung equivalent tissue, separating the body volume from the. Thereafter follows a step for detection of the anatomic orientation which determines the patient position, patient gender and the respective body region. In the last step follows structure segmentation which tries to localize reference points, outlines specific organs and refines the result.

The algorithm has been clinically evaluated by comparison to manual segmentations of several clinicians and radiation oncologist and a data set of 600 CT images. The qualitative and quantitative analysis of the algorithm proofed its efficiency and its usage can lead to a time gain for the segmentation of the prostate and the bladder.

Although robustness and time saving potential could be shown, manual corrections of organ outlines had generally to be performed. The outline of the rectum proofed to be especially

challenging and required further improvements. The result for the segmentation of the bladder was considered between “excellent” and “good”. For the rectum the result was considered “acceptable” to “not acceptable” (Haas et al.) (Haas et al., 2008) (Huyskens et al., 2008).

2.3 State of Research

Various fully automatic as well as interactive semi-automatic segmentation tools have been developed to this date. They are based on distinctive mathematical theories and exhibit characteristic user workflows and parameter handling. Region-based approaches investigate grey values in interrelated regions, whereas contour-based approaches detect object contours and try to track them. Graph-based methods are a fairly new methodology where a graph is set up, grey values sampled determine its edges weights and a minimization along the graph is calculated to find an object contour. An overview about the current state of research on segmentation tools and their mathematical principles is given in this chapter.

2.3.1 Region Growing

In the methodology of region growing the grey values of pixels are examined and according to predefined rules, the respective pixels are successively labeled as part of the object or part of the background. This is repeatedly performed over every pixel until the whole image has been segmented and each pixel has been grouped (Davies, 2012). Generally, in a first step features are extracted neglecting possible object contours. Thereafter follows a preliminary segmentation. With the knowledge of the preliminary segmentation all previously extracted features are calculated anew. This scheme of alternating feature extraction and segmentation is repeated until it converges against a steady result (Jähne, 2005)

Region growing algorithms are often used in combination with seed points which can be set by the user inside the object or outside into the background. Initially, the algorithm starts its iterative labeling around the seed point area with information provided by these.

Two methodologies based on region growing will be further explained in detail.

Simple Region Growing

The simple region growing (Community, 2013) algorithm is based on a statistical region growing scheme which accepts one or several user-defined seed points as input. Starting with the area around the seed points a statistical model of the foreground consisting of the mean and standard deviation of intensity is computed. This statistical model is transferred into a scalar threshold range using the mean intensity of a seed point plus or minus a multiplier of the standard deviation. After this computation the result can be refined by recalculating the mean and standard deviation, where after a new segmentation is calculated.

Besides providing seed points, the user has to handle several parameters to control the algorithm, expanding it to more than five degrees of freedom. A *smoothing iterations* parameter and a *time step* parameter define the smoothing parameters. The segmentation

parameters are comprised of a *number of iterations*, a *multiplier* and a *neighborhood radius* parameter.

The algorithm has been tested on the available brachytherapy MRI data by trying to segment the rectum/sigmoid colon. The computed result can be seen in Figure 14. In a first step two seed points are set inside the object. Thereafter the algorithm computes a segmentation result. It can be seen that the algorithm strongly connects neighboring areas of like intensity of the seed points. This causes darker as well as brighter areas of the rectum to be spared and excluded from the segmented area. On the other hand, areas of like intensity to the seed points are falsely included in the segmented area. This phenomenon is known as leaking regarding region growing based algorithms and appears where the labeling criteria is not specific enough to clearly discriminate object and background areas. Thereby, poor contrast around organs contours can result in leaking of the growing area, letting the segmented area reach far beyond the actual object contour (Egger et al., 2012b) (Vezhnevets and Konouchine, 2005) (Heimann et al., 2004).

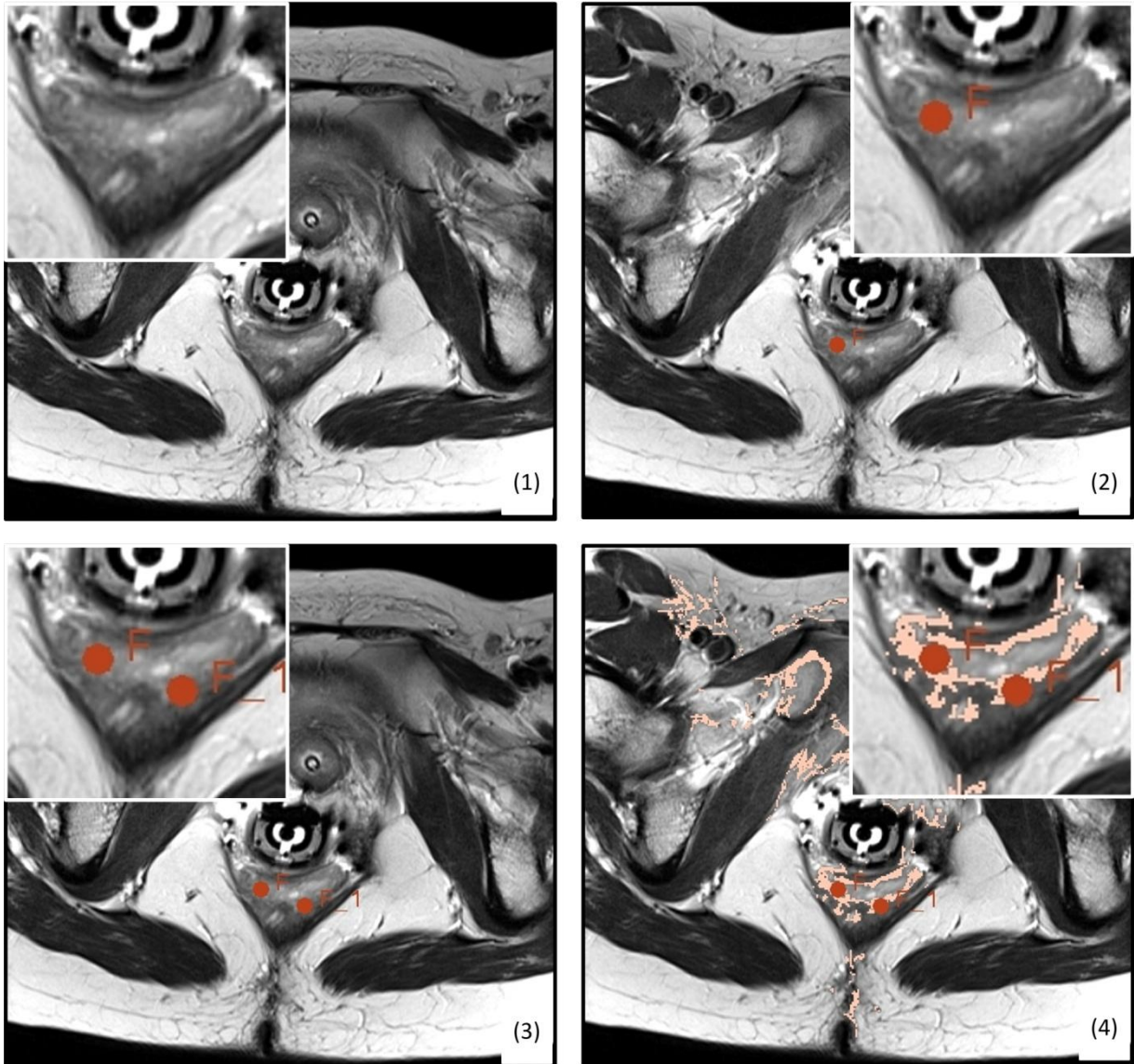


Figure 14: Segmentation result of the rectum/sigmoid colon by the simple region growing algorithm: (1) Raw image, (2) First Seed Point, (3) Second Seed Point, (4) Segmentation Result (© TUM-MIMED, 2012, MRI data from (Egger et al., 2012e))

Although leaking can be limited by cropping a certain area around the region of interest where the algorithm is working, the effect will persist and the quality of the result regarding the region of interest will not be affected or enhanced.

Grow-Cut

The Grow-Cut algorithm is a semi-automatic interactive region growing algorithm. It uses cellular automata and user defined initialization scribbles as input classes and is further described in (Vezhnevets and Konouchine, 2005). The methodology needs a user-defined background class and can additionally cope with n classes to segment, determined by different user scribbles. Based on the user defined scribbles, the algorithm computes a region of interest enclosing the input areas. Thereafter, it tries to label all image pixels according to the different input classes and converges when all pixels are labeled. After a first result is

computed, the user can improve the result by providing further input scribbles where segmentation is tough and run the segmentation again.

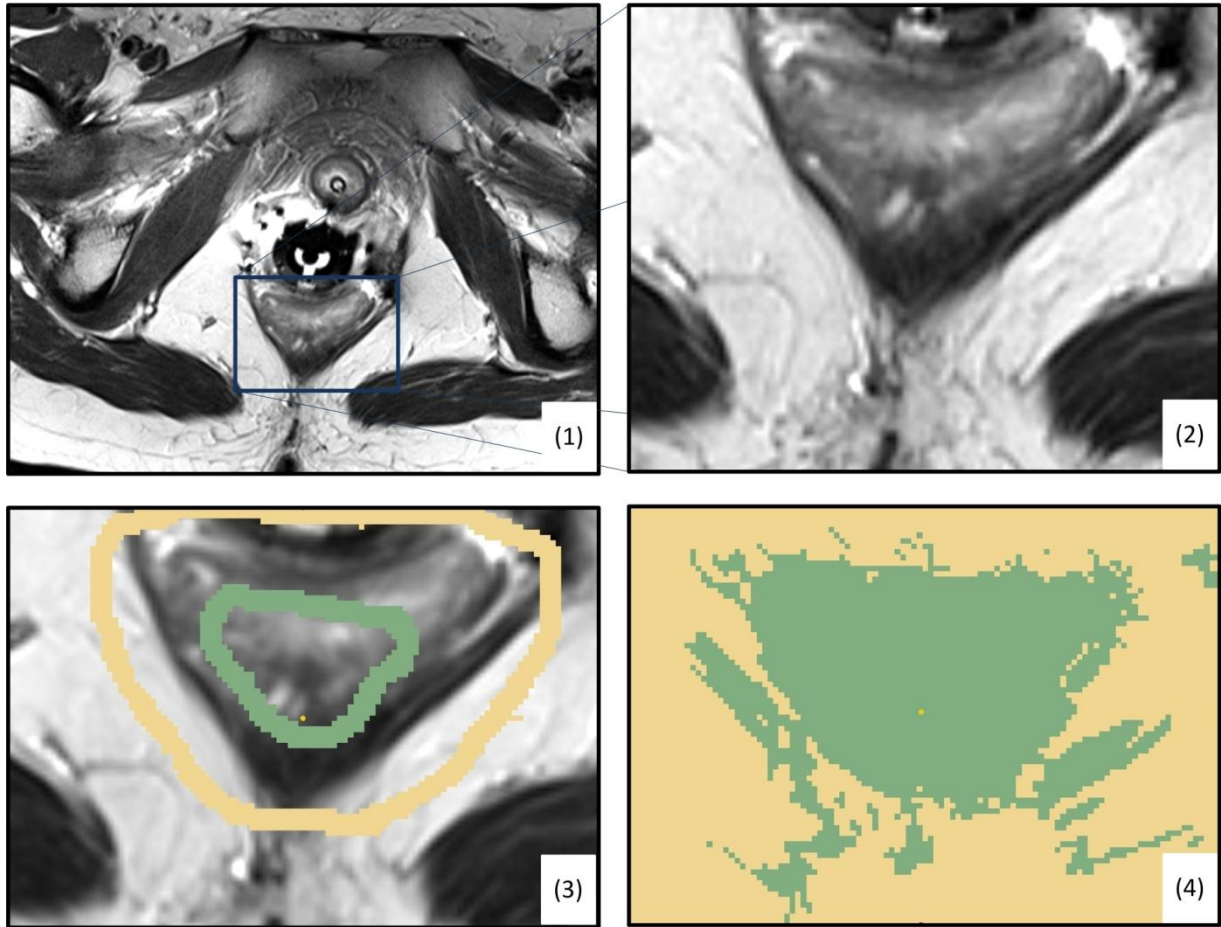


Figure 15: Segmentation result of the rectum/sigmoid colon by the Grow-Cut algorithm: (1) Raw Image, (2) Cropped Region of Interest, (3) Initialization Scribbles: Background (yellow), Object (green), (4) Segmentation Result (© TUM-MIMED, 2012, MRI data from (Egger et al., 2012e))

Egger et al. (Egger et al., 2012a) have investigated Grow-Cut with gynecological MR image data and tried to segment the urinary bladder, rectum/sigmoid colon and a gynecological tumor structure. Successful segmentations of the bladder could be shown by a Dice Similarity Coefficient of 91.94 ± 5.4 compared to clinical expert manual segmentations. However, the Grow-Cut methodology did not achieve sufficient results for the tumor and rectum/sigmoid colon. This is due to their mostly inhomogeneous appearance.

Figure 15 depicts a segmentation of the rectum/sigmoid colon based on the Grow-Cut algorithm. To limit the computation area and time a region of interest (2) is cropped from the original image (1). Thereafter follows an initialization with an object scribble (green) and a background scribble (yellow) (3). In the last screenshot (4) the computed segmentation result is depicted. In similarity to the simple region growing algorithm, Grow-Cut also exhibits leaking tendencies and problems segmenting the rectum/sigmoid colon.

2.3.2 Active Appearance Models

In a segmentation algorithm based on Active Appearance Models (AAM), an atlas is used and prior information is implemented via a tree structure into a statistical model. The tree represents a hierarchical connection between anatomical structures where each sub tree represents a limited segmentation task. Segmentation solutions are calculated through an expectation-maximization by a conventional classifier.

One example of an atlas-based algorithm based on data trees was developed by Pohl et al. (Pohl et al., 2007) and implemented in 3D Slicer as EM Segmenter module. Although it was specifically developed for the segmentation of brain MR images into anatomical structures such as white and grey matter, Pohl et al. mention the adaptability of the algorithm to a wide range of segmentation problems since a new atlas can be created for unknown problems by providing pixel samples.

EM Segmenter

An implementation of an AAM data tree approach can be found in the 3D Slicer under EM Segmenter (Slicer-Community, 2013b) and it was applied to the segmentation of the rectum/sigmoid colon in the given gynecological brachytherapy MR images.

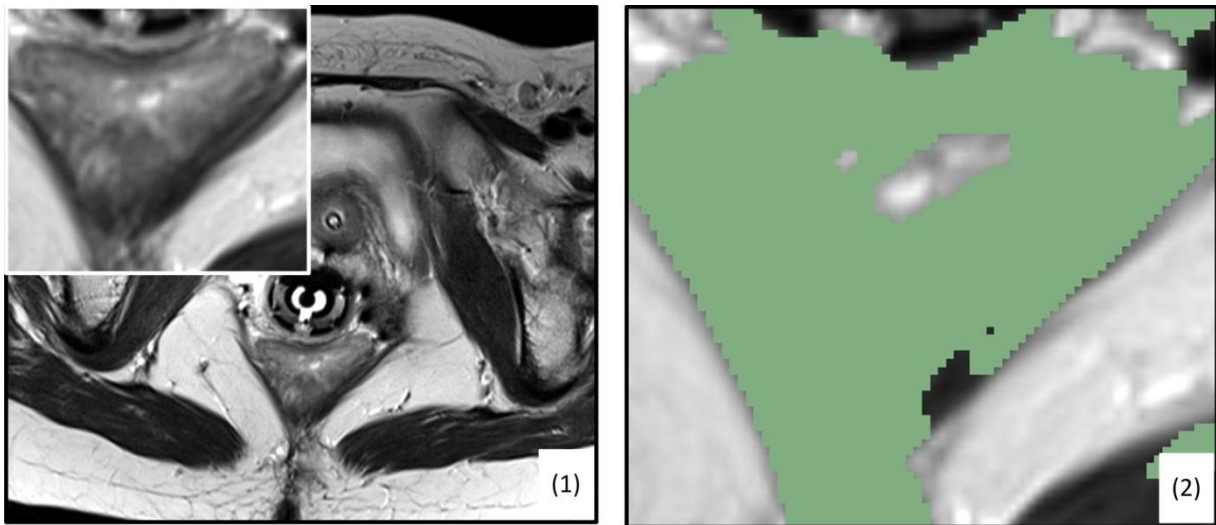


Figure 16: Segmentation of the rectum/sigmoid colon based on a data tree algorithm implemented in the 3D Slicer EM Segmenter tool. (1) Raw image and cropped region of interest, (2) Segmentation result of the region of interest (© TUM-MIMED, 2012, MRI data from (Egger et al., 2012e))

As no hierarchical model of the rectum/sigmoid colon is available, the model was used as EM Segmenter without Atlas which lets the user define a new atlas based on pixel samples. Two types of classes were defined (background and tissue) and 30 pixel samples were provided for each class to generate an atlas. The result can be seen in Figure 16 which shows a leaking tendency of the algorithm and includes areas beyond the object outline.

2.3.3 Active Contours

Active Contours (Kass et al., 1988), also known as deformable contours or snakes, is an object segmentation scheme which tries to outline a complete contour of an object. The idea is to segment an object outline even if the contour might be difficult to define in places due to lack of contrast or noise. Two initialization methodologies are common. Either a large contour encompassing the object is shrunk to fit the object outline or a small contour within in the object is enlarged to match the outline. Basically, the initial contour can be fairly arbitrary. Its shape is iteratively evolved by an energy minimization scheme trying to minimize the external represented by a degree of object fit as well as internal energy which tries to prevent the contour from becoming too complex (Davies, 2012).

Conditioned by the continuous enhancement of the contour, noise and other contour imperfections can be compensated. Furthermore, so called subjective contours can be found by active contours. Subjective contours do physically not exist in images. However they can be reconstructed by including information of adjacent objects and the broader image. One example of a subjective contour is given in Figure 17 which can be found by an active contour approach but is hard to define with conventional approaches such as region growing (Egger, 2012).

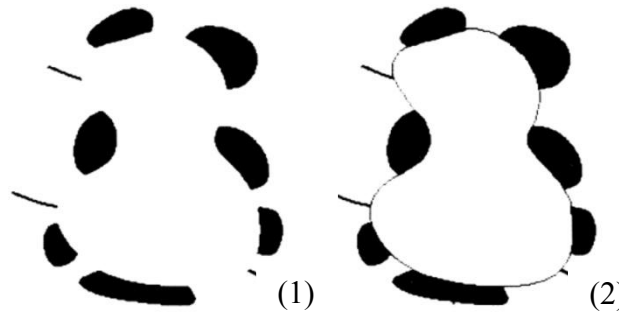


Figure 17: Example of a subjective contour (1) which can be found by an active contour approach (2). Altered from ()

Robust Statistics Segmenter

One example of a segmentation methodology based on active contours is the work of Gao et al. (Gao et al., 2012). An implementation of the algorithm is included in 3D Slicer as Robust Statistics Segmenter (RSS) (Slicer-Community, 2013c). The user can initialize the algorithm by providing several input contours or scribbles. Thereafter, several parameters have to be set. Those parameters encompass the approximate volume, intensity homogeneity $\in [0,1.0]$,

boundary smoothness $\in [0,1.0] \in [0,1.0]$.

The RSS was tested to segment the rectum/sigmoid colon in the available gynecological MR image data which is depicted in Figure 18. To initialize the algorithm two seed contours have been provided as object (green) and background (yellow). The segmentation result is depicted as blue area. It is considerably better compared to the results based on region growing or data trees, because the segmented area stays within the provided background contour (yellow) and

leaking is thereby prevented. Setting the parameters to reasonable values however is considerably difficult and demands a notable amount of time.

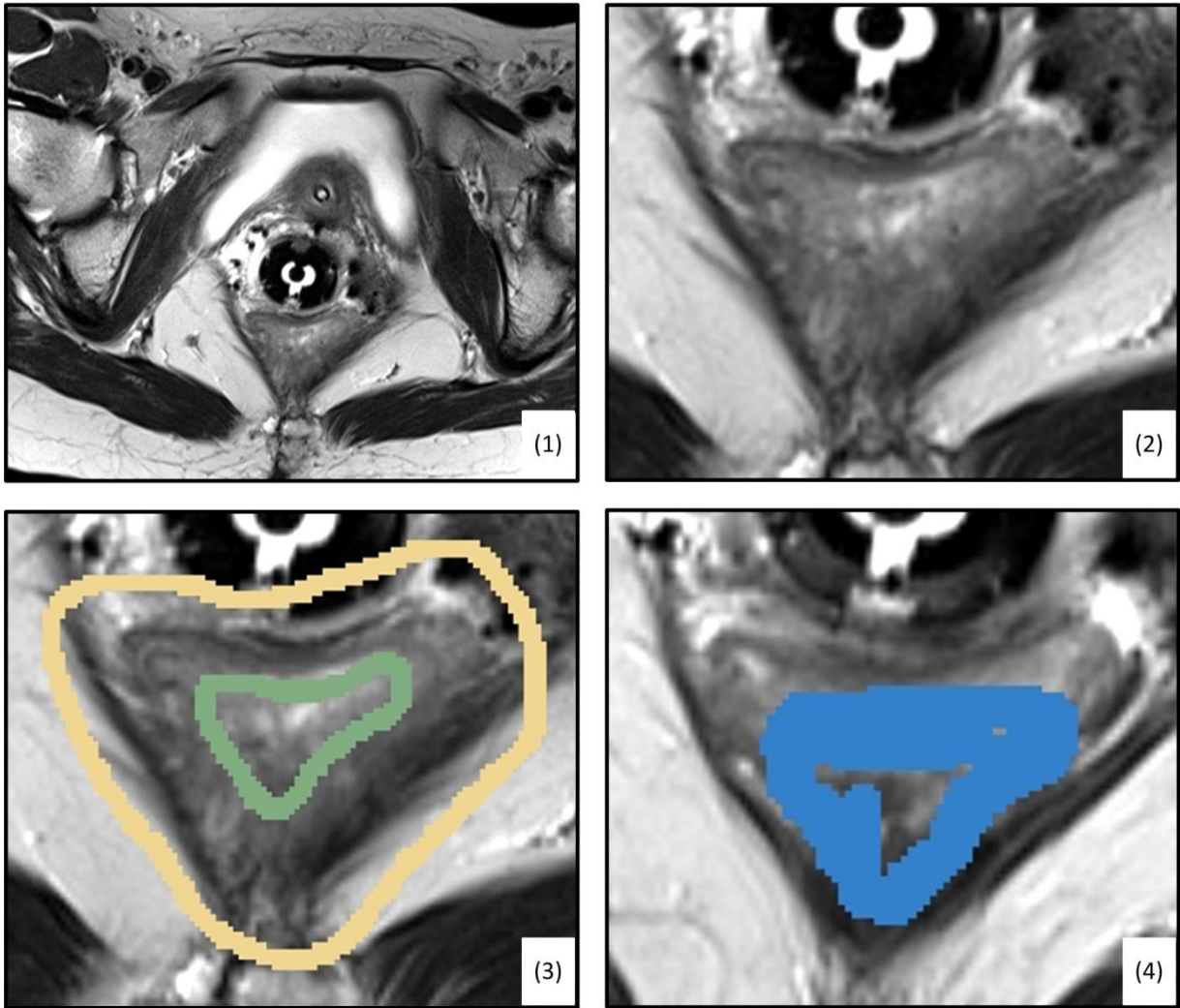


Figure 18: Segmentation of the rectum/sigmoid colon by an active contour model implemented in the 3D Slicer Robust Segmenter tool. (1) Raw image, (2) Cropped region of interest, (3) Initialization with 2 label maps, (background: yellow, object: green), (4) Segmentation result (© TUM-MIMED, 2012, MRI data from (Egger et al., 2012e))

2.3.4 Graph Cuts

Modern computers are capable of handling dexterous computation tasks and it is that nowadays more complex algorithms can be used for image segmentation. One example of those are algorithms based on graphs. They have been applied to various fields such as stereo reconstruction, image segmentation, multiview reconstruction or planar shape matching (Schmidt et al., 2009). In particular several medical imaging segmentation schemes based on graphs have been proposed and employed to brain and other MR images (Egger et al., 2012c) (Egger et al., 2012d) (Wels et al., 2008) (Rother et al., 2004) (Birkbeck et al., 2009).

The basic concept is the modeling of the image as a weighted, undirected graph. The graph's nodes or vertices are represented by pixels or pixel groups and the weights between those nodes are determined by the likeness of neighboring pixels. To separate the object from the

rest of the image a minimal cut is calculated. This is an energy minimization related problem and can be formulated as an instance of a maximum flow problem which in turn is equal to a minimal cut of the graph (Boykov and Jolly, 2001).

The segmentation scheme presented in this thesis is based on graphs and a detailed description follows in chapter 3.

2.3.5 Interactive Methodologies

In this thesis a novel interactive and iterative graph-based segmentation algorithm is presented. The need for interactive segmentation methodologies is rooted in the fact that until today no fully automatic methodology delivers guaranteed robust results (Vezhnevets and Konouchine, 2005). It is therefore that semi-automatic or so called interactive schemes become more and more popular as they allow the user to directly influence the segmentation result where it is particularly hard to calculate for the computer (Birkbeck et al., 2009) (Egger et al., 2012b).

In this chapter various recent interactive methodologies and workflows will be presented. The focus will lie on the realization of interactivity and user workflow methodologies and less on the underlying mathematical algorithms. Moreover, the field of applications is extended from medical images alone to general purposes including photographic applications.

The interactivity of most recent segmentation schemes is limited to initial user-defined scribbles. The user starts by providing several scribbles to define object classes and background areas. The algorithms then calculates a segmentation result which the user can enhance by providing more detail scribbles in areas where the segmentation is difficult and run the algorithm again. This kind of interactive user workflow strongly equals the workflow presented for Grow-Cut (see Chapter 2.3.1) and Robust Statistics Segmenter (see Chapter 2.3.3).

Further examples can be found in the work of: (Boykov and Jolly, 2001) (Artan, 2011) (Delong et al., 2011) (Ding and Yilmaz, 2010) (Kulkarni and Nicolls, 2009) (Nickisch et al., 2010) (Phan and Androutsos, 2011) (Sindeyev and Konushin, 2008) (Wang et al., 2007) (Doria D., 2010) (Lechse, 2007) (Mannan) (Steger and Sakas, 2012).

Little alterations of the described scheme can be found in the work of (Rother et al., 2004) where the user drags a bounding box about the region of interest in a first step. Thereafter the algorithm computes a segmentation result which can be improved by providing user scribbles. In the work of (Steger and Sakas, 2012) the user provides a seed point for a graph-based approach. After the segmentation result is computed, it can be enhanced by detailed user scribbles.

Figure 19 illustrates a workflow where the user provides scribbles to define object classes and background areas.

In the approach of Blake et al. (Blake et al., 2004) the user draws along the object contour with a fat pen tool. The algorithm automatically tries to find the object outline in the given pen trail. Similarly, in the approach presented by Birkbeck et al. (Birkbeck et al., 2009) the user sweeps a brush or lasso tool coarsely along the object contour. The algorithm automatically calculates a segmentation in the underlying trail (see Figure 20, (1)).

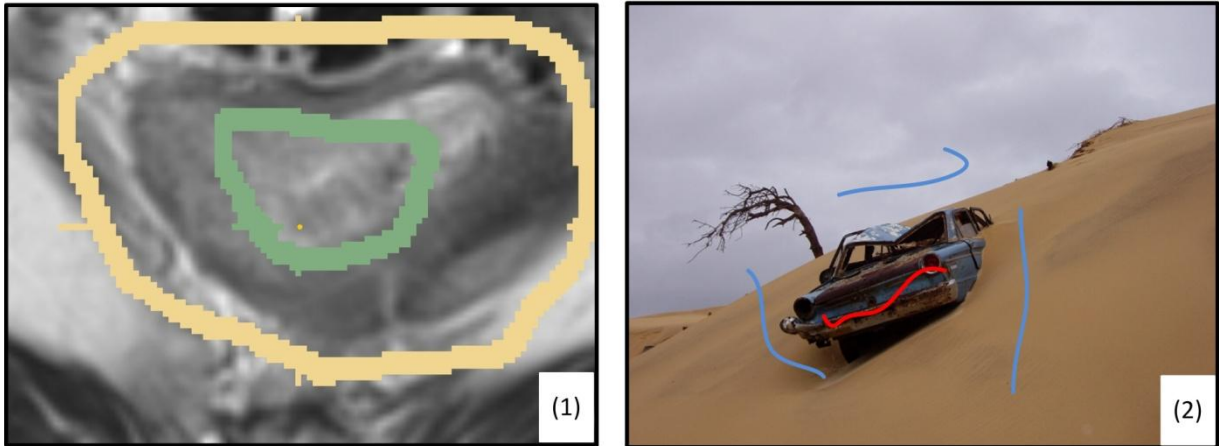


Figure 19: Common interactive segmentation methodologies where the user provides input information by class scribbles: (1) object (green), background (yellow), (2) object (red), background (blue) (© TUM-MIMED, 2012, MRI data from (Egger et al., 2012e))

Jackowski et al. (Jackowski et al., 1999) presented a methodology where in an automatic segmentation scheme based on thresholding an object contour is found. Along the calculated outline so called control points are placed in constant distance. The user can interactively drag those control points to improve the segmentation result (Jackowski et al., 1999) (see Figure 20, (2)).

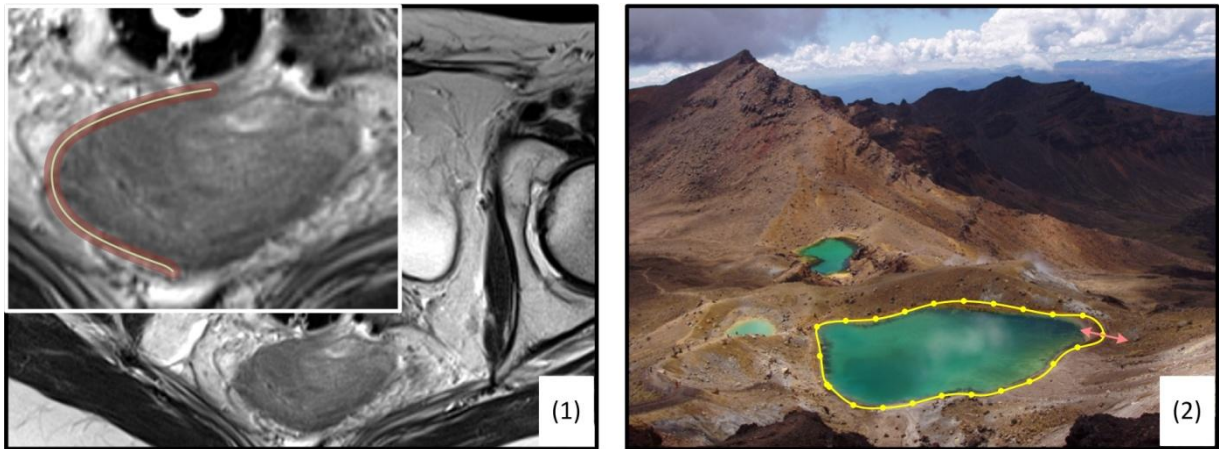


Figure 20: Illustration of interactive segmentation methodologies: (1) The user draws the object contour with fat brush tool, contour is automatically calculated within this trail, (2) User can improve automatic segmentation result (yellow line) by dragging object control points (yellow dots) (© TUM-MIMED, 2012, MRI data from (Egger et al., 2012e))

Although the user can initialize scribble-based algorithms with arbitrary strokes and improve the calculated result with further input scribbles, eventually he has little influence on the computation process or the calculated result. Within the presented methodologies only the approach of Jackowski et al. enables the user to directly influence the resulting object contour.

2.4 Overview

In summary, the stated problem is defined by the absence of computer-assisted tools to support physicians in the progress of segmentation of tumor tissue and organs-at-risk. This leads to a time consuming manual task which every developed tool has to be evaluated against to proof its time-wise benefit. Furthermore, the computer-assisted segmentation area has to be evaluated against manual results regarded as the gold standard to predict its robustness and quality. Various segmentation methodologies have been developed, an overview about their advantageous and disadvantageous will be shortly given here.

Region Growing provides a simple basic concept to perform image segmentation tasks that can be implemented comparatively easily (Kamdi and Krishna, 2011). However, region growing algorithms can become complex in practice and have to be computed iteratively. Thereby, local as well as global calculations have to be performed, which causes each pixel to undergo several examinations and makes those algorithms very computation intensive (Davies, 2012). Another disadvantage of region growing algorithms is leaking, which can be caused by noise or weak, contrast poor edges that cause oversegmentation of an area (Vezhnevets and Konouchine, 2005) (Heimann et al., 2004) (Davies, 2012) (Egger et al., 2012b).

Active appearance models or atlas-based algorithms are advantageous in cases where repeatedly anatomical structures of a similar texture and shape have to be segmented. The use of an atlas can improve the segmentation result where only poor knowledge about pixel intensity relationships are known, e.g. contrast poor edges or noise. Furthermore, they can be advantageous in clinical practices where morphological comparisons between anatomical structures of patients can easily be performed. Disadvantages of atlas-based algorithms are the excessive time to create an atlas, because iterative steps or non-rigid registrations might be necessary (Kalinic) (Cabezas et al., 2011). Additionally, patient to patient shape differences of anatomical structures, e.g. the rectum/sigmoid colon, vastly limit the creation and further benefit of an atlas. Segmentation approaches for malignancies pose another problem, because malignancies such as brain tumors can appear in different locations in arbitrary shapes which makes the creation of a general atlas very difficult.

One advantage of active contours is the mentioned ability to find subjective contours, that are physically not existing (Egger, 2012). Although they are computationally efficient to implement, they might converge to a local minimum instead of finding the global minimum during the iterative segmentation process (Egger, 2012) (Lechsel, 2007).

In contrast to active contours, graph cut algorithms present an efficient way to compute a guaranteed convergence to the minimum of a global energy function (Davies, 2012) (Egger et al., 2012b). One of the disadvantageous is their limited flexibility, because the only changeable parameters are the graph's weights and the cost function (Vezhnevets and Konouchine, 2005).

The user input scribbles as well as presented fat pen tool input provide a simple and intuitive interactive methodology. However, the eventual control over the algorithm and resulting object are very limited, because the outline cannot directly be influenced (Artan, 2011) (DeLong et al., 2011) (Birkbeck et al., 2009) (Blake et al., 2004). Only the approach of Jackowski et al. with its control point methodology provides true control over the segmentation result, because the control points can be manually dragged and placed. On the other hand, more effort is needed until a sufficient result is reached (Jackowski et al., 1999).

Examples of research result are given for vertebra segmentation in Zukic *et al.* (2012) where an average DSC of 78% was achieved and the methodology could be shown to outperform other methodologies. Neubert *et al.* (2011) developed a fully automatic segmentation methodology for vertebral and intervertebral bodies. They considered their result of DSC 85% for vertebra as “very good”, the DSC 81% for intervertebral bodies as “satisfactory”.

In brain image segmentation, Pohl *et al.* (2007) achieved DSC values ranging from 70% - 86% and considered their result as “quite high”. Other results are Babalola *et al.* (2008) with a DSC value of around 80% and Hausdorff distance of 3mm - 14mm, Khotanloua *et al.* (2009) with a DSC of 90% and HD of 4,92mm.. Corso *et al.* (2008) with a HD of 3mm – 127mm.

In Martinez *et al.* (2012) a model based approach on the prostate, bladder and rectum in CT images yielded a Hausdorff distances of 5.98 ± 2.2 mm for the prostate, 19.09 ± 3.1 mm for the urinary bladder and 7.52 ± 2.3 mm for the rectum. The results were considered “reliable” and outperforming the best multi-atlas based approach.

Regarding clinical applications, manual segmentation is considered the gold standard, although it exhibits a high intra- as well as inter-variability and strongly depends on the user’s clinical experience (Bille and Schlegel, 2002) (Chang et al., 2011) (Elsa et al., 2010). Intra analysis of two manual segmentations was also investigated by Egger et al. (2013). For brain tumor images, the DSC value for two versions of the same physician revealed 90%, the comparison among versions of the different physicians revealed 88% and 86%, respectively. Other publications concerning intra observer variability are (Elsa et al., 2010, Letteboer et al., 2004, Prastawa et al., 2004).

The Varian, Inc. Smart SegmentationTM tool could proof its efficiency and time saving potential and is part of the commercially available Eclipse© software for treatment planning. However, in most cases manual corrections of the fully automatic algorithms have to be performed. Furthermore, due to its mostly inhomogeneous appearance the rectum proofed to be especially difficult to segment in a validation through 600 data sets (Haas et al.) (Haas et al., 2008) (Huyskens et al., 2008) (Egger et al., 2012a). In Huyskens *et al.* (2008) the commercially available Varian Inc. Smart Segmentation® tool was evaluated by comparing automatic and manual segmentation results in a first step and asking clinicians to group the automatic result in either *excellent* (no manual modification needed), *good* (limited nr. of slices need modification), *acceptable* (several slices need modification) or *not acceptable* (result considered useless) in the next step. The automatic result which yielded a DSC of 73% for the prostate was considered “good to acceptable”. For the bladder, a DSC of 90% was achieved and the automatic result was considered “excellent to good”. For the rectum, a DSC of 52% was achieved and the automatic result was considered “acceptable to not acceptable”.

In the evaluation of the Varian Inc. Smart Segmentation® tool given in Haas et al. (2008), the time for the algorithm to calculate a result, not including potential manual corrections, is targeted at 2 minutes to represent a time saving potential.

Table 1: Overview of the advantages and disadvantages of clinical applications, segmentation algorithms and interactive methodologies in research

	State of Clinical Applications		State of Research: Segmentation Algorithms				State of Research: Interactive Methodologies		
	Manual	Varian, Inc. Smart Segmentation	Region Growing	Active Appearance Models	Active Contours	Graph Cuts	Scribbles	Pen Tool	Control Points
Advantages	<ul style="list-style-type: none"> Segmentation on gold standard 	<ul style="list-style-type: none"> Efficiency proofed Time saving potential 	<ul style="list-style-type: none"> Simple concept and implementation 	<ul style="list-style-type: none"> Work even with poor knowledge about pixel intensity relationship Mostly applied for repeatedly same structures 	<ul style="list-style-type: none"> Find physically not existing subjective contours Computationally efficient 	<ul style="list-style-type: none"> Efficient computation Guaranteed convergence to minimum of global energy function 	<ul style="list-style-type: none"> Simple input Fast Intuitive 	<ul style="list-style-type: none"> Simple Detailed outlining input possible 	<ul style="list-style-type: none"> Exact control over segmentation result
Disadvantages	<ul style="list-style-type: none"> Time consuming Intra- and inter variability Resource inefficient 	<ul style="list-style-type: none"> Manual corrections have to be performed Segmentation of the rectum especially challenging 	<ul style="list-style-type: none"> Computation intensive Possible leaking at contrast poor contours 	<ul style="list-style-type: none"> Time consuming atlas creation Objects of high shape, location and texture variability 	<ul style="list-style-type: none"> May converge to a local minimum 	<ul style="list-style-type: none"> Low flexibility, only graph's weights and cost function can be altered 	<ul style="list-style-type: none"> Little influence on segmentation result 	<ul style="list-style-type: none"> Limited influence on segmentation result 	<ul style="list-style-type: none"> Relatively time consuming

Citation	(Bille and Schlegel, 2002) (Chang et al., 2011) (Elsa et al., 2010)	(Haas et al.) (Haas et al., 2008) (Huyskens et al., 2008)	(Davies, 2012) (Jähne, 2005) (Heimann et al., 2004) (Vezhnevets and Konouchine, 2005)	(Pohl et al., 2007) (Kalinic) (Cabezas et al., 2011)	(Gao et al., 2012) (Egger, 2012) (Lechsel, 2007)	(Egger et al., 2012c) (Wels et al., 2008) (Boykov and Jolly, 2001)	(Artan, 2011) (DeLong et al., 2011) (Ding and Yilmaz, 2010)	(Birkbeck et al., 2009) (Blake et al., 2004)	(Jackowski et al., 1999)
-----------------	---------------------------------------------------------------------	-----------------------------------------------------------	---------------------------------------------------------------------------------------	------------------------------------------------------	--------------------------------------------------	--------------------------------------------------------------------	-------------------------------------------------------------	----------------------------------------------	--------------------------

3 Interactive Graph-Based Segmentation

3.1 Task Definition

As described in section 2.1.2 and section 2.1.3, in the course of Image Guided Interstitial Brachytherapy particularly and Radiology Treatment Planning in general, a crucial step in planning the applied amount and distribution of radiation is the segmentation of the tumor and adjacent organs-at-risk potentially exposed to radiation. With the gained 3D information of the tumor and adjacent Organs-At-Risk the positioning of the interstitial brachytherapy needles is controlled and the loading with individual radiation sources of each needle is calculated to accomplish an optimal radiation distribution on the tumor while sparing or limiting exposition to radiation for the Organs-At-Risk. This delineation of anatomical structures is mostly conducted manually by a physician with little computer assistance and represents a time-consuming task in the progress of planning radiological treatments.

Due to its inhomogeneous appearance, the rectum/sigmoid colon as an organ-at-risk, has proven to be challenging to segment for fully automatic segmentation tools. Therefore, the rectum/sigmoid colon is segmented manually in clinical daily routine which represents a time and resource consuming task. To support clinicians in the course of this delineation, the aim of this thesis is to develop an interactive segmentation methodology for the rectum/sigmoid colon.

The methodology is based on a graph network which by virtue of a calculated minimal cut through the graph network can find the object outline. As most fully automatic segmentation tools struggle with leaking in the progress of the segmentation of the rectum/sigmoid colon, the methodology has to show robustness and limitedness to leaking effects. Additionally, it has to allow direct and comprehensive control over the segmentation result in each slice by simple user interactions to improve the segmentation result where the algorithm is challenged.

The evaluation of the segmentation methodology will be done by the Dice Similarity Coefficient (DSC) and Hausdorff distance (HD). For segmentation algorithms in the medical imaging domain DSC values of around 80% are common and considered successful (see section 2.3.5)

In regard of the values mentioned in section 2.4 common for the medical imaging domain and the results of Martinez *et al.* (2012) and Huyskens *et al.* (2008) directly considering the rectum, a DSC result of around 80% and HD of 7,5 mm can be considered successful. Furthermore, in the evaluation of the Varian Inc. Smart Segmentation® tool given in Haas *et al.* (2008), the time for the algorithm to calculate a result, not including potential manual corrections, is targeted at 2 minutes to represent a time saving potential.

3.2 Expected Advantages and Characteristics

Fulfillment of the formerly mentioned requirements will cause a valuable time saving potential and thereby discharge from tedious manual segmentation tasks for the performing clinician. Eventually, it will open the clinician time for direct patient treatment, than monotonous delineation tasks.

With workload time saving for the clinician comes saving of costs for expensive medical human resources in the medical sector.

Interactivity, few parameter inputs and direct control over the segmentation result by simple user interactions can increase the acceptance of segmentation tools among clinical personal and increase their use in daily clinical routine. Until today segmentation tools often lack those features and are complex in their handling methodologies because of extensive numbers of input parameters and demand excessive initial training.

The developed methodology can be transferred to other fields of segmentation in the medical compound that proved to be challenging to segment, e.g. gynecological tumors or brain tumors. A more general context of application could be object segmentation in digital videos or photo sequences.

3.3 Solution Structure

In this section the basic concept of the developed segmentation scheme will be described generally. The following section 3.4 will describe the computational implementation and mathematical principles in further detail.

Figure 21 illustrates the first steps of the algorithm. For a given object to segment (1), the user traces the object outline purely manual (2). The drawn contour (yellow) will be scaled by a specific factor and serve as template for a next slice where the segmentation is performed semi-automatically (3).

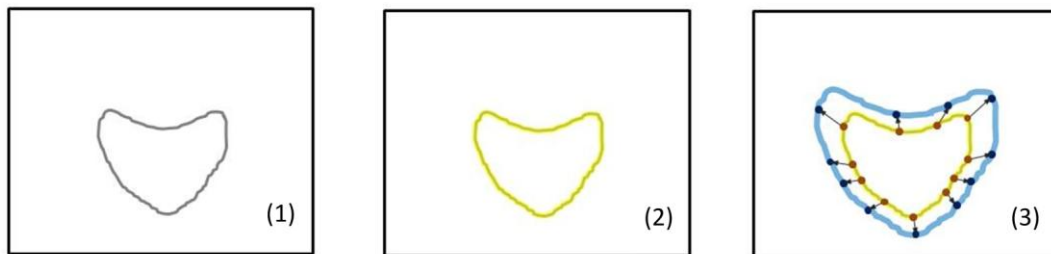


Figure 21: Object outline (1), drawn user contour (2), scaled user contour serving as template (3) (© TUM-MIMED, 2012)

After the contour has been drawn and scaled, the user skips to a next slice where a deviation from the drawn contour occurs (see Figure 22 (4)). The user sets a seed point which determines the template position (5). With the information of the seed point and template a segmentation result is calculated based on an underlying graph network (6).

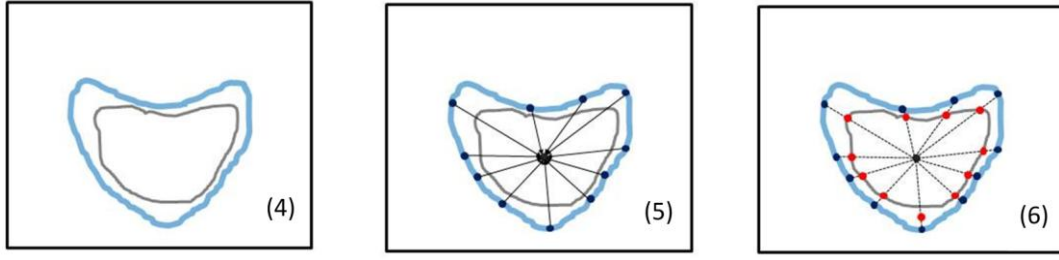


Figure 22: Scaled contour serves as template for a segmentation (4), template position is determined by user-defined seed point (5), segmenation result is calculated (6) (© TUM-MIMED, 2012)

The calculated segmentation contour (see Figure 23 (7)) will serve as template for the segmentation in a next slice (8). The basic idea of this methodology is to dynamically adopt the template which frames the area where the segmentation is performed. The dynamic process of the template starts with the user-drawn contour in the first slice and alters its shape depending on the segmentation result in successive image slices. This methodology enables the algorithm to adapt to altering object shapes in the region of interest (ROI), but also to spare disturbing objects from the ROI.

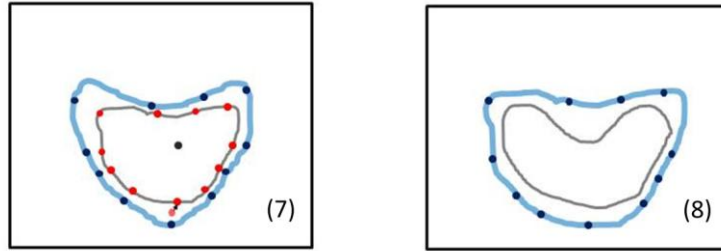


Figure 23: The calculated segmentation result (grey) (7) is scaled and serves as template for a next segmentation (blue) (8) (© TUM-MIMED, 2012)

3.4 Solution Processes

This section will go into detail of the implemented processes and further explain the user work flow (see section 3.4.1) and the structure of the implemented network (see section 3.4.2). Furthermore, the information flow of the presented methodology (see section 3.4.3) and source code structure (see section 3.4.4) are explained in detail. Thereafter follows a description of the underlying mathematical implementations of graph networks (see section 3.4.5) and its application on the image segmentation task (see section 3.4.6).

3.4.1 User Workflow

The user workflow of the presented segmentation algorithm consists of several steps and is fully illustrated in Figure 24.

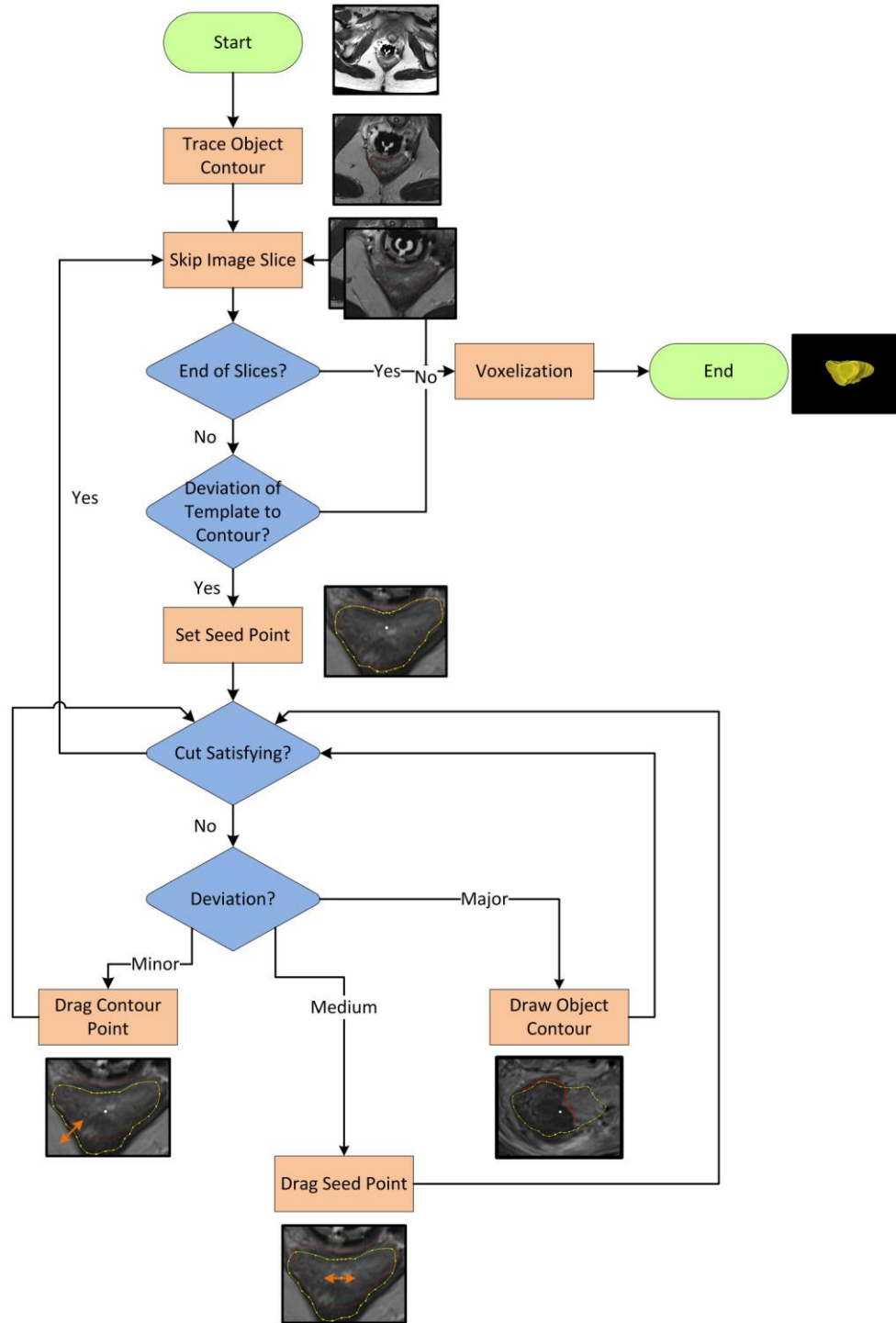


Figure 24: User workflow of the presented interactive segmentation algorithm. First, the user traces the object contour. Second, the user skips to a next slice and determines if a deviation to the drawn contour occurs. If not, the user skips to a next slice. If yes, a seed point is set and cut calculated. If the result is satisfying the user skips to a next. If not, the user can either drag a contour point, drag the seed point or reinitialize by redrawing the object contour (© TUM-MIMED, 2012)

First, the user traces the complete contour of the target object in clockwise or counter clockwise direction. Figure 25 illustrates this step in an exemplary slice $i=0$, where $0 < x < y < z < v < n$ with n being the number of all object slices.

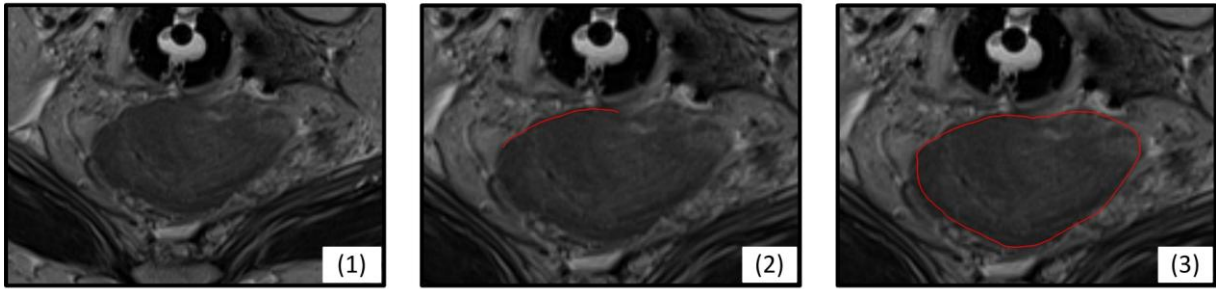
Slice 0 :

Figure 25: User traces object outline in slice nr. 0, (1) – (3) (© TUM-MIMED, 2012, MRI data from (Egger et al., 2012e))

Thereafter, the user skips to a next slice $0 + x$ or $0 + y$ (see Figure 26, (4), (5)) where either the end of the segmentation process can be determined if no further segmentation is necessary or the segmentation process can be continued. If the end is not reached yet, the user continues and has to evaluate if the drawn contour deviates from the object outline in the current slice. Therefore, the user drawn contour is shown in various slices deep to enable easy comparison.

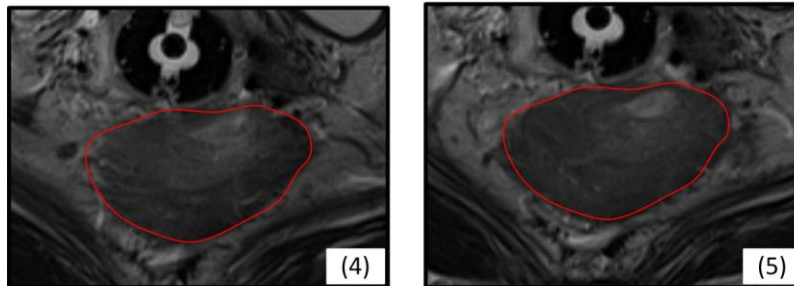
*Slice 0 + x :**Slice 0 + y :*

Figure 26: User skips slices where no noteworthy deviation from the last contour occurs (© TUM-MIMED, 2012, MRI data from (Egger et al., 2012e))

If no noteworthy deviation occurs, the user skips to the next slice. This feature is particularly important in the context of comparatively small images slice thicknesses, e.g. 1.6mm. With a small image slice thickness, the change in shape of the object is relatively limited from one slice to another which makes skipping of slices, where no large change in shape occurs, a valuable time saving feature in the segmentation process.

If the user skips through the slices and reaches a slice where a deviation occurs (e.g. Figure 27 (6)), a seed point can be set (7) and cause the algorithm to calculate a segmentation (8). At this stage, the user can choose between 4 different options. In the ideal scenario the calculated cut is satisfactory and the user can complete the segmentation of this slice by skipping to the next slice.

In case medium size segmentation mismatches occur, the user can interactively drag the seed point, which causes the algorithm to compute another segmentation result (see Figure 27 (9), (10)). If a satisfactory result was computed, the user continues by skipping. This option represents the most frequent type of improvement. If further improvements are necessary, the user can drag the seed point again, or employ additional options of improvement.

In case minor segmentation mismatches occur at a particular location, the user can interactively drag a contour point and improve the segmentation result (see Figure 27 (10), (11)). If thereafter the segmentation result is satisfactory, the user continues by skipping to the next slice. If the result demands improvements, further enhancements can be employed.

Slice 0 + z :

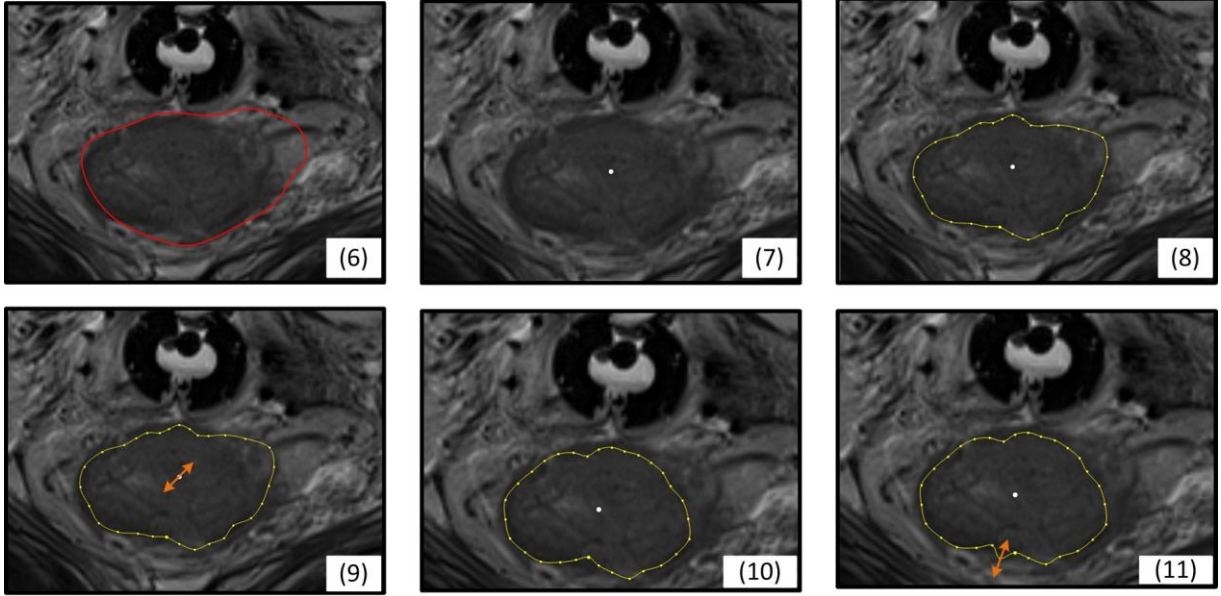


Figure 27: Deviation from the previous contour (6), user sets seed point (7), segmentation is calculated (8), improvement by interactive dragging of seed point (9), new calculated segmentation result (10), interactive improvement of contour by dragging contour control point (11)) (© TUM-MIMED, 2012, MRI data from (Egger et al., 2012e))

In case of major segmentation mismatches (see Figure 28 (12)), the user can outline the object again in the current slice and thus reinitialize the algorithm (see Figure 28 (13), (14)). This option of improvement rarely occurs and might merely be necessary where the object shape vastly changes from one slice to another, especially at locations where the organ bends from the image z -axis directing through the image slices.

Slice 0 + v :

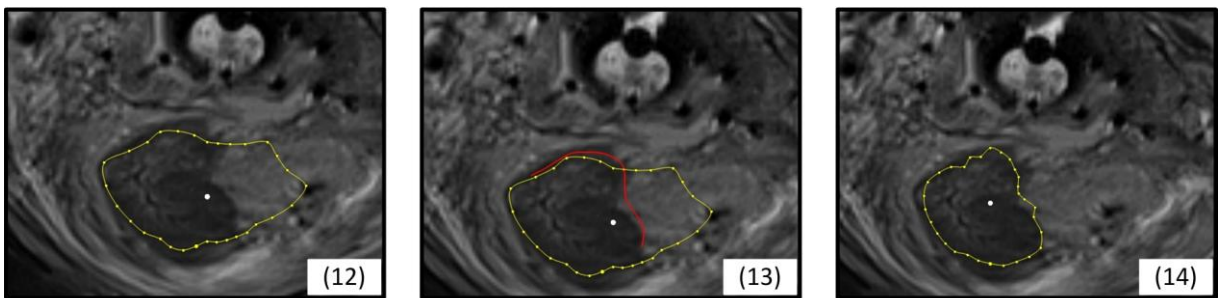


Figure 28: Major deviation of the segmentation result from the object outline (12), reinitialization by drawing new object outline (13), new segmentation result (14)) (© TUM-MIMED, 2012, MRI data from (Egger et al., 2012e))

After a satisfactory segmentation result was found and the user skips to a next slice, the last calculated object contour serves as reference to determine a deviation to the current slice.

After all slices where the object appears have been segmented, the user completes the segmentation process by automatic interpolation of the skipped slices and voxelization of the final object.

3.4.2 System Overview

The developed segmentation algorithm consists of two main components illustrated in Figure 29. The main component is a C++ project *InteractiveCut* developed in Microsoft Visual Studio which realizes the graph cut approach as well as parts of the interactive methodology. In the C++ project embedded is the publicly available max flow/min cut library developed by Boykov and Kolmogorov (Boykov and Kolmogorov, 2004) (Kolmogorov, 2010). It provides several classes and methods to setup a graph network and eventually calculate a minimal cut of the given network. The algorithm is further described in section 3.4.5.

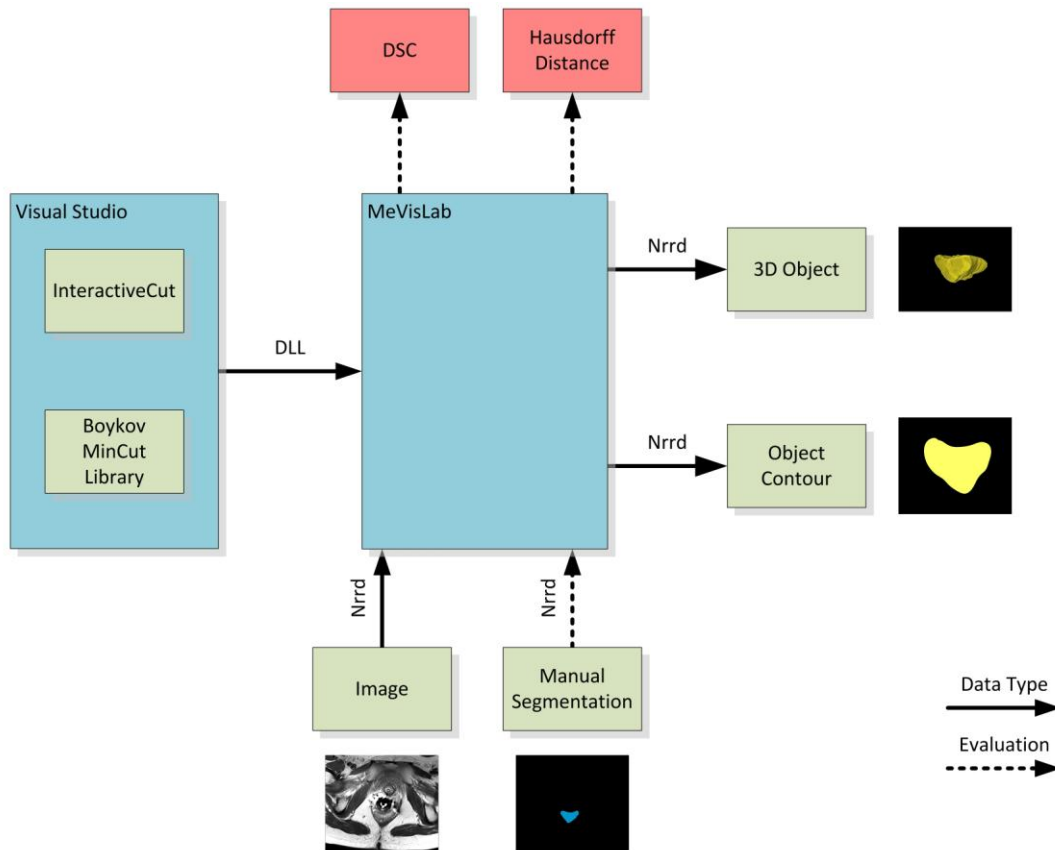


Figure 29: System overview: The C++ codes of the *InteractiveCut* and *Boykov Library* are implemented in a Microsoft Visual Studio project, which is embedded in a *MeVisLab* network. The *MeVisLab* network imports the image and manual segmentation and exports the object contour and voxelized 3D object (© TUM-MIMED, 2013)

The *InteractiveCut* source code is embedded into a *MeVisLab*® (*MeVisLab*, 2012) network environment. *MeVisLab* provides a modular framework for the development of medical image processing and visualization tasks. New C++ algorithms such as the *InteractiveCut* code can be integrated into *MeVisLab* through a *Dynamic Link Library* (DLL) file. The *MeVisLab* network loads the image file as a *Nearly Raw Raster Data* (Nrrd) file. The

segmentation results in form of the object contour slices and voxelized 3D object are exported as Nrrd files as well.

For evaluation purposes of the segmentation algorithm, additional manual segmentation data can be imported as Nrrd file and compared to the algorithmic segmentation. Results are a Dice Similarity Coefficient as well as Hausdorff distance. Both coefficients are further described in section 4.1.

3.4.3 Network

The network implementation is based on MeVisLab® version 2.3.1 with Qt version 4.8.0 (MeVisLab, 2012). The MeVisLab network is structured in seven distinct groups which consist of predefined MeVisLab modules. The complete network is given in Figure 30.

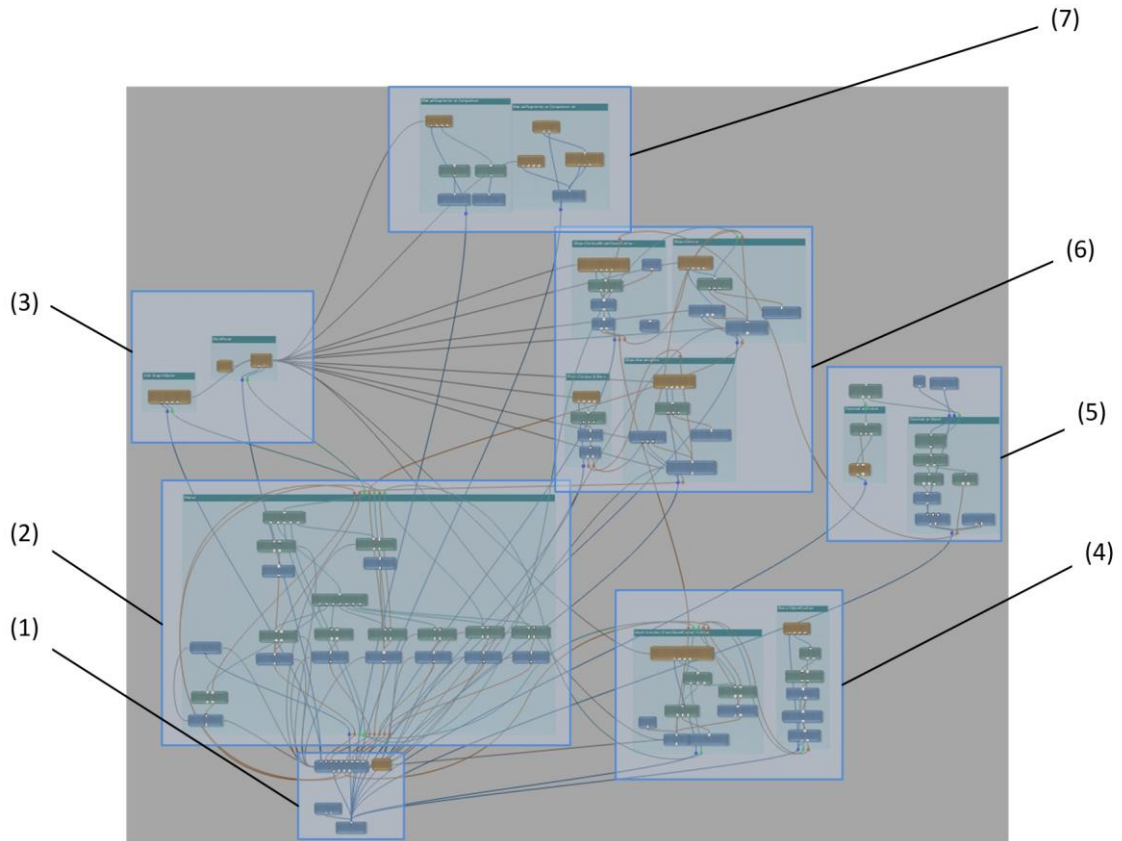


Figure 30: Implemented MeVisLab® network consisting of 7 distinct groups (© TUM-MIMED, 2013)

The network modules generate a specific information flow through the network which handles all user interactions and segmentation calculations. Figure 31 presents an illustration of this information flow through the network.

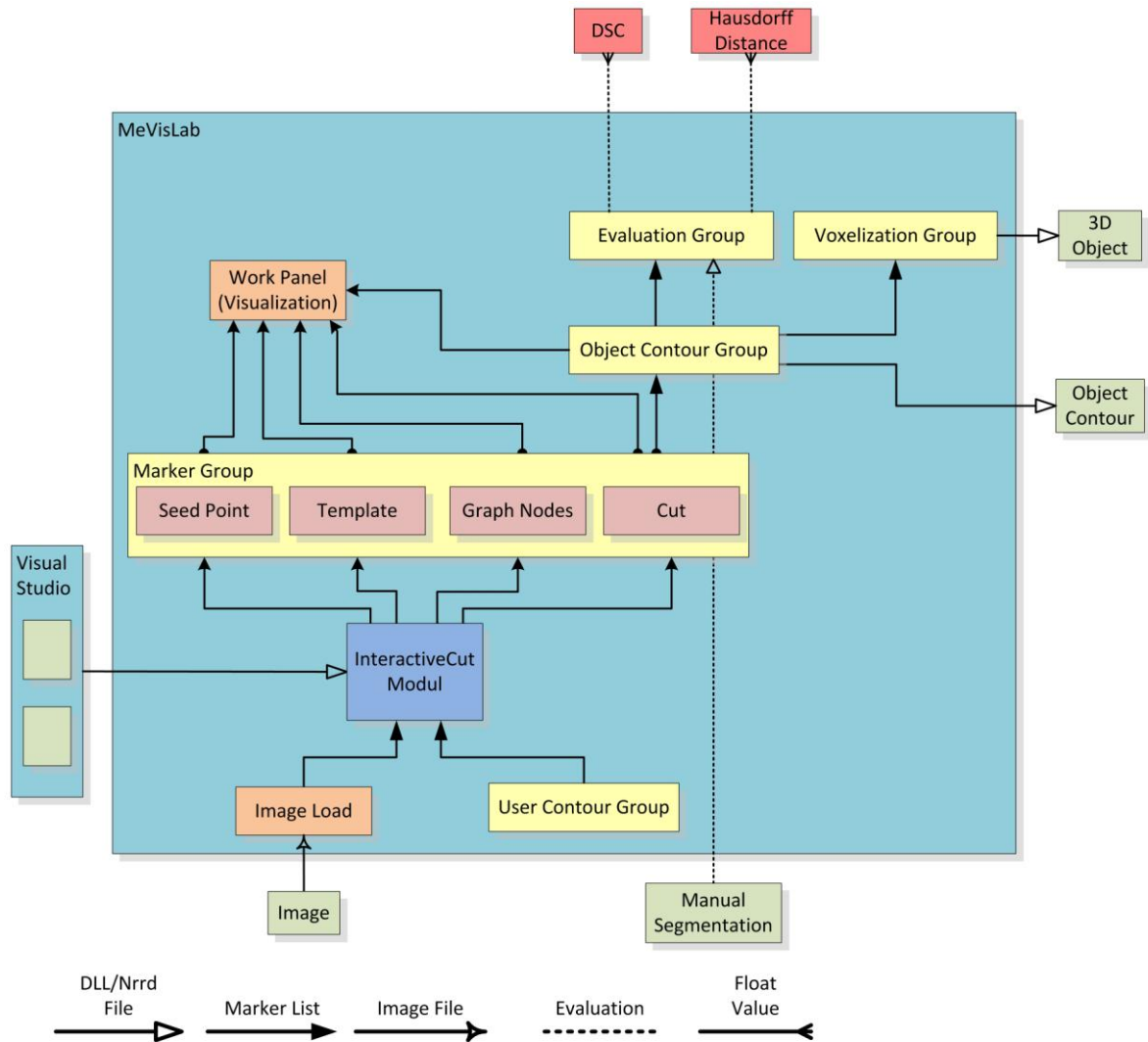


Figure 31: Illustration of the implemented MeVisLab® network and information flow (© TUM-MIMED, 2013)

The information flow is as following. After the image file is loaded, the image is transferred to the *InteractiveCut* module. This module represents the core of the network and incorporates the C++ code via *dll* file. Besides the image file input, the module imports a *markerlist* representing the user drawn contour from the *User Contour* group. A *markerlist* is a MeVisLab specific class which handles arrays of 3D vector positions.

The *User Contour* group (see Figure 32) handles all information exchange between the user and the *InteractiveCut* module (see Figure 34). For instance, it transforms the contour drawn by the user into a polygon consisting of vertices which are passed to the *InteractiveCut* module as *markerlist*. The group also handles the user provided seed point position and interactive seed point movements and passes this information to the *InteractiveCut* module. It also updates the graph template shape in case the object contour points are dragged for improvement.

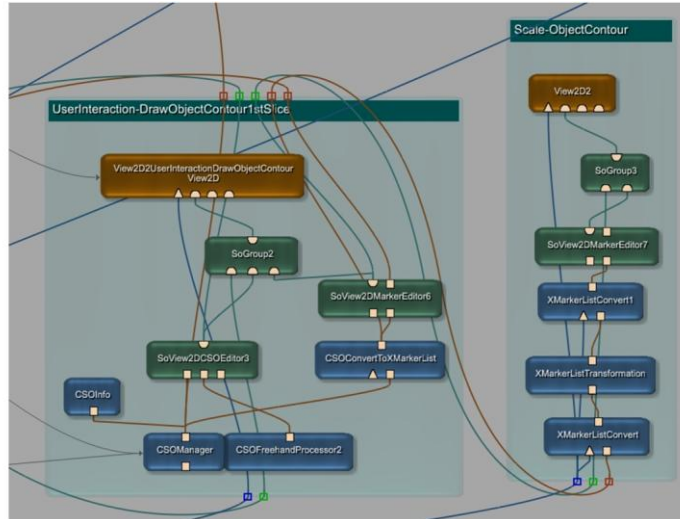


Figure 32: *User Contour* group (4) handling user interactions (© TUM-MIMED, 2013)

With the information of the image, the user drawn contour and a given 3D seed point position, the *Interactive Cut* module generates a graph network with the provided seed point at its origin and the shape of the user drawn contour. Thereafter, according to the graphs nodes, image voxel grey values are sampled and the graphs edges weights are determined. The weighted graph is then evaluated by the Boykov max flow/min cut algorithm to calculate the object segmentation. The *InteractiveCut* module's calculated segmentation result is passed back to the network into the *Marker* group (see Figure 33). The output comprises several *markerlists* including the current seed point, the graph template inherited from the user drawn contour, the graph nodes and finally the graph nodes which are part of the calculated *cut*.

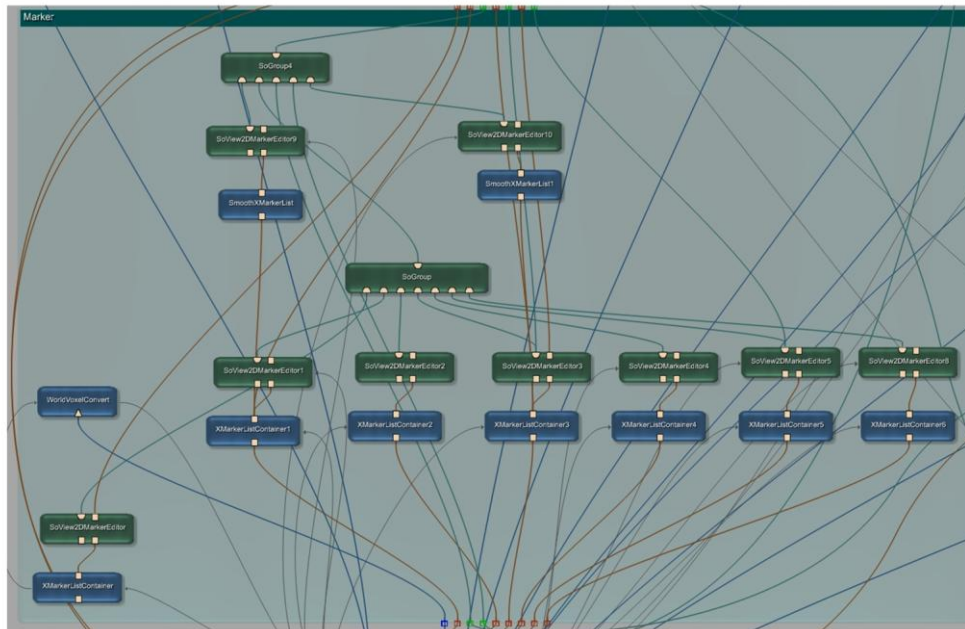


Figure 33: *Marker* group (2) handling all calculated marker outputs (© TUM-MIMED, 2013)

The *cut* nodes are passed to the *Object Contour* group, which generates a *contour segmentation object* (CSO) from the *cut markerlist* and handles all updates in case of seed point or contour point dragging. The sum of all generated CSOs is stored in a CSO list. After

all slices have been segmented, an automatic interpolation is applied to the CSO list to generate CSOs in slices which have been skipped by the user. The final CSO list is stored as segmentation result. It is also passed to the *Voxelization* group which renders the CSO list in a 3D object.

The *Work Panel* module handles all visualizations. In this module the image is shown as well as seed points and segmentation results. Furthermore, the *Work Panel* module handles all user interactions. Here, the user draws the object contour, but also performs all improvements of the segmentation result in form of dragging the seed point, dragging the object contour points or reinitializing the algorithm with a new user drawn contour.

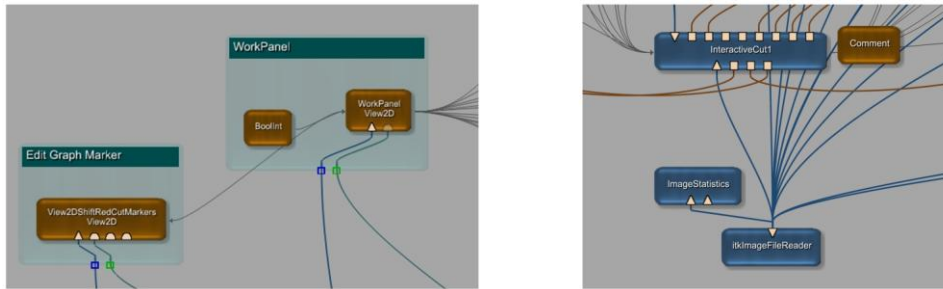


Figure 34: *Work Panel* (3) group, *InteractiveCut* modul and *Image load* modul (1) (© TUM-MIMED, 2013)

For evaluation purposes the *Evaluation* group receives the sum of all object contours in form of a CSO list and evaluates it against the provided manual segmentation data to calculate a DSC value and Hausdorff distance. The DSC value and Hausdorff distance, together with their implementations are described further in section 4.1.

3.4.4 InteractiveCut Module

The *InteractiveCut* module C++ source code can be partitioned in several distinct states where each state fulfills a specific task and executes individual functions. The module itself is designed as observer module where a MeVisLab specific method (*handle notification*) is called each time on changes of the input fields. This enables the design of the interactive user workflow. Depending on the user input, the program transits from one state to another to fulfill the segmentation task (see Figure 35).

The sequence starts and transits into the *Get User Contour* state as soon as the *User Drawn Contour* is available. The *GetUserContour()* function loads and casts the input contour. Additionally, a flag *TemplateFlag* is set *false* to indicate the use of the user drawn contour as graph template.

At the time the user has skipped slices and set a seed point, the program transits into the *Get Template* state. Here, the *GetTemplate(TemplateFlag)* function, depending on *TemplateFlag*, decides if the user drawn contour or last *cut* contour is used as template. On the state exit, *TemplateFlag* is set *true* to enable the use of the calculated *cut* as template in a next slice.

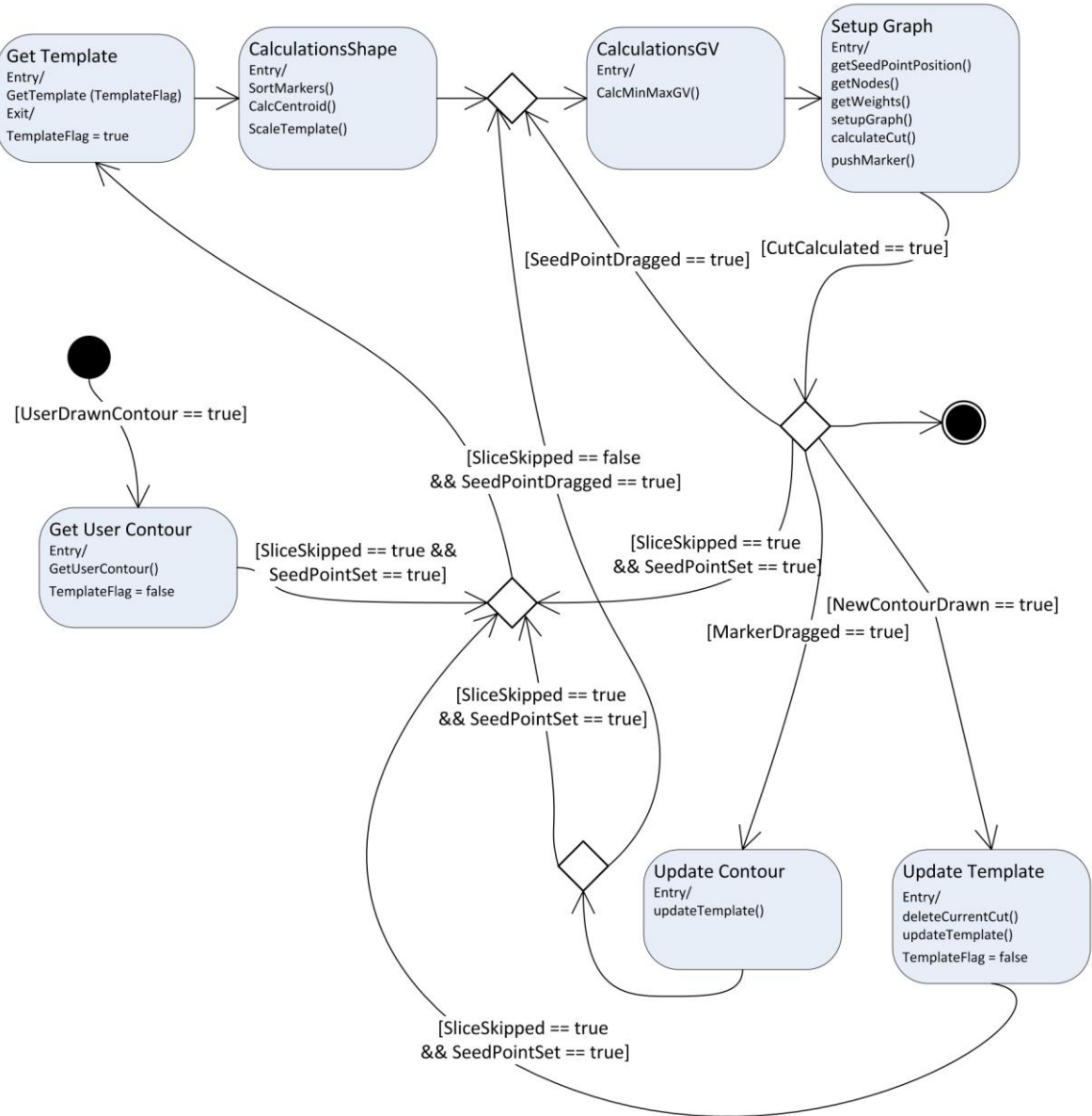


Figure 35: State transition diagram of the implemented *InteractiveCut* source code (© TUM-MIMED, 2013)

The state *Calculations Shape* performs various calculations on the provided contour, which are described in detail in section 3.4.6. First, all the contour markers are sorted in clockwise order. Thereafter, the centroid of the contour polygon is calculated to determine the seed point position. From the seed point position the contour is scaled homogenously in the x - y -plane which results in the actually shape of the graph template.

With the information of the seed point and template position, the state *Calculations GV* samples grey values in the seed point area and template location to gather information of the object grey value distribution. Those values are used to determine the graphs weights in the next state.

In state *Setup Graph*, the current seed point position is specified in a first step. Thereafter, the nodes of the graph are distributed to create the graph network over the image. The edges between the graph's nodes are weighted depending on sampled GV between those nodes.

After the creation of the graph network, it is passed to the Boykov library where the minimal cut is calculated. The calculated minimal cut result is pushed back to the MeVisLab network as *markerlist*, together with the seed point, template and graph node *markerlists*. If the cut is calculated successfully, the program waits for further user input.

In case the seed point is dragged for improvement, the program switches back to the *Setup Graph* state where a new graph network is created depending on the new seed point position. Note that the graph template stays the same, although its location is altered depending on the seed point shift.

In case a contour marker is dragged, the contour is updated externally in the MeVisLab network. However, the template shape is updated, such that the altered shape of the segmentation result is used as template in a next slice. Thereafter, if the *cut* is not satisfying the user can drag the seed point to generate a new *cut*. In case the *cut* was satisfying the user continues to a next slice.

In case a new contour is drawn by the user, the current template is deleted and the new contour drawn by the user is taken over as (new) template. Additionally, the flag *Template Flag* is set *false* so that the user drawn contour is taken as template instead of the last *cut*.

As soon as a satisfying *cut* is calculated the user continues the segmentation process by skipping to a next image slice and setting a new seed point. Thereafter, the program transits into the *Get Template* state where the type of template is determined depending on the *Template Flag* and the formerly described process repeats in the current slice.

3.4.5 Graph Networks

The following section describes the mathematical principles of graph theory this thesis is based on. A particular focus lies on simple, undirected graph networks, the paradigm of max flow/minimal cuts through a graph network and the applied algorithm to calculate minimal cuts.

A graph is defined by a pair $G = (V, E)$ consisting of a finite set of $V \neq \emptyset$ and a set of $E \neq \emptyset$ of two element subsets of V . Thereby, the elements v of the set V represent the vertices or nodes of the graph and are referred to as $V(G)$. The elements e of E represent the edges linking two vertices, whereby $e_i = \{v_x, v_y\}$. The set of edges of a Graph G is referred to $E(G)$. The number of vertices in a graph is denoted by $n = |V|$ and the number of edges by $m = |E|$ (Jungnickel, 2005). A common way to picture a graph is by depicting vertices as dots and to connect vertices by lines to depict edges (Gibbons, 1985).

Simple, undirected graphs

An edge $e = \{v_x, v_y\}$ is considered a self-loop if $v_x = v_y$. A parallel edge cannot be specified by its vertices alone, but only by its order. In Figure 36 (right) a graph with a self-loop and a parallel edge is shown. A graph is called a multi graph if the graph contains parallel or self loops. It is called a simple graph if it does not contain parallel edges or self loops (Gibbons, 1985).

In some cases it is advantageous to assign a direction to each edge of a graph. This is called a directed graph. A simple, directed graph consists of an ordered pair $(V(G), E(G))$ where $E(G) \subseteq V(G) \times V(G)$. If a simple, directed graph fulfills:

$$(v_x, v_y) \in E(G) \leftrightarrow (v_y, v_x) \in E(G) \quad (3.1)$$

it is a simple, undirected graph (Knauer, 2011) (Figure 36 (left)). The course of this thesis will be restricted to simple, undirected graphs.

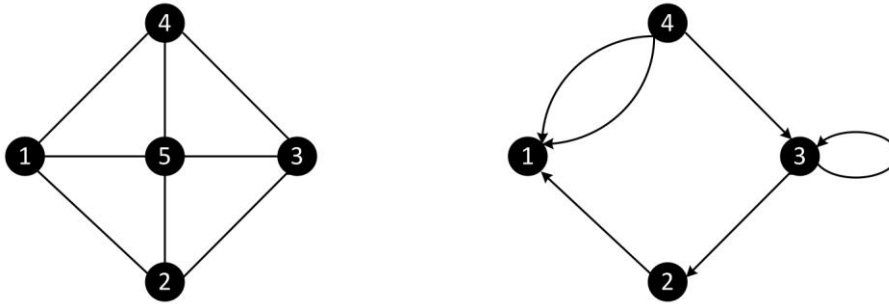


Figure 36: Illustration of a simple, undirected graph with $n = 5$ nodes and $m = 7$ edges (left) and a multi, directed graph with a parallel edge and a self loop, $n = 4$ nodes and $m = 6$ edges (right) (© TUM-MIMED, 2013)

Paths and Connectedness

Let (e_1, \dots, e_n) be a sequence E^* of edges in a graph G . If there is a sequence of vertices (v_0, \dots, v_n) , where $e_i = \{v_{i-1}, v_i\}$ for $i = 1, \dots, n$, then E^* is called a walk. If furthermore $v_0 = v_n$, the walk is called a closed walk. In a sequence E^* , where e_i is distinct, the walk is called a trail. In case a closed walk exhibits distinct edges, the closed walk is called a closed trail. In a sequence E^* not only e_i but also v_j might be distinct, what makes the trail a so called path. A closed trail where $n \geq 3$ and v_j are distinct, excluding $v_0 = v_n$, is defined as a cycle. Regarding Figure 36 (left), the set of $(1, 4, 3, 5, 4, 3)$ represents a walk. In contrast $(1, 4, 5, 2, 3, 5)$ is a trail. The set of $(1, 4, 3, 5)$ is a path and $(1, 4, 3, 5, 2, 1)$ is a cycle. To denote the length of any of the presented cases the notation

$$W: v_0 \xrightarrow{e_1} v_1 \xrightarrow{e_2} v_2 \dots v_{n-1} \xrightarrow{e_n} v_n \quad (3.2)$$

where n represents the length of W .

The concept of connectivity is a basic idea of graphs and closely related to network flow problems and graph cuts, which are described in following sections. A graph $G \neq \emptyset$ is considered connected if any pair of vertices out of the set $V(G)$ can be linked by a path. In case all possible pairs of vertices of G can be linked by a path, then the graph G itself is

called connected. If two vertices (v_x, v_y) are connected by a path of length $n = 1$ (a single edge), then those vertices (v_x, v_y) are called adjacent (Jungnickel, 2005, Diestel, 2005).

For a given graph $G(V, E)$ a subgraph is defined as a graph H such that $V(H) \subseteq V(G)$ and $E(H) \subseteq E(G)$ and edges in H are assigned in the same manner than in G , then H is called a subgraph of G and denoted $H \subseteq G$. A connected component G_s of G is defined by a subgraph with a set of vertices $V_s \subseteq V$ and set of edges $E_s \subseteq E$, which fulfills two properties: G_s itself is connected and $\forall e(v_x, v_y) \in E_s : v_x, v_y \notin V - V_s$ (Jungnickel, 2005, Diestel, 2005). Figure 37 illustrates a graph $G(V)$ with $V = (1, 2, 3, 4, 5, 6, 7, 8)$ and a subgraph $G_s(V_s)$ with $V_s = (3, 5, 6)$. Graph G itself is not connected, however it consist of two connected components defined by the vertices $(7, 8) \in V$ and $(1, 2, 3, 4, 5, 6) \in V$ (West, 2001).

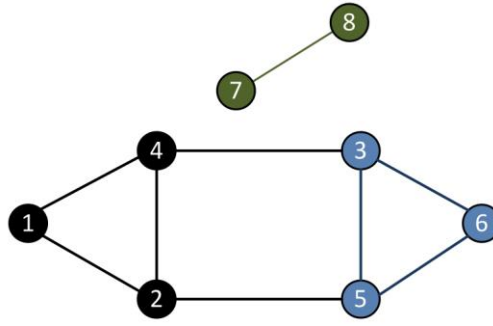


Figure 37: A simple, undirected Graph G consisting of two connected components $(1, 2, 3, 4, 5, 6)$ and $(7, 8)$. Note that the G itself is not connected. The set of vertices $(3, 5, 6)$ represent a subgraph of G (© TUM-MIMED, 2013)

Networks and Flows

A graph $G(V, E)$ can be interpreted as a network, where a specific amount of flow $f(v_x, v_y)$, mapping $f : V(G) \times V(G) \rightarrow \mathbb{R}_0^+$, is carried from one node to another. Each edge $e(v_x, v_y) \in E(G)$ has an upper limit of flow that can pass the edge, defined by a capacity $c(v_x, v_y)$, mapping $c : V(G) \times V(G) \rightarrow \mathbb{R}_0^+$ (Diestel, 2005).

In a flow network there are two distinct vertices seen as the start and end point. At these points flow will enter and leave the network. The start vertex is denoted as *source* s , where the flow of material starts. The end vertex is denoted as *sink* t , where flow material arrives after passing the network (Gibbons, 1985) (see Figure 38).

For consistency, a network has to fulfill several conditions. First, for any vertex $v_y \neq s, t$ the amount of flow entering and leaving v_y has to be equal and thus:

$$\sum_{v_y \in V(G)} f(v_x, v_y) = 0 \quad (3.3)$$

Second, flow in direction $v_x \rightarrow v_y$ has to be denoted negatively in the opposite direction $v_y \rightarrow v_x$, thus:

$$f(v_x, v_y) = -f(v_y, v_x) \quad (3.4)$$

Third, the flow in an edge $e(v_x, v_y)$ can never exceed its capacity $c(v_x, v_y)$, thus:

$$f(v_x, v_y) \leq c(v_x, v_y) \quad (3.5)$$

The overall value of flow $F(G)$ for a network $G(V, E)$ is defined by the net flow leaving the source s :

$$F(G) = \sum_{v_x \in V} f(s, v_x) - \sum_{v_x \in V} f(v_x, s) \quad (3.6)$$

The maximum flow of a network describes a problem where flows $f(v_x, v_y)$ shall be assigned to all edges of $G(V, E)$ such that the above given conditions apply and the flow $F(G)$ from the source to the sink is maximized (Gibbons, 1985).

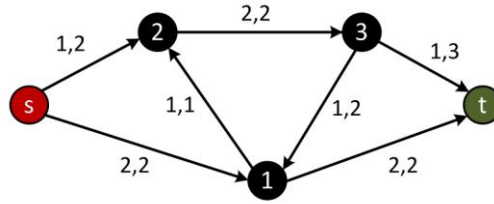


Figure 38: Example of a flow network with the *source* s and *sink* t . The flows and capacities are denoted by $f(v_x, v_y), c(v_x, v_y)$ (© TUM-MIMED, 2013)

Graph Cuts

In terms of graph theory, an s - t -cut or *cut* separates the vertices $V(G)$ of a graph G into two disjoint subsets. The subsets consist of a set S related to the *source* s and a set T related to the *sink* t . The cut is denoted by $C = (S, T) : s \in S, t \in T \wedge S \cap T = \emptyset \wedge S \cup T = V(G)$. The cut-set C_{ST} of a cut describes edges whose vertices are part of the set S and the set T and is described by the cut $C = (S, T)$ where $\{(v_x, v_y) \in E(G) \mid v_x \in S, v_y \in T\}$. The capacity of a cut C denoted by $cap(S, T)$ is given by the total sum of the capacities of the edges of the cut-set C_{ST} leaving S (Boykov and Veksler, 2006) (West, 2001) (see Figure 39):

$$cap(S, T) = \sum_{v_y \in S, v_y \in T \mid (v_x, v_y) \in E} c(v_x, v_y) \quad (3.7)$$

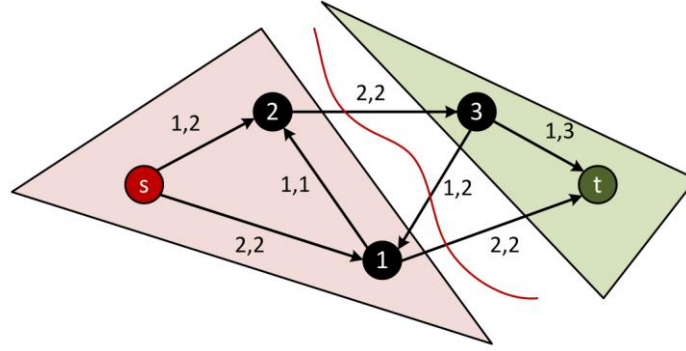


Figure 39: A cut C in the network example of Figure 38. The subset $S = \{s, 1, 2\}$ (red) is related to the source and the subset $T = \{3, t\}$ (green) is related to the sink. The cut-set C_{ST} consists of the set of edges $\{(2,3), (3,1), (1,t)\}$ and a capacity of $cap(S, T) = 2 + 2 = 4$ (© TUM-MIMED, 2013)

Max Flow/Min Cut Theorem

The problem of finding the maximum flow in a network correlates with the problem of finding the cut of minimal capacity among all possible s-t-cuts. According to the theorem of Ford and Fulkerson (Ford and Fulkerson, 1962) the maximum flow value in a network equals the cost of the minimum cut among all possible s-t-cuts. Generally speaking the flow through any network is limited by its bottleneck capacities. Although at some edges higher flow might occur, the maximal total flow is limited by the flow through its bottleneck (Boykov and Veksler, 2006) (Gibbons, 1985):

$$\max F(G) = \min cap(S, T) \quad (3.8)$$

Boykov-Kolmogorov Algorithm

Since Ford and Fulkerson first stated their theorem various algorithms have been developed to solve max-flow min-cut problems. The algorithm published by Boykov and Kolmogorov (Boykov and Kolmogorov, 2004) is currently considered the fastest algorithm for the application of computer vision graph cuts (Schmidt et al., 2009). Their publicly available C++ library (Kolmogorov, 2010) was used to calculate a minimal cut among the set up graph described in section 3.4.6.

The algorithm belongs to the group of algorithms based on augmenting paths and implements two types of search trees, one tree starting from the source and one starting from the sink. Nodes that are not part of either tree are “free” nodes. Within these search trees, inner nodes are considered “passive” while nodes at the border in contact with other nodes are considered “active”. Active nodes are allowed to grow and thereby come in contact with nodes of other trees. In case an active nodes comes in contact with a node of the other tree an augmenting path is found.

The algorithm follows 3 repeating stages:

- Grow: trees from source and sink grow until they come in contact and make an $s \rightarrow t$ path

- Augmentation: the $s \rightarrow t$ path is augmented, while search trees split, such that disconnected nodes remain as orphans
- Adoption: trees from source and sink are restored by assigning each orphan to either tree

When the adoption stage is completed, the algorithm repeats with its grow stage. Termination is reached when the trees from source and sink cannot grow anymore, because no active nodes are left, such that all nodes are either part of the source tree or the sink tree. The corresponding separation of nodes represents the minimum cut $C = (S, T)$.

3.4.6 Graph-Cut Implementation

The objective of the graph construction is to transfer the segmentation problem into a simple, undirected graph $G(V, E)$. Nodes are distributed originating from a user provided seed point. Those nodes sample the grey value (GV) of their respective underlying voxels. The difference in GV between neighboring voxels $\{v_x, v_y\}$ determines the graph's weights $c(v_x, v_y)$. After the graph is set up and all edges are assigned their weights, a minimal cut is calculated which separates all nodes into either a group associated to the object represented by the *source* s or a group associated to the background represented by the *sink* t (see Figure 40).

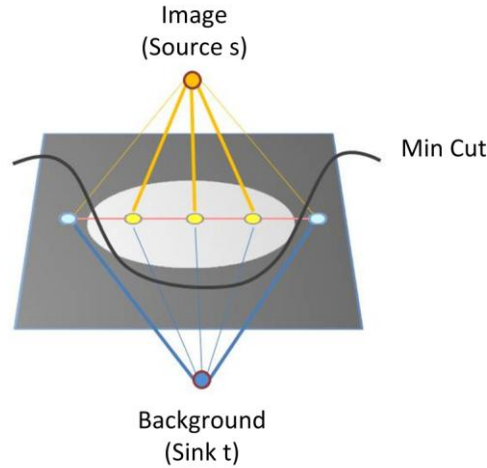


Figure 40: Representation of the segmentation task as a graph network from a *source* s to a *sink* t . The image is separated from the background through a minimal cut (© TUM-MIMED, 2013)

Graph Template

In order to define the graph's shape, diameter and area to spread within, a graph template $T \in \mathcal{R}^3$ is introduced

$$T = \{M_0, \dots, M_n\} : 0 \leq n \leq \infty \quad (3.9)$$

The markers $M_i = (m_x, m_y, m_z)$ of template T are vectors in \mathfrak{R}^3 , where $\forall m_z := \phi$, resulting in a two dimensional template. The markers M_i of template T are denoted by $M_i(T)$. Various predefined shapes can be implemented to serve as a template, e.g. a square-shape, triangle-shape or heart-like-shape (see Figure 41 (2), (3), (4)).

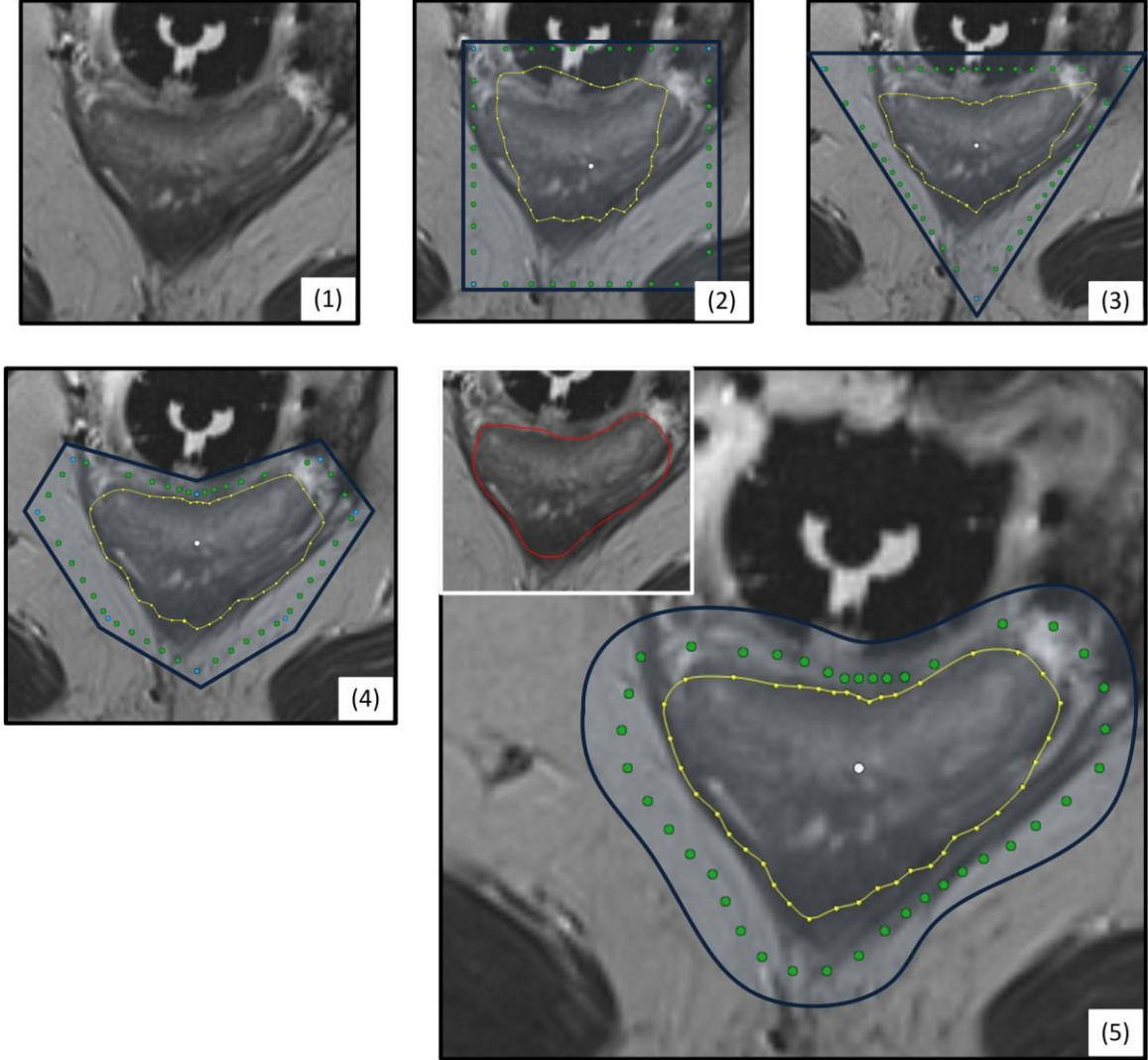


Figure 41: Various graph template shapes, template (green and blue), seed point (white), segmentation result (yellow): Raw image (1), square template (2), triangle template (3), heart shaped template (4), dynamic template: user drawn or previous cut, in this case: user drawn template (red) (5) (© TUM-MIMED, 2013, MRI data from (Egger et al., 2012e))

Although predefined shapes might result in sufficient results in some images slices, they are not capable of robustly handling the altering two dimensional shapes of the rectum/sigmoid colon in succeeding image slices. Moreover, in case the ROI is fully covered with a square template, other objects might be included as well in the square area which can negatively influence the segmentation result. In Figure 41 (2) it can be seen that the cut (yellow line) incorporates parts of the characteristic dark obturator. The proximity of the dark obturator to the rectum/sigmoid colon frequently compromises the segmentation result, as the transition to the dark obturator causes over proportional high graph weights and results in a cut at this location. An approach to spare such objects from the ROI provides a user-defined template

such as Figure 41 (4). It can be predefined or setup by multiple user clicks and circumventing disturbing objects such as the obturator. However, the user effort to setup the template compared to the information gained about the ROI is relatively high. A more advantageous approach provides a user drawn template, where the user outlines the object contour. With this approach not only the exact shape of the object in the respective slice is known and can be employed further, but also exact information about the object's contour grey values and grey value distribution inside the object can be extracted. Such an approach can be seen in Figure 41 (5), where the red outline is a user drawn contour used as template for the graph in (5).

Furthermore, complex templates such as a user drawn template or a template taken from the last cut inherent higher robustness in cuts resulting from them, than other graph template shapes such as squares or triangles. With the same number of nodes V spread from the seed point to the template border and a $\Delta = 0$ (see section 3.4.6), cuts from complex templates yield the exact same shape as the previous shape.

Sorting of Template Markers

In the context of a user provided template for the graph, the user might draw a template in clockwise or counter-clockwise order. To calculate the centroid of polygon, set up the graph and distribute its nodes it is necessary to arrange the provided template in a clockwise order. Therefore, consider a template $T \in \mathbb{R}^3$ consisting of a limited, unordered set of three dimensional markers M_i . To sort the markers M_i of the given template T , consider the markers $M_i \in \mathbb{R}^2 \setminus m_z \in \mathbb{R}$. First, the position of the mass center $MC = \{MC_x, MC_y\}$ of the given template T is calculated in the x - y -plane by

$$MC_x = \frac{1}{n+1} \sum_{i=0}^n m_x \quad (3.10)$$

$$MC_y = \frac{1}{n+1} \sum_{i=0}^n m_y \quad (3.11)$$

Thereafter, the polar angles between each marker M_i and the x -coordinate is calculated referring to the mass center MC :

$$\tan_i = \arctan\left(\frac{m_{y,i} - MC_{y,i}}{m_{x,i} - MC_{x,i}}\right) \quad (3.12)$$

With the information about the angle to the x -plane of each vector M_i , the vectors can be sorted by the following algorithm:

Algorithm 1: Pseudocode of the sorting algorithm

1. *Procedure: Sort(tan, v)*
2. $flag \leftarrow true$
3. $\forall i \in \mathbb{N} : 0 \leq i \leq n \text{ and } flag == true$
4. $flag \leftarrow false$

4. $\forall j \in \mathbb{N} : 0 \leq j \leq n-1$
5. *if* $\tan_{j+1} > \tan_j$
6. $temp_{tan} \leftarrow \tan_j$
7. $temp_{vec} \leftarrow M_j$
8. $\tan_j \leftarrow \tan_{j+1}$
9. $M_j \leftarrow M_{j+1}$
10. $\tan_{j+1} \leftarrow temp_{tan}$
11. $M_{j+1} \leftarrow temp_{vec}$
12. $flag \leftarrow true$

Thereafter, the sets M_t as well as \tan_t are sorted in a clockwise order.

Seed Point Position

At the origin of every graph lies a specific point from where the nodes of the graph are distributed. This point is called the seed point SP of the graph. The seed point can be automatically determined from the provided template T .

The obvious location for the seed point is the center of mass of the given template T calculated by equations (3.10) and (3.11). However, this calculation only yields useful results in some rare situations when all markers $M_t \in T$ are uniformly and symmetrically distributed. Generally, equations (3.10) and (3.11) find the center of mass of a massless polygon with equal mass points at the marker positions. Figure 42 illustrates this effect with three different polygons. Although the spanned area of all three shapes is equal the position of the mass center varies.

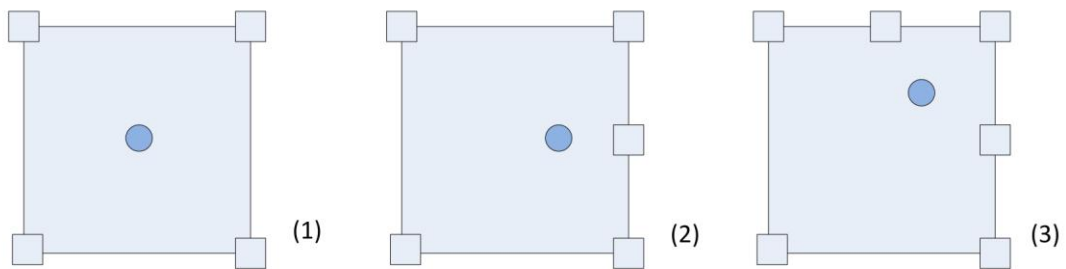


Figure 42: Center of mass of different shapes. The position of the center of mass varies depending on the number of markers, although the spanned area stays equal (© TUM-MIMED, 2013)

Depending on the shape of the user drawn template or respective calculated cut, the markers M_t of template T are non-uniformly distributed and therefore equations (3.10) and (3.11) cannot be employed. Instead, the so called centroid of polygon CP will be calculated and used as seed point position (see Figure 43). The centroid of a polygon defined by n markers M_t yields the center of mass of an area of equal mass distribution spanned by the markers M_t .

For the markers $M_t \in \mathbb{R}^3 : M_t = \{m_x, m_y, m_z\} \wedge 0 \leq x \leq n \wedge 0 \leq y \leq n$, it is calculated by the following equations (Bourke, 2007) (Heckbert, 1994):

$$CP_x = \frac{1}{6A} \sum_{i=0}^{n-1} (m_{x,i} + m_{x,i+1})(m_{x,i}y_{i+1} - m_{x,i+1}y_i) \quad (3.13)$$

$$CP_y = \frac{1}{6A} \sum_{i=0}^{n-1} (m_{y,i} + m_{y,i+1})(m_{x,i}y_{i+1} - m_{x,i+1}y_i) \quad (3.14)$$

$$CP_z = m_z \quad (3.15)$$

Thereby, A is the spanned polygon's area defined by

$$A = \frac{1}{2} \sum_{i=0}^{n-1} (m_{x,i}m_{y,i+1} - m_{x,i+1}m_{y,i}) \quad (3.16)$$

In the process of calculation it is assumed that

$$m_{x,n}, m_{y,n} = m_{x,0}, m_{y,0} \quad (3.17)$$

The seed point $SP = \{sp_x, sp_y, sp_z\}$ of a given template T is defined

$$sp_x := CP_x \quad (3.18)$$

$$sp_y := CP_y \quad (3.19)$$

$$sp_z := CP_z \quad (3.20)$$

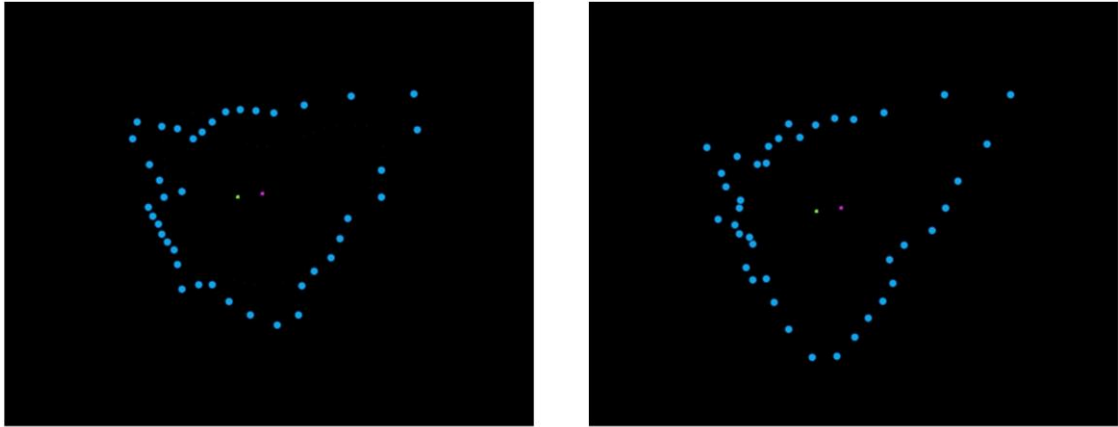


Figure 43: Illustration of the calculated mass center (green) and centroid of polygon (pink) of two different templates (© TUM-MIMED, 2013)

This effect is particularly important regarding the dynamic adaption of the template over consecutive segmentation slices. Depending on the object shape and calculated minimal cut, the template can become more and more rugged over several image slices such that the template marker distribution becomes less uniformly and the difference between the mass

center and centroid increases. This effect impairs an optimal node distribution over the object which causes decreased sampling of the object's grey values.

Scaling of Template

A given template T , either user drawn or the last calculated *cut*, will be scaled by a specific size s in order to be used as template for a next cut. To scale the template about a fixed point, the template first has to be translated so that the fixed point is at the coordinate origin. Then, the scaling is computed and the inverse translation is applied to shift the template back to its original coordinates. The scaling process used is based on homogeneous coordinates (HC) where vector translations can be represented as matrix multiplications instead of vector additions (Godse, 2008). Consider a template T consisting of a set of markers $M_t \in \mathbb{R}^3 \setminus m_z \in \mathbb{R} : M_t = \{v_{x,t}, v_{y,t}\}$. For the fixed point used for scaling the formerly calculated centroid of the template polygon $CP = \{CP_x, CP_y\}$ will be used. The equation for scaling and rotation of a given vector $p = \{x, y\} \in \mathbb{R}^2$ with CP as the fixed point is given by

$$f(p) = \tilde{p} = (-T) R S T p \quad (3.21)$$

Thereby, T is the translation matrix given by

$$T = \begin{bmatrix} 1 & 0 & -CP_x \\ 0 & 1 & -CP_y \\ 0 & 0 & 1 \end{bmatrix} \quad (3.22)$$

which translates p such that CP is at the origin $\{0,0\}$. The matrix S is the scale matrix given by

$$S = \begin{bmatrix} s_x & 0 & 0 \\ 0 & s_y & 0 \\ 0 & 0 & 1 \end{bmatrix} \quad (3.23)$$

where $s = \{s_x, s_y\}$ is are the specific scale factors in the x and y direction. In the course of this work $s_x = s_y$ will be used at all times and denoted by the scale factor sf . The matrix R is the rotation matrix to rotate the template along the x axis with angle α . It is given by

$$R = \begin{bmatrix} \cos(\alpha) & -\sin(\alpha) & 0 \\ \sin(\alpha) & \cos(\alpha) & 0 \\ 0 & 0 & 1 \end{bmatrix} \quad (3.24)$$

However, in the course of this thesis the template will not be rotated and thus $R = E$, where E is the identity matrix.

To scale the template T with a specific scale factor s , all markers M_t of T are scaled by equation (3.21) eventually mapping the original template T to the scaled template \tilde{T}

$$z : T \rightarrow \tilde{T} \quad (3.25)$$

Figure 44 illustrates this procedure for a given template. In this case a *cut* (1) (yellow line) is used as a template T . The markers of T are scaled by a scaling factor s around the centroid of the polygon (2) (white dot) defined by T . The scaled template \tilde{T} is illustrated by the green line (2), which is used as a template for the graph in a next slice (3) (green dots).

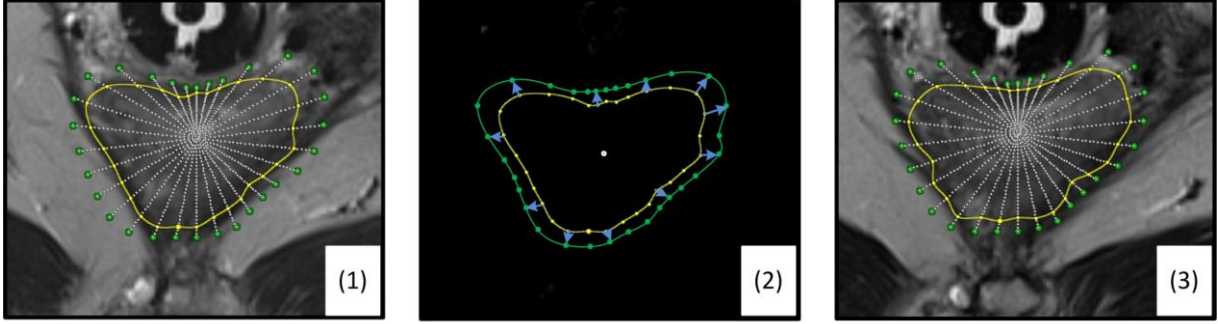


Figure 44: A given template is scaled by a certain scaling factor s with the centroid of the polygon as the fixed point. The cut in (1) (yellow line) is taken as a template and scaled (2) (green line), which is then used as a template for a next cut (3) (green dots) (© TUM-MIMED, 2013, MRI data from (Egger et al., 2012e))

Node Distribution

From a given seed point $SP = \{sp_x, sp_y, sp_z\}$ a number of rays $r_i : 1 \leq i \leq k$ are spread in uniform angles. For each ray r_i the intersection point IP with T is calculated. The length of each ray r_i is defined by the distance between SP and the intersection point IP of T .

$$|r_i| = |IP_{ri} - SP| \quad (3.26)$$

Along all rays r_i a number of nodes $V_{i,n} : 0 \leq n \leq u$ is distributed in equal distances from the seed point to the template border (see Figure 45). The node $V_{i,0}$ indicates the node closest to the seed point, $V_{i,u}$ indicates the last node of ray r_i . Furthermore, each node $V_{i,n}$ coincides with a voxel of the image I . Moreover, the graph network requires the implementation of two distinct virtual nodes that are not represented by a voxel of image I , the source s and the sink t (Boykov and Jolly, 2001).

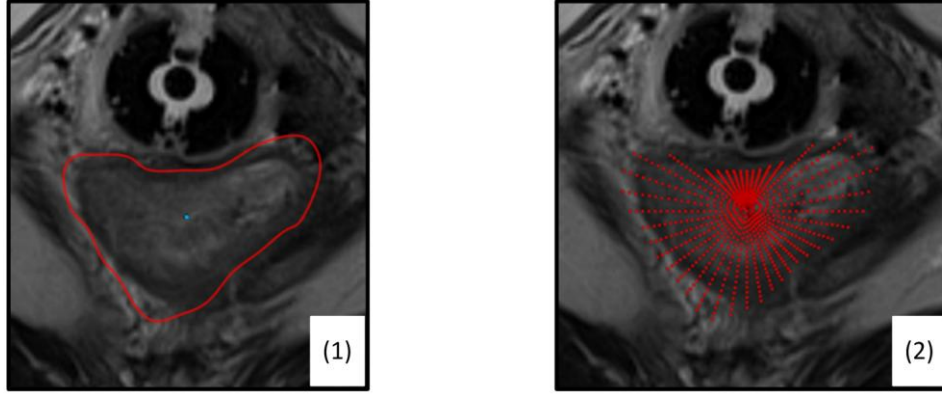


Figure 45: Graph node distribution from a given template and seed point position (© TUM-MIMED, 2013, MRI data from (Egger et al., 2012e))

Due to the equal amount v of nodes spread along each ray r regardless of the length of each ray r , the seed point position is particularly important to accomplish an equal node distribution within the template. It is that the centroid of the template is used instead of the mass center.

Figure 46 illustrates this effect: image (1) on the left shows the difference between the mass center and centroid location for the given polygon and in image (2) on the right the node distribution is based on the mass center which causes a concentration of nodes in the area above the seed point. The centroid position will decrease this effect and cause a more equal node distribution.

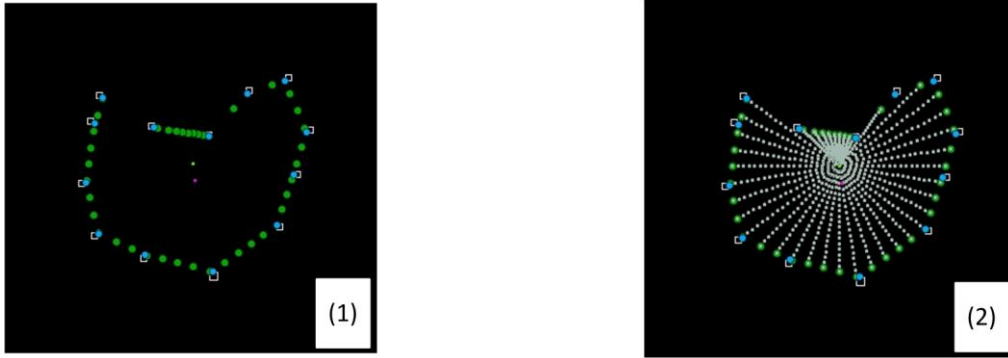


Figure 46: Difference between the mass center (green) and the centroid (pink) (1), and corresponding node distribution based on the mass center (2) (© TUM-MIMED, 2013)

Sampling of Grey Values

Each node $V_i \in V(G)$ is a set of four, comprising $V_i = \{v_{x,i,r}, v_{y,i,r}, v_{z,i,r}, gv_{i,r}\}$ with the node's 3D position and voxel's grey value. To gather information about the object's grey value outlook, the mean grey value in an area a around the seed point SP determined by factor ϕ is calculated according to

$$a \subset gv_i(V_i) : V_i \in V(G) | 0 \leq i \leq k \times \phi \quad (3.27)$$

$$meanGV_{SP} = \frac{1}{k \times \phi} \sum_{i=0}^{k \times \phi} gv_i(a) \quad (3.28)$$

In the same way a $meanGV_C$ of $gv_i(M_C) \in C$ is calculated among all markers M_C of the minimal cut C of a previous slice, to gather information of the grey values among the object contour.

Interactive Seed Point Dragging

The segmentation result strongly depends on the seed point position, as it determines the position of the graph's nodes and thereby the GV samples to calculate the graph's weights and the cut result in the last step.

In case an object contour represented by a sharp dark to bright area is not sampled due to a too little sampling rate, the cut will perform differently and the quality of the segmentation result will decrease. The *star like* distribution of nodes inherits this problem such that areas further away from the seed point are sampled with a smaller sampling rate per area than areas closer to the seed point.

However, by interactively dragging the seed point different voxels of the image are sampled with the graph's nodes and the user intuitively and unwarely increases the sampling rate per area defined by the number of nodes of graph G and the area of template T

$$f_s = \frac{|V(G)|}{area(T)} \quad (3.29)$$

Graph Weights

So far the nodes V of the graph $G(V,E)$ have been implemented. The next step to set up the complete graph network is to implement the graph's edges E . In the following, three different types of edges can be distinguished (see Figure 47):

- Z-weighted edges are inter-edges connecting the seed point SP with the first node $v_{i,0}$ of each ray r_i . They also connect all neighboring nodes $(v_{i,n}, v_{i+1,n})$ of the same ray r_i . They are denoted by the subset $E_z \subset E$
- XY-weighted edges are intra-edges connecting nodes $(v_{i,n}, v_{i+1,m})$ of directly neighboring rays r_i, r_{i+1} . They are denoted by the subset $E_{xy} \subset E$
- T-weighted edges connect each node $v_{i,n} \in V(G)$ with the source s and the sink t . They are denoted by the subset $E_T \subset E$

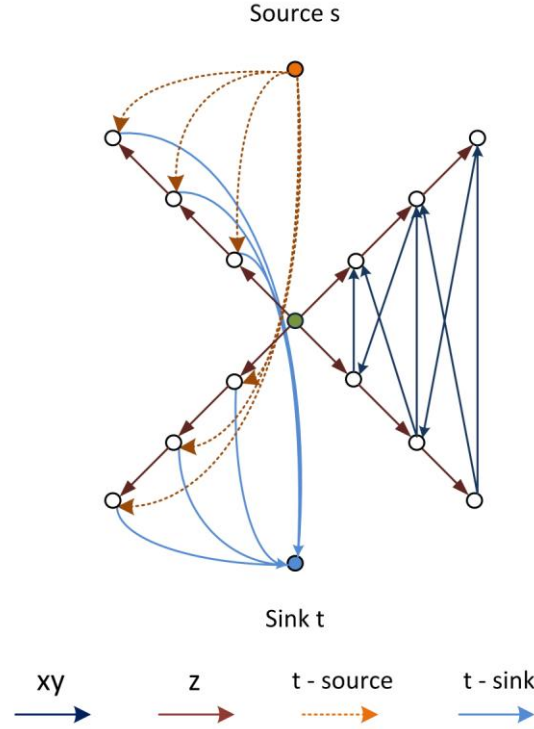


Figure 47: Illustration of three different graph weight types: xy-weights, z-weights and t-weights (© TUM-MIMED, 2013)

Z-Weights

According to (Li et al., 2006) the capacity $c(v_{i,n}, v_{i,n+1})$ for all edges $(v_{i,n}, v_{i,n+1}) \in E_Z$ is set to a maximum value indicated by ∞ .

$$\forall e(v_{i,n}, v_{i,n+1}) \in E_Z : c(v_{i,n}, v_{i,n+1}) = \infty \quad (3.30)$$

Under the assumption that the calculated minimal cut separates the graph $G(V, E)$ by $C = (S, T)$, such that $\{s \in S \wedge t \in T\}$ each ray r has to be cut at least one time. Setting all z-weights to a value of ∞ furthermore guarantees that each ray r is cut only one time which cost $1 \times \infty$ per ray. Cutting the same ray twice or more costs $> n \times \infty$ which will not result in the minimal possible cut set, thus each ray is cut exactly one time.

Because of this paradigm, it is hardly possible to alter the z-weight cost function and assign values different to ∞ . In case it is lowered to an effective value, similar to t-weight values, the possibility of cutting the same ray twice increases, which will not result in an optimal segmentation result.

T-Weights

The allocation methodology of T-Weight capacities to all edges $E_T \in E(G)$ is crucial to the calculated segmentation result. The algorithmic implementation is given as pseudo code in Algorithm 2 and can be separated in four distinct tasks that will be explained in further detail.

Algorithm 2: Pseudo code of the implementation of capacities to all T-Weighted edges $E_T \in E(G)$

```

1.  Procedure: TWeights(G(V, E))
2.   $\forall i \in \mathbb{N} : 0 \leq i \leq k - 1$ 
3.       $c(s, v_{i,0}) \leftarrow \infty$ 
4.       $c(v_{i,0}, t) \leftarrow 0$ 
5.       $c(s, v_{i,u-1}) \leftarrow 0$ 
6.       $c(v_{i,u-1}, t) \leftarrow \infty$ 
7.       $Phi \leftarrow \frac{1}{s}$ 
8.       $nPhi \leftarrow \text{floor}\{u \times Phi - 1\}$ 
9.      if Flag == false
10.          $meanG^* \leftarrow meanGV_{SP}$ 
11.     else
12.          $meanGV^* \leftarrow meanGV_C$ 
13.      $\forall i \in \mathbb{N} : 0 \leq i \leq k - 1$ 
14.          $\forall n \in \mathbb{N} : 0 \leq n \leq u - 1$ 
15.              $Pre \leftarrow \text{abs}(gv(v_{i,n-1}) - meanGV^*)$ 
16.              $Act \leftarrow \text{abs}(gv(v_{i,n}) - meanGV^*)$ 
17.             if  $(n \leq (nPhi - nPhi \times WF_T))$ 
18.                  $c(s, v_{i,n}) \leftarrow \infty$ 
19.                  $c(v_{i,n}, t) \leftarrow 0$ 
20.             if  $(n > (nPhi - nPhi \times WF_T))$  and  $(n \leq (nPhi + nPhi \times WF_T))$ 
21.                 if flag == false
22.                     if  $(Act - Pre) \leq 0$ 
23.                          $c(s, v_{i,n}) \leftarrow \text{abs}(Act - Pre)$ 
24.                          $c(v_{i,n}, t) \leftarrow 0$ 
25.                     else
26.                          $c(s, v_{i,n}) \leftarrow 0$ 
27.                          $c(v_{i,n}, t) \leftarrow \text{abs}(Act - Pre)$ 
28.                 else
29.                     if  $(Pre - Act) \leq 0$ 
30.                          $c(s, v_{i,n}) \leftarrow \text{abs}(Act - Pre)$ 
31.                          $c(v_{i,n}, t) \leftarrow 0$ 
32.                     else

```

```

33.                                      $c(s, v_{i,n}) \leftarrow 0$ 
34.                                      $c(v_{i,n}, t) \leftarrow \text{abs}(\text{Act} - \text{Pre})$ 
35.           else
36.                                      $c(s, v_{i,n}) \leftarrow 0$ 
37.                                      $c(v_{i,n}, t) \leftarrow \infty$ 

```

Under the assumption that the user-defined seed point is centered in the object and the last node v of each ray r is part of the background, lines 2-5 ensure that the first node v of each ray r is bound to the source s by a capacity of ∞ . In contrast, the last node of each ray will be bound to the sink by a capacity of ∞ .

The capacity value assigned to each T-weight is determined by the intensity contrast of the grey value $gv(v_{i,n})$ of the currently regarded node $v_{i,n}$ to the previous node $v_{i,n-1}$ on the same ray. The deviation from a given mean grey value meanGV^* determines if the node is connected to the sink or source and what capacity value will be assigned.

Generally, with the variable $\text{flag} = \text{false}$, a transition from averagely intensity high to intensity low values is expected and the connections and capacity values are set such that nodes of the intensity high area are connected to the source and nodes of the intensity low area are connected to the sink. For comparison see lines 21 – 27. If the $\text{flag} = \text{true}$, a transition from intensity low to high values is expected and the connections and capacity values are set oppositely, see lines 28 – 34. Figure 48 illustrates this effect for the calculated *cut* in the same image slice depending on the *flag* value.

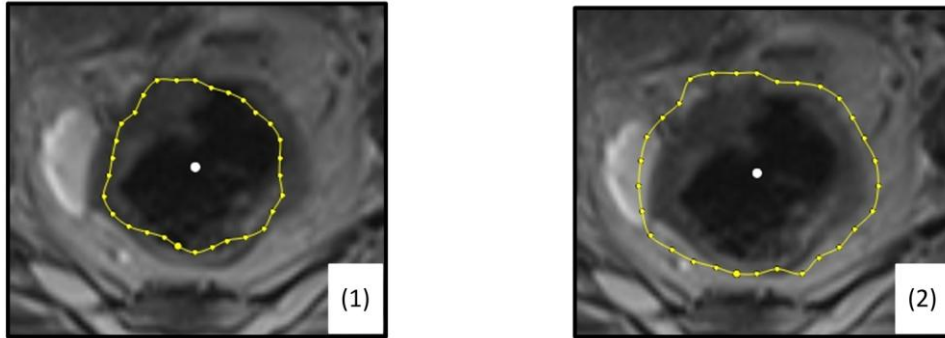


Figure 48: Effect of two types of allocated T-weight capacities. In (1) the transition from intensity low to high areas is preferred, in (2) the transition from high to low intensities is preferred (© TUM-MIMED, 2013, MRI data from (Egger et al., 2012e))

In lines 7 and 8 two variables Φ and $n\Phi$ are introduced. With the knowledge of the scaling factor sf from the previous *cut* to the current template and the number u of nodes v per ray r , the current node v of each ray r representing the shape of the previous *cut* can be determined. The variable Φ represents the inverse scaling factor sf , while $n\Phi$ represents node index in the graph of the current slice that is closest to the node that was part of the *cut* set C in the graph of the template of a previous slice. This allows the implementation of a three zone strategy for the allocation of capacity values among all T-weighted edges. With the assumption that the object shape change from one slice to another is limited, it can be expected that the current *cut* will occur in a similar radius indicated by the node index n .

Thus, a zone I in a range $n \leq (nPhi - nPhi \times WF_T)$, where WF_T is a t-weight parameter defining the zone width is implemented in line 17. With the assumption that all nodes in zone I will be part of the source set S , those nodes are connected with ∞ to the source s and 0 to the sink t . All nodes in zone III, defined by $n > (nPhi + nPhi \times WF_T)$, are assumed to be part of the sink set T and thus connected with ∞ to the sink t and 0 to the source s . In zone II, defined by $(n > (nPhi - nPhi \times WF_T))$ and $(n \leq (nPhi + nPhi \times WF_T))$, the *cut* is expected and weights are allocated according to the previously discussed methodology (see lines 20 – 34).

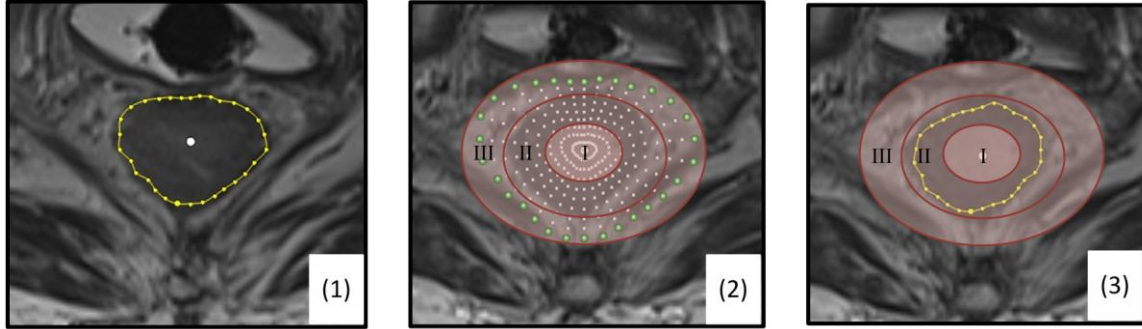


Figure 49: Implemented 3 zone strategy for the allocation of t-weights. (1) Cut of a previous slice used as template, (2) Allocation of t-weights according to their zone (3) Resulting cut in zone II (© TUM-MIMED, 2013, MRI data from (Egger et al., 2012e))

The three zone strategy leads to more robust and stable and less variability in the resulting *cuts*. This is particularly important in the course of dragging the seed point. In slices where the object is very bright in a small area around the seed point, the calculated *cut* might exhibit an effect similar to collapsing and prefer a small areal *cut*. By imposing the cut to occur in zone II, this effect is suppressed which furthermore enhances segmentation quality, robustness and user handling (see Figure 49 and Figure 50).

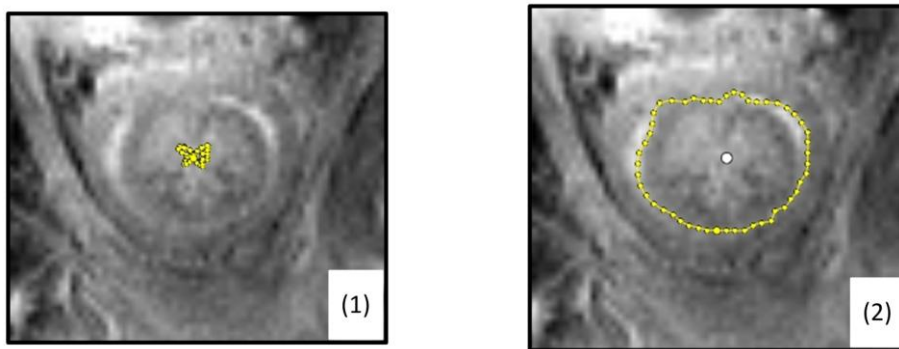


Figure 50. Effect of graph collapsing (1), Segmentation result with implemented three zone strategy, collapsing prevented (2) (© TUM-MIMED, 2013, MRI data from (Egger et al., 2012e))

XY-Weights

The xy-weights $E_{xy} \in E(G)$ can be considered as stiffness parameters and refers to (Li et al., 2006). The implementation, depending on the parameter Δ , realizes different smoothness values for the resulting minimal cut and greater variability among possible *cuts* with the same cost amount.

Their implementation follows

$$\forall e \in E_{xy} : c(v_{i-1,n}, v_{i,n-\Delta}) = \infty \quad (3.31)$$

for the implementation of xy-weights to the previous ray and

$$\forall e \in E_{xy} : c(v_{i+1,n}, v_{i,n-\Delta}) = \infty \quad (3.32)$$

to the next ray. Whereby applies that if $n - \Delta < 0$ take $v_{i,0}$. For $\Delta = 0$, the cut is exactly alike to the template shape. Figure 51 illustrates the effect of $\Delta = 1$ and possible cuts of equal costs.

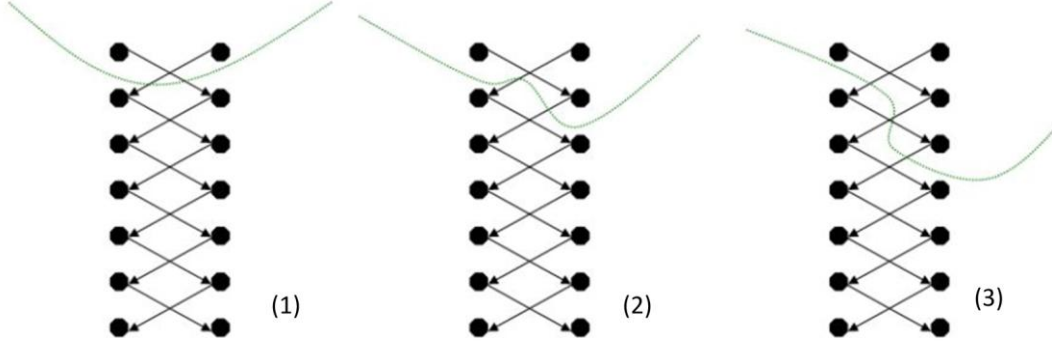


Figure 51: Illustration of the xy-weight implementation, the effect of the parameter Δ and the resulting costs. Exemplary $\Delta = 1$, $c_{xy} = \infty$: (1) $costs = 2 \times \infty$, (2) $costs = 2 \times \infty$, (3) $costs = 4 \times \infty$ (altered from (Egger, 2012))

However, the use of the Δ parameter was limited in the course of thesis, because the higher Δ the more rugged are *cut* contours. With the template for a next slice dynamically adopted from the previous *cut*, the template can become increasingly rugged in the progress of the segmentation, too. However, rugged templates showed to be disadvantageous for the segmentation result, such that the use of parameter Δ was limited to values $\Delta \leq 2$.

Min Cut Labeling

After all nodes $V(G)$ are assigned their weights $c(v_x, v_y)$ (see Figure 52), the Boykov library labels all nodes either corresponding to the *source* s or the *sink* t . The nodes $v \in C(S, T)$ of the min cut are determined such that the last node labeled *source* is included in C as node c_x and the first node labeled *sink* is excluded:

Algorithm 3: Pseudo code MinCut labeling


```

1.  Procedure: LabelMinCut( $G(V, E)$ )
2.   $x \leftarrow 0$ 
3.   $\forall i \in \mathbb{N} : 0 \leq i \leq k-1$ 
4.   $\forall k \in \mathbb{N} : 0 \leq n \leq n-2$ 
5.      if  $v_{i,n} == source$ 
6.          if  $v_{i,n+1} == sink$ 
7.               $c_x \leftarrow v_{i,n}$ 
8.               $x++$ 

```

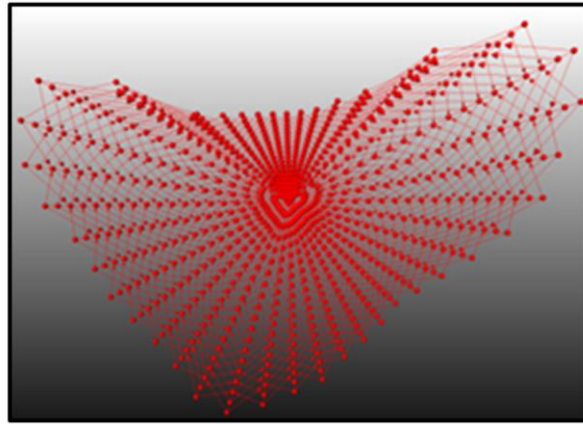


Figure 52: Illustration of a completely connected and weight assigned graph network (© TUM-MIMED, 2013)

Object Processing

The calculated *cut* of a specific slice is stored as segmentation result together with all previous *cuts* of this object. After the complete object is segmented, slices that have been skipped by the user have to be interpolated in order to generate a object contour in each image slice. This step is done with the MeVisLab *CsoSliceInterpolator* module and illustrated in Figure 53.

Thereafter, the set of object contours is used for voxelization of the object and to generate a 3D Object with the *CsoConvertToImage* module. The set of object contours is stored as *cso* file, while the voxelized 3D object is stored as *nrrd* file for further use in treatment planning.

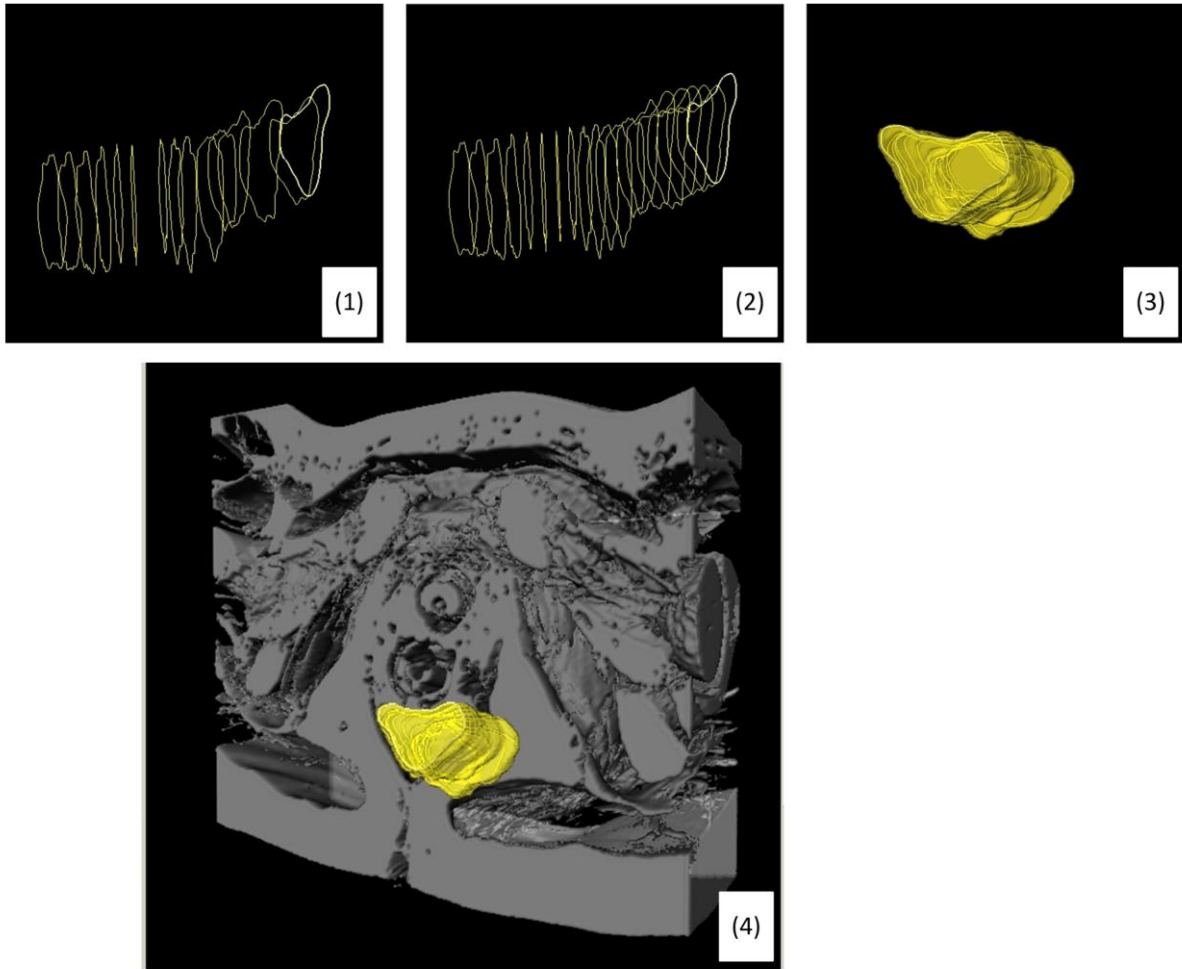


Figure 53: Set of object contours: (1) slices skipped, (2) skipped slices interpolated, (3) voxelized object, (4) voxelized object (yellow) superimposed in the patient anatomy (© TUM-MIMED, 2013)

3.5 Distinguishing Characteristics

The presented segmentation methodology distinguishes itself from the systems introduced in section 2.2 and 2.3 in the following characteristics.

1. *Direct control over the segmentation result:* Compared to fully automatic systems or systems based on user input scribbles with no further possible user influence on the segmentation result, the presented systems offers dexterous direct control over the segmentation result in each slice. Three different methodologies have been implemented to enhance the segmentation result.
2. *Few, intuitive user input parameters:* In contrast to other systems, the presented methodology merely requires the user drawn contour as user input and intuitive interactions for segmentation improvement. No complex parameters such as the estimated object volume which demand initial training or experience are required.
3. *Robust and stable segmentation result:* The mathematical principle of graph theory and minimal capacity cuts leads to a guaranteed global maximum. Furthermore, due to

the dynamic template-based graph construction, not only leaking is prevented but also the segmentation result is robust to object shape changes and contrast variations.

4 Evaluation

4.1 Approach

The presented segmentation methodology and the underlying algorithm was subject to an experiment comparing the computer assisted segmentation result to manually outlined segmentation results. The assed data comprises MR imaging data of the lower female pelvis acquired in the course of image guided gynecological brachytherapy.

Objective

The objective of this experiment is to evaluate the benefit regarding quality and time-saving that can be achieved by utilizing the presented methodology in contrast to the clinical gold standard of manual segmentation.

Materials

Computation was performed on a personal computer with Windows 7 Home Premium 64 Bit operating system and installed Service Pack 1. The processor was an Intel® Core™ i3 CPU M330 with 2.13 GHz dual core. Internal memory comprises 4.00 GB, with 3.68 GB available.

The utilized MeVisLab® version is 2.3.1 with Qt version 4.8.0. All C++ implementations were conducted and compiled with Microsoft® Visual Studio 2008, Version 9.

Table 2: Data sets and their respective performed MR sequence					
Data Set	Magnet Resonance Sequence	Matrix (voxel x voxel)	Resolution (mm x mm)	Slices	Slice thickness (mm)
1	Axial T2 weighted TSE (Turbo Spin Echo) 320	320 x 320	0.625 x 0.625	26	3.0
2	Axial T2 weighted TSE 320	320 x 320	0.625 x 0.625	30	3.0
3	Axial T2 weighted TSE 320	320 x 320	0.625 x 0.625	50	3.0
4	TrueFisp (fast imaging with steady state precession)	384 x 384	0.781 x 0.781	72	3.0
5	TrueFisp	320 x 256	0.875 x 0.875	28	3.0
6	Axial T2 weighted TSE 320	320 x 256	0.875 x 0.875	22	3.0
7	Axial T2 weighted TSE 320	320 x 256	0.875 x 0.875	40	3.0

To calculate the max flow/min cut the publicly available C++ library developed by Boykov and Kolmogorov (Boykov and Kolmogorov, 2004) (Kolmogorov, 2010) was utilized.

The data used for this experiment is a set of 7 MRI datasets acquired during gynecological interstitial brachytherapy cases performed at the AMIGO suite of the Brigham & Women's Hospital with a Siemens 3 Tesla Verio MR scanner. The complete data is available for download from (Egger et al., 2012e) and described in detail in (Kapur et al., 2012). The respective MR sequence of each data set can be seen in Table 1.

For comparison of the algorithmic computed segmentation result, a medical doctor experienced in radiological segmentations of gynecological brachytherapy at the SPL, for comparison see Egger et al. (2012a), manually outlined the rectum/sigmoid and bladder. For the rectum/sigmoid, the manual segmentation was performed two times with a time difference of several months. For the bladder only one set of manual segmentations was available.

Parameters

The evaluation was performed with a constant t-weight parameter $WT_F = 0.2$. The scaling factor sf and the number of rays r and points per ray n were $sf \in [1.6]$, $r \in \{40\}$ for the rectum and $r \in \{50\}$ for the bladder, $n \in \{40\}$ for the rectum and $n \in \{50\}$ for the bladder.

In order to estimate the complexity of the segmentation task, the respective number of slices where segmentation was performed as well as the object's volume (cm^3) and number of voxels was investigated. Furthermore, the time in seconds for the segmentation of each data set was acquired by screen capture recordings.

Evaluation Methods

The evaluation of the presented segmentation algorithm was performed with the Dice Similarity Coefficient (DSC) and the Hausdorff distance (HD). Moreover, the median and standard deviation of the DSC and Hausdorff distance were calculated.

Dice Similarity Coefficient:

The DSC is a common measurement procedure in image segmentation (Crum et al., 2006) (Zou et al., 2004). It measures the spatial overlap between two segmentation results noted by sets A , B and is defined as

$$DSC(A, B) = 2 \times V(A \cap B) / (V(A) + V(B)) \quad (4.33)$$

where $A \cap B$ is the intersection area of sets A and B and $V(\cdot)$ is the volume in mm^3 . Exemplary scenarios of three different DSC calculations are illustrated in Figure 54.

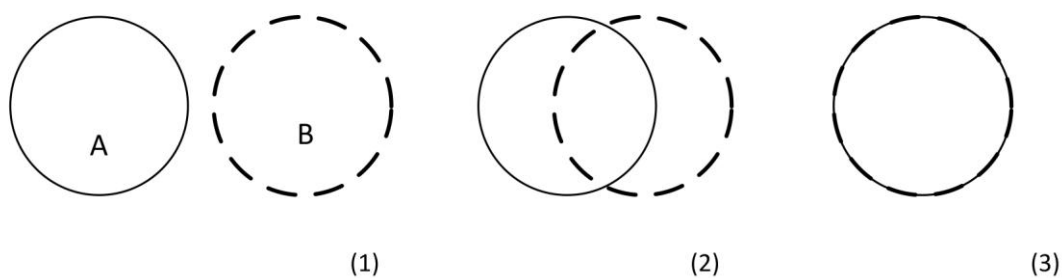


Figure 54: Illustration of three different segmentation scenarios and their respective DSC : (1) $DSC(A,B) = 0\%$, (2) $DSC(A,B) = 2 \times V(A \cap B) / (V(A) + V(B))$, (3) $DSC = 100\%$ (© TUM-MIMED, 2013)

The calculation was performed by a MeVisLab® network depicted in Figure 55 utilizing *Algorithm* modules.

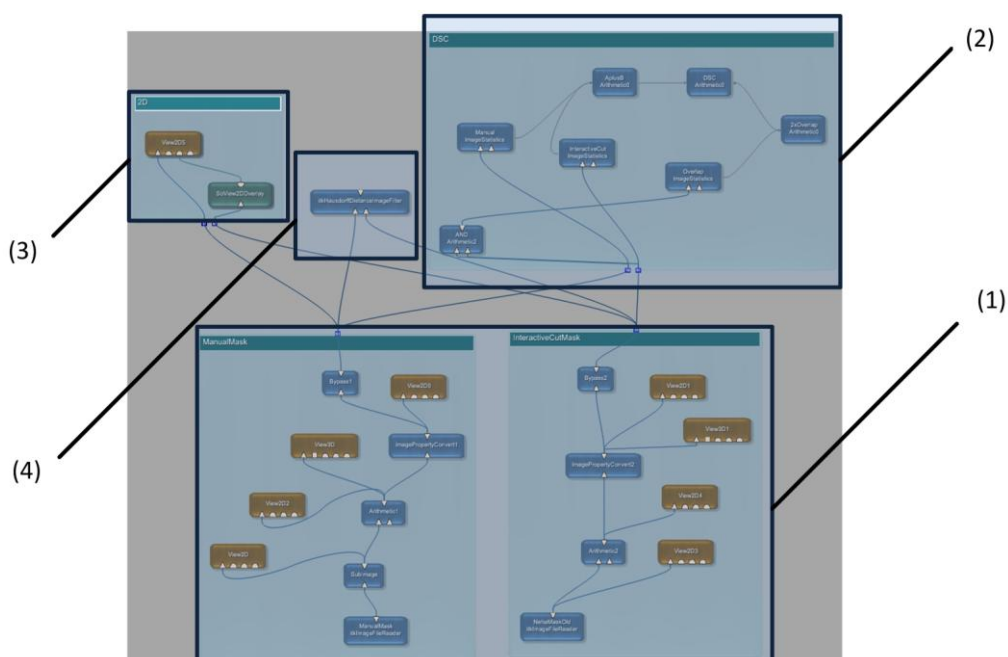


Figure 55: MeVisLab® network for the computation of the DSC and Hausdorff distance: (1) image loading and preprocessing, (2) DSC calculation, (3) visualization, (4) Hausdorff distance calculation (© TUM-MIMED, 2013)

The image loading and preprocessing of the calculated result and manual segmentation result of Figure 55 (1) can be seen in detail in Figure 56. Both data sets are imported as *nrrd* data file types.

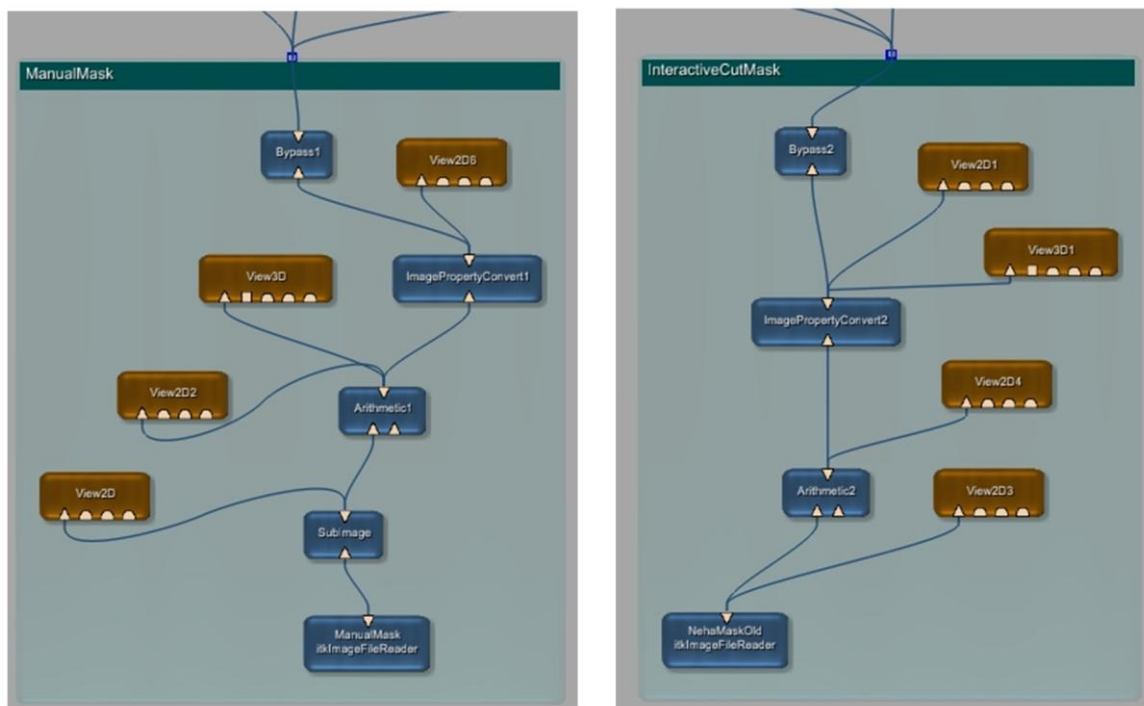


Figure 56: Image loading and preprocessing of the calculated and manual segmentation result for the calculation of the DSC and HD (© TUM-MIMED, 2013)

The calculation of the DSC (Figure 55 (2)) is performed utilizing predefined *Algorithm* modules and is depicted in detail in Figure 57.

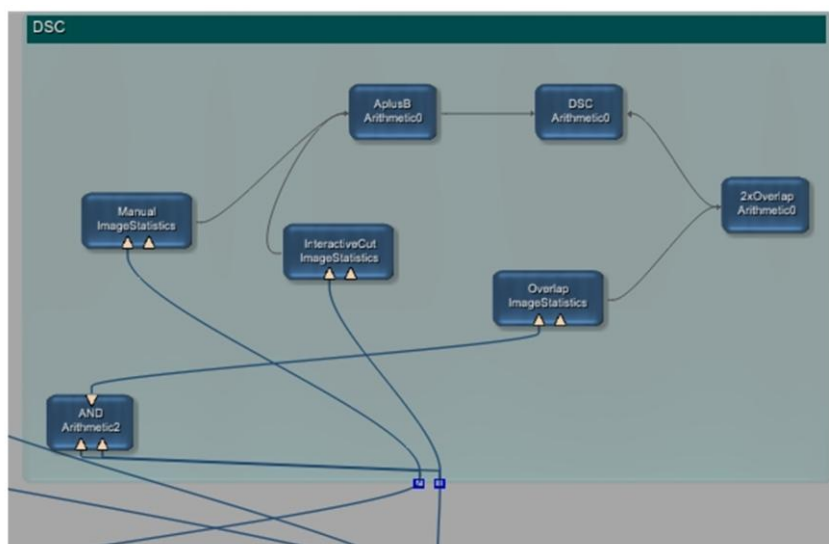


Figure 57: Calculation of the DSC by predefined *Algorithm* modules (© TUM-MIMED, 2013)

Hausdorff Distance: The Hausdorff distance measures the distance between two subsets of the metric space. It defines the maximum distance among all minimal distances between two sets (Jesorsky et al., 2001).

$$H(A, B) = \max(h(A, B), h(B, A)) \quad (4.34)$$

$$h(A, B) = \max_{a \in A} \min_{b \in B} \|a - b\| \quad (4.35)$$

Since the HD is non-symmetric, often $h(A, B) \neq h(B, A)$ applies (see Figure 57).

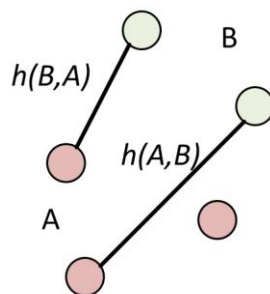


Figure 58: Illustration of the Hausdorff distance for two sets A and B where $h(A, B) \neq h(B, A)$ (© TUM-MIMED, 2013)

The calculation of the Hausdorff distance (Figure 55 (4)) was performed using the MeVisLab® module *itkHausdorffDistanceImageFilter* shown in Figure 598 which returns the HD in *voxels*.



Figure 59: MeVisLab® module used for calculation of the Hausdorff distance (© TUM-MIMED, 2013)

4.2 Experiments

In each data set one segmentation utilizing the presented interactive segmentation methodology was conducted for the rectum/sigmoid and bladder.

For documentation and time measurement purposes each segmentation performance was visually recorded by the screen capture tool Microsoft® Expression®. From the acquired videos the segmentation time needed was gained starting at the beginning of the user drawn contour until the end of the segmentation of the final slice (see Figure 58).

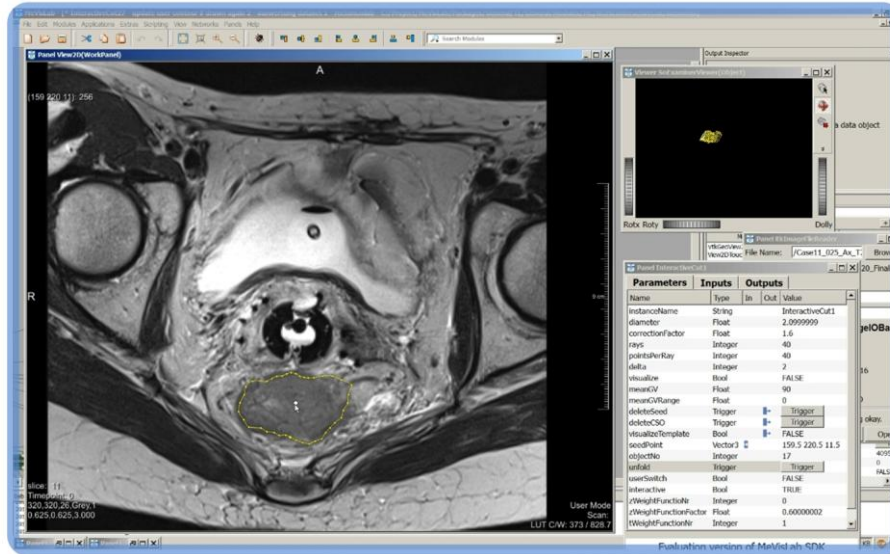


Figure 60: Experimental evaluation of the InteractiveCut methodology with MeVisLab® (© TUM-MIMED, 2013, MRI data from (Egger et al., 2012e))

Manual segmentations of the rectum/sigmoid and bladder have been performed in August 2012. The second segmentation data set of the rectum/sigmoid has been performed in April 2013 by the same physician.

In the organ segmentation process, a segmentation was performed in each slice, such that a seed point and contour was calculated in each slice and the sum of segmented slices is in accordance to the manual segmentations. Therefore, no slices were skipped and no interpolation of slices has been performed.

In order to evaluate the basic performance of the presented segmentation algorithm, no methods of improvement such as contour point dragging or reinitialization have been applied. Merely dragging of the seed point was utilized to find an optimal segmentation contour.

Evaluation was performed such that before computer assisted segmentation the outlook of the respective manual segmentation was roughly studied. Otherwise it is challenging for non medical specialists to recognize the object outline and decide an optimal segmentation result.

Regarding the rectum/sigmoid colon, data sets 1, 2, 3, 4, 5, 6, 7 of the manual segmentation version 2 were used as reference. For the evaluation of the bladder, since only one version of manual segmentations was available, this manual segmentation version 1 was used as reference for all data sets 1 – 7.

The interactive algorithm could be performed smoothly without any delay or interruptions on the utilized personal computer.

In the following the segmentation results for the rectum/sigmoid and the bladder are discussed in detail.

4.2.1 Rectum/Sigmoid Colon

The results in Table 3 show the volumetric and time data for the manual expert segmentations of the rectum/sigmoid colon. According to the performing physician, in average the segmentation per data set took 300 sec (5 min) to perform.

Table 3: Manual rectum/sigmoid colon segmentation 1 & 2. M1 indicates the first manual data set, M2 indicates the second manual data set			
Data set	volume (mm ³)		slices
	M1	M2	M1 M2
1	53227	47223	25
2	38809	31635	25
3	24802	18287	18
4	37186	28205	26
5	n.a.	37110	27
6	41787	39164	22
7	99957	100194	40
median	40298	37110	25

In comparison to the manual expert segmentation, the InteractiveCut algorithm segmented a smaller volume in all cases except case 7, where a slightly larger volume was segmented. Furthermore, the InteractiveCut algorithm achieved an median segmentation time per data set of 128 seconds compared to the manual segmentation, which represents a ~60% time saving (see Table 4).

The segmentation results of the InteractiveCut for the data sets 1, 2, 3, 4, 5, 6, 7 have been compared to the expert manual segmentation results M2. The InteractiveCut algorithm achieved an average DSC of $83.85 \pm 4.08\%$ when compared to M2 (see Table 5).

The two manual expert segmentation versions M1 and M2 have been compared in an intra analysis and a DSC has been calculated in order to precisely asses the DSC value of the InteractiveCut result. The intra analysis between manual segmentation data set M1 and M2 yielded a DSC of $83.97 \pm 8.08\%$. This value reflects the difficulty inherent in the segmentation of the rectum/sigmoid colon. As mentioned in section 1, the difficulty of the segmentation of the rectum/sigmoid colon due to its inhomogeneity was also previously discussed by (Haas et al., 2008) (Huyskens et al., 2008) (Egger et al., 2012a). Furthermore, the time period between M1 and M2 exceeded 6 months, whereas for the InteractiveCut segmentation the respective manual segmentation was roughly studied for orientation due to lack of medical experience directly before the segmentation performance.

Table 4: Interactive Cut rectum/sigmoid colon segmentation

Data set	volume (mm³)	time (sec)	slices
1	51734	141	25
2	27945	128	25
3	18915	113	18
4	21207	117	26
5	32473	158	27
6	38073	104	22
7	103171	228	40
median	32473	128	25

Regarding the Hausdorff distance, the InteractiveCut achieved an average value of 11.05 ± 6.81 mm voxel, compared to the average Hausdorff distance of 11.76 ± 7.54 mm voxel between M1 and M2.

Table 5: Comparison of the InteractiveCut results to expert manual segmentation results. IC indicates the InteractiveCut result, M2 the respective manual expert data set, n.a. indicates non availability of the respective data set

	DSC (%)		Hausdorff dist. (voxel)	
Data set	IC – M2	M1 – M2	IC – M2	M1 – M2
1	88.43	86.93	11.04	4.03
2	80.88	85.16	6.48	11.45
3	79.04	78.19	25.47	18.92
4	80.17	70.37	11.05	22.29
5	84.78	n.a.	9.34	n.a.
6	89.54	91.05	4.36	9.78.
7	84.14	91.40	9.64	4.12
$\mu \pm \sigma$	83.85\pm4.08	83.97\pm8.08	11.05\pm6.81	11.76\pm7.54
min	79.04	70.37	4.36	4.03
max	89.54	91.40	25.47	22.29

Figure 61 shows exemplary segmentation results taken from data set 1 and 3. The red area represents the segmentation result of the InteractiveCut, whereas the green area represents the manual expert result. The image (5) depicts the voxelized segmentation result of the manual segmentation, image (6) depicts the InteractiveCut result.

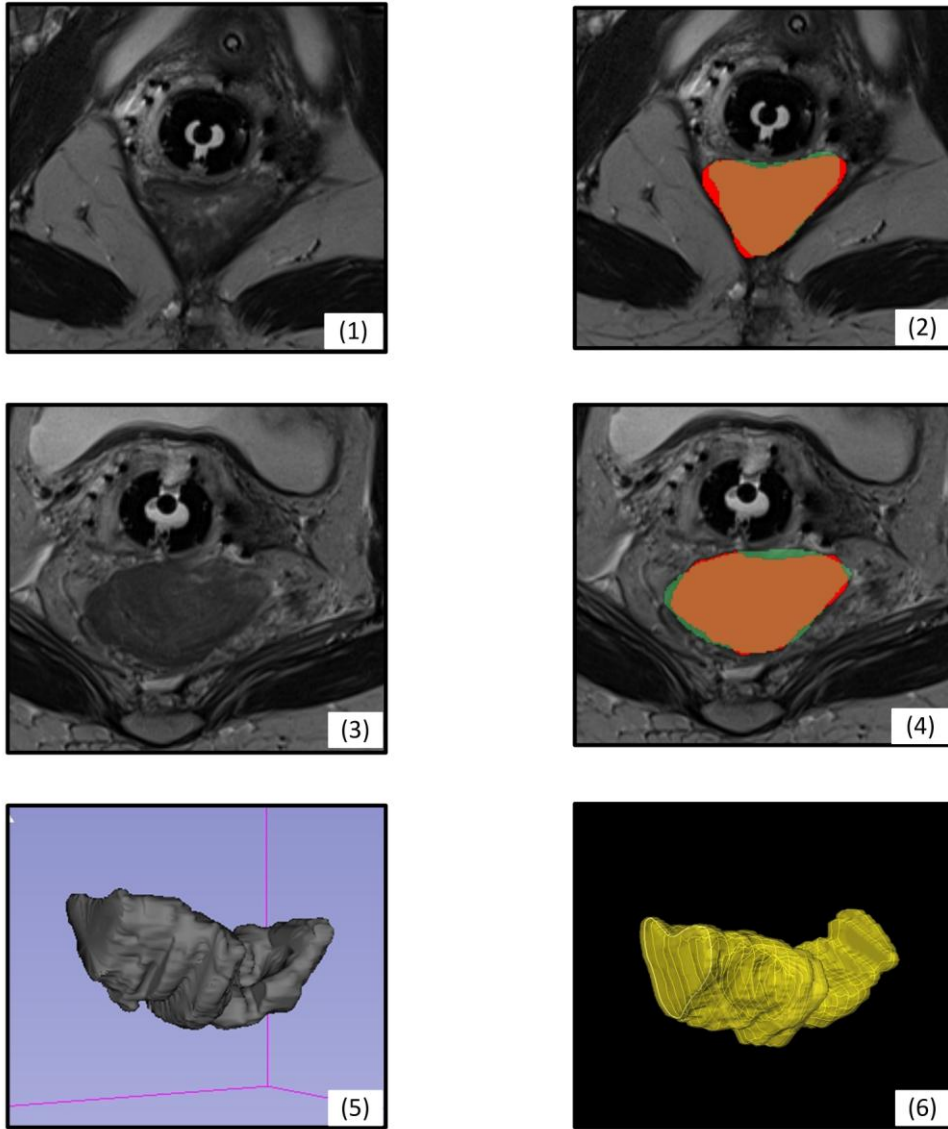


Figure 61: Segmentation results of the rectum/sigmoid colon. For (2) and (4) the red area indicates the InteractiveCut result, the green area the expert manual segmentation result. (5) voxelized manual segmentation, (6) voxelized InteractiveCut segmentation (© TUM-MIMED, 2013, MRI data from (Egger et al., 2012e))

Challenges for the algorithm occurred where the rectum/sigmoid colon shape changed from rotation symmetric to strongly concave as depicted in Figure 62. Thereby, the algorithm is challenged to adopt the graph template to strong shape change within one slice difference. Furthermore, the seed point rooted star-like node distribution corrupts an optimal sampling rate in terms of area within concave object shapes.

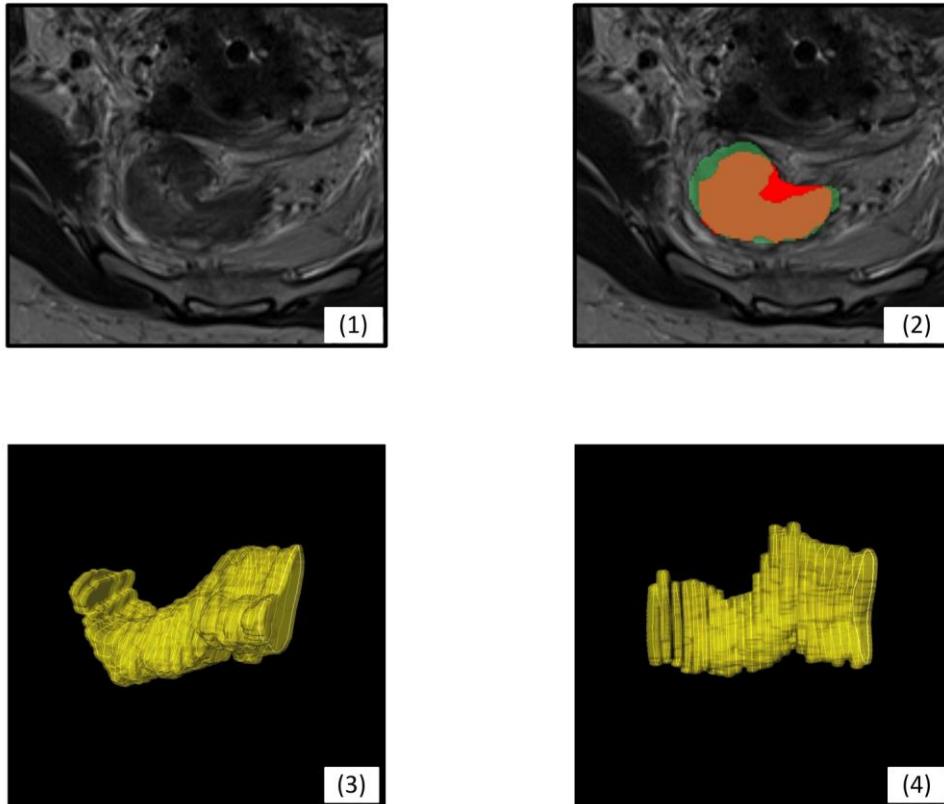


Figure 62: A concave shape can challenge the algorithm due to its seed point rooted star-like node distribution. (2) manual segmentation (green), InteractiveCut segmentation (red), (3) and (4) illustrate strong bending of the object length axis where strong object shape changes can occur (© TUM-MIMED, 2013, MRI data from (Egger et al., 2012e))

4.2.2 Bladder

In accordance to the rectum/sigmoid colon, the bladder as an organ-at-risk was also subject to the evaluation of the InteractiveCut methodology. For the bladder, however, only one set of manual expert segmentation data sets were available, such that an intra-analysis between two manual segmentations was not performed.

In Table 6 the data of the manual expert segmentation is confronted with the results of the InteractiveCut segmentation. In average, it took about 300 seconds (5 min) for the physician to segment each data set. Compared to the rectum, the bladder is larger in volume, however, it is filled with contrast medium such that segmentation is supported. With the utilization of the InteractiveCut methodology the time per data set reduced to a median of 62 seconds in average, which represents a time-saving relation of $\sim 1/5$ (see table 6).

Table 6: Comparison bladder manual/InteractiveCut segmentation, M refers to the manual segmentation results, IA to the InteractiveCut segmentation result. For data set 5 no manual segmentation was available				
Data set	volume (mm³)		time (sec)	slices
	M	IA	IA	M/IA
1	89356	101193	52	10
2	71456	64196	59	15
3	170913	144605	115	20
4	147200	148387	111	17
6	113160	175543	64	22
7	52247	61795	50	13
median	101258	122899	62	16

The spatial comparison between the manual and the InteractiveCut segmentation revealed an average DSC of 81.47 ± 4.48 , which correlates with the achieved value of 83.85 ± 4.08 for the rectum/sigmoid colon (see Table 4 and Table 6).

The average Hausdorff distance for the evaluation of the bladder yielded a value of 13.25 ± 2.10 , which again, is in accordance to the results achieved for the rectum/sigmoid colon with a HD of 11.05 ± 6.81 for the manual/interactiveCut comparison and 11.76 ± 7.54 for the intra-manual comparison.

Table 7: Comparison bladder manual/interactiveCut segmentation		
	DSC (%)	Hausdorff (voxel)
Data set	M – A	M – A
1	79.36	13.60
2	77.42	13.89
3	83.50	14.17
4	85.45	14.38
6	76.08	14.46
7	86.98	9.01
$\mu \pm \sigma$	81.47\pm4.48	13.25\pm2.10
min	76.08	9.01
max	86.98	14.46

Figure 63 shows two exemplary results for the segmentation of the bladder. Due to the user drawn contour in a previous slice and its dynamic adaption, the InteractiveCut methodology achieves to segment the bladder in its complete outline, including both the high value contrast medium filled area and its air filled dark value area. With the three zone strategy, the high contrast edge between the contrast filled area and air filled area is spared from evaluation, as lying in zone I. Instead, the *cut* is performed in zone II, finding both the transition from the high value contrast medium filled area to the background and the transition from the low value contrast air filled area to the background.

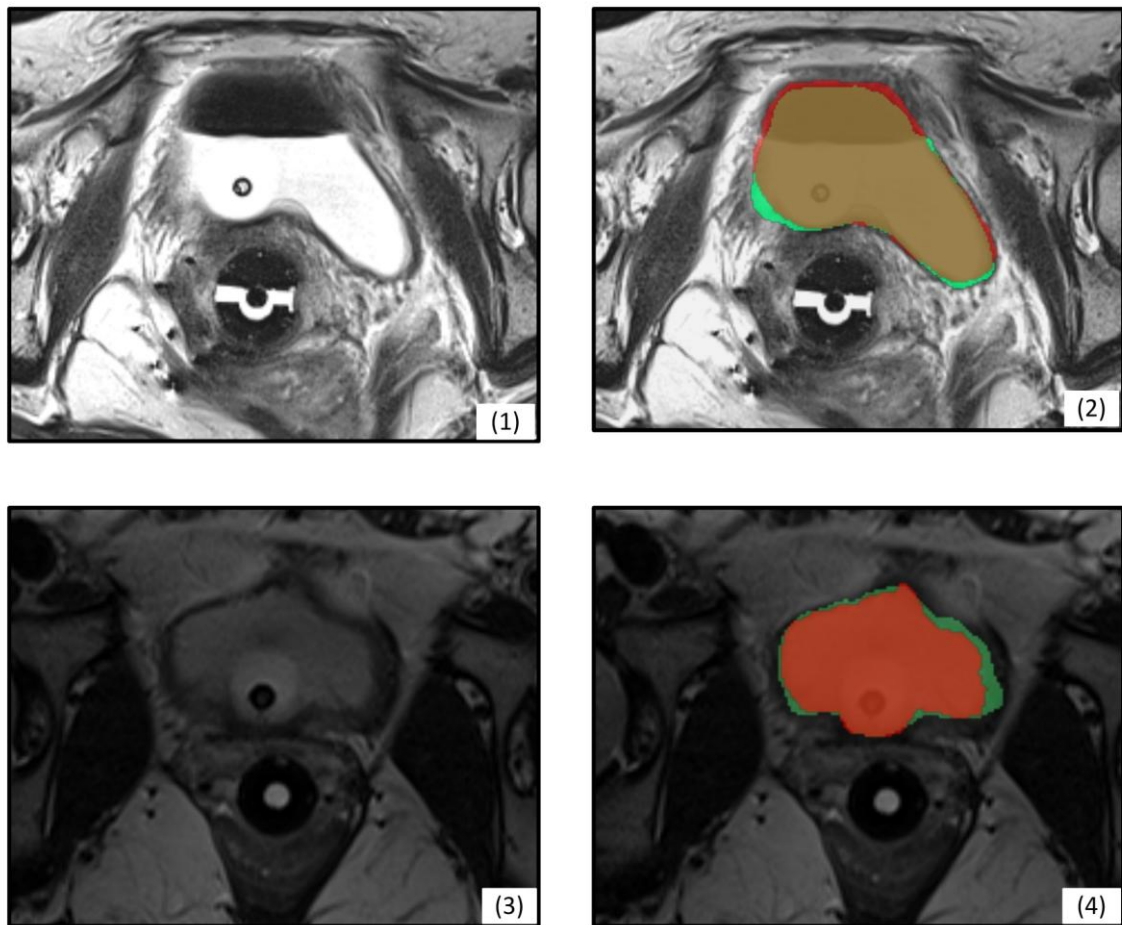


Figure 63: Comparison of segmentation result performed manually (green) and with the InteractiveCut methodology (red). For (2), the dark, air filled area as well as the bright, contrast medium filled area is included in the segmentation (© TUM-MIMED, 2013, MRI data from (Egger et al., 2012e))

In accordance with the results of the rectum/sigmoid colon, the algorithm was particularly challenged where the object shape was strongly convex or concave (see Figure 62).

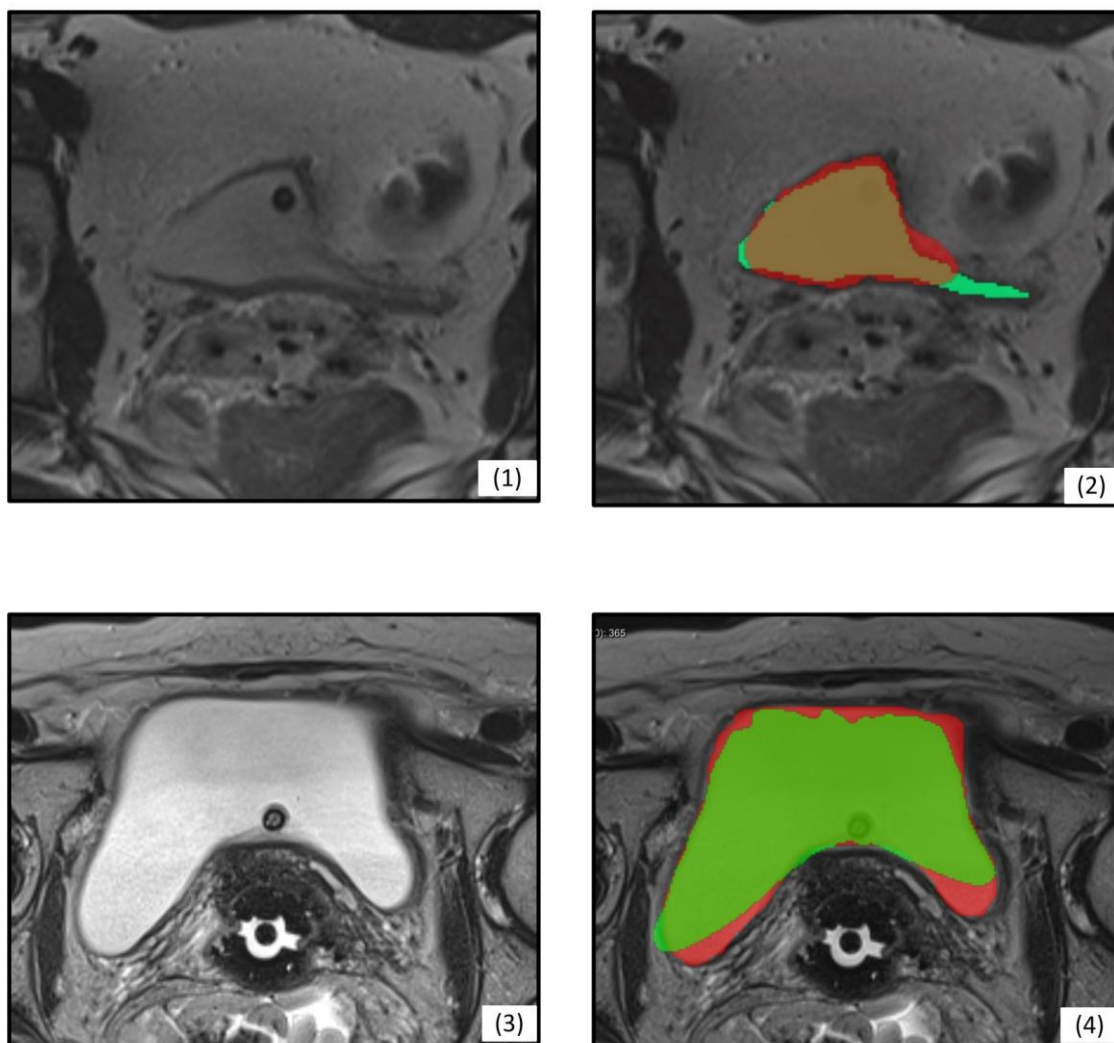


Figure 64: Due to the star like node distribution, segmentation challenges for the InteractiveCut algorithm occur where the object shape is strongly convex or concave (© TUM-MIMED, 2013, MRI data from (Egger et al., 2012e))

4.3 Discussion

The evaluation of the presented segmentation methodology showed a DSC value of 83.85 ± 4.08 and a Hausdorff distance of 11.05 ± 6.81 for the rectum/sigmoid colon compared to manual expert segmentation. An intra-analysis between two manual expert segmentations for all data sets revealed an average DSC value of 83.97 ± 8.08 and a HD of 11.76 ± 7.54 mm.

In accordance with the rectum/sigmoid colon results, a comparison between algorithmic and manual expert segmentations for the bladder yielded an average DSC value of 81.47 ± 4.48 and a HD of 13.25 ± 2.10 mm, which is slightly lower than the rectum/sigmoid colon result. It has to be mentioned that the initial administration of contrast medium to the bladder and thus homogeneous high contrast appearance supports the use of fully automatic region growing algorithms, which could achieve DSC values of 90% (Egger et al., 2012a, Huyskens et al., 2008).

The DSC value of 83.85 ± 4.08 (rectum) and 81.47 ± 4.48 (bladder) achieved with the algorithm presented in this thesis is thus in accordance with the common DSC values in the medical imaging domain regarded as successful as mentioned above. In consideration of the publication of Huyskens et al. (2008) which evaluated the Varian Inc. Smart Segmentation Tool® and where the segmentation result of the rectum was classified “not acceptable to acceptable” and yielded a DSC of 52% and “good to excellent” with a DSC of 90% for the bladder, the DSC value of 83% (rectum) and 81% (bladder) achieved in this thesis is considerably good for the rectum while lower for the bladder.

The intra analysis of Huyskens et al. (2008) between two manual segmentations of different physicians revealed a DSC of 76% for the rectum, compared to 83% in this thesis. These values substantiate the particular difficulty of rectum segmentation mentioned by Huyskens et al. (2008) not only for computer algorithms but also for clinicians.

Regarding the Hausdorff distance Martinez et al. (2012) achieved 7.52 ± 2.3 mm for the rectum and 19.09 ± 3.1 mm for the bladder. The HD achieved in this thesis are 11.05 ± 6.81 mm (rectum) and 13.25 ± 2.10 mm (bladder), where one main reason for these values lies within the star-like node distribution originating in the central seed point and impairs equal sampling where the object outline is strongly convex or concave as described in section 4.2.1 and 4.2.2.

Although the presented DSC (~80-90%) and HD (~7-20 mm) values might seem low, they represent current state-of-the-art research results in the medical domain in general and results achieved with commercially available and research tools for the rectum/sigmoid colon are even lower (52%). Beyond that, as shown by intra analysis DSC values achieved among clinicians, human segmentations as used in clinical daily routine reveal results in the same range of 80% -90%. Depending on the anatomical structure values are slightly higher, e.g. brain, or slightly lower, e.g. rectum/sigmoid colon for intra analysis. Furthermore, it has to be noted, that for pelvic radiotherapy procedures as compared to others, e.g. brain tumors, accurate local segmentation is less concerned by clinicians for soft organ radiotherapy and their OARs, e.g. rectum/sigmoid colon and bladder. Since these organs are prone to change their organ shape in the period from segmentation to treatment start due to air pockets, digestive activities, changes in patient position and weight loss in long term, segmentation results are always error prone and less dependable. To take these alterations into account, the segmented Gross Tumor Volume is always enhanced to the Clinical Target Volume and Planning Target Volume in the process of Treatment Planning, for comparison see section 2.1.3 (Bille and Schlegel, 2002, Kauffmann et al., 2006).

The time needed to segment one data set yielded 128 seconds for the rectum/sigmoid colon and 62 seconds for the bladder utilizing the presented methodology compared to average 300 seconds for manual segmentation, which represents a time saving relation of ~60% and ~80%, respectively. In comparison the work of Haas et al. (2008), regarding the Varian Inc. Smart Segmentation® tool, the time needed to segment the bladder can be considered equal for the algorithm of this thesis and the Smart Segmentation® tool. The later needed 53 seconds in average for the fully automatic segmentation and the result was classified “excellent to good”, which includes “manual modification in a limited nr. of slices”, compared to 75 seconds for the complete and final segmentation of this thesis. Although in Haas et al. (2008) an average segmentation time needed for the rectum was given as 53 seconds without manual modification as well, compared to 141 seconds in this thesis for the complete segmentation, the quality was with a DSC of 52% considerably low, compared to 83% in this thesis. However, the result of 141 seconds for the complete rectum segmentation in this thesis is in

the range of the mentioned targeted time frame of 2 minutes for the automatic result without modifications of Haas et al. (2008).

Not taken into account for the time evaluation of the algorithmic segmentation is the option to skip certain slices where the change in the object outline is limited. This possibility can accelerate the segmentation in a large extent, since only a fraction of all slices has to be concerned.

Also not taken into account for qualitative evaluation of the algorithmic segmentation are the implemented tools of improvement regarding dragging of contour points and reinitialization. With those options the segmentation result can intuitively enhanced with fewer time effort.

It can be said that segmentation quality achieved with the presented algorithm is in accordance with common commercial and research results in medical imaging and equal to results achieved in daily clinical routine by clinicians. The use of a locally limited template and the inherent convergence to a local minimum of graph cuts prevents leaking. Together with the interactive methodology of the presented approach, user input parameters are limited to a minimum and make this approach superior to fully automatic methodologies. Equal quality results together with its time saving potential make this approach advantageous to manual segmentation.

5 Conclusion

The objective of this thesis was the development of a novel interactive graph-based segmentation methodology for the rectum/sigmoid colon as an Organ-At-Risk in the context of interstitial gynecological brachytherapy. The clinical gold standard for segmentation tasks is given by time and resource consuming slice-by-slice manual outlining of the region of interest. Although various fully automatic segmentation tools have been developed up to date, only few can guarantee robust results or are used in daily clinical routine. One drawback of automatic approaches is their complexity, limited flexibility and little provided user influence on the computed segmentation result where the algorithm is challenged. Thus, manual refinement of the computed segmentation is desirable and the motivation for the development of interactive segmentation approaches that allow direct and intuitive control over the segmentation result.

The presented methodology is based on graph networks and transforms the image segmentation problem into a simple, undirected graph. A minimal cut separates the object of interest from the background area. The graph network distribution across the image is determined by a dynamically adapting template whose shape is gained from user input in the beginning and obtained from the segmentation contour of a previous slice in succeeding slices. Interactive dragging of the graph network seed point in the object center allows to calculate various segmentations in the same slice and thus helps to find the optimal result. Slices where no strong object contour change occurs can be skipped and are interpolated later.

Evaluation of the algorithm was performed by comparing the computer assisted segmentation result with manual expert segmentations of the rectum/sigmoid colon and the bladder. The rectum/sigmoid colon yielded a DSC value of 83.85 ± 4.08 , the bladder 81.47 ± 4.48 . An intra-analysis between two sets of manual expert segmentation results yielded a DSC value of 83.97 ± 8.08 . Utilizing the presented methodology, the average time for the segmentation of one data set dropped from approximately 300s for one manually evaluated data set to 128 seconds for the rectum/sigmoid colon and 62 for the bladder utilizing the presented methodology.

Due to the star-like graph node distribution with the seed point at its origin, the algorithm was challenged where the object shape was particularly concave or convex. For future approaches multiple, equally distributed seed points could be utilized to guarantee an ideal areal sampling of the object and thus enhance the segmentation result quality.

Figures

- Figure 1: Illustration of the female pelvis: (1) anal canal (2) rectum, (3) sigmoid colon, (4) urethra, (5) vagina, (6) bladder, (7) uterus. Illustration based on (Drake et al., 2005) 10
- Figure 2: Illustration of the large intestine. It starts with the appendix (1) and cecum (2) in the right groin(A), continues as ascending colon (3) into the right flank (B) and right hypochondrium (C), crosses the abdomen (D) as transverse colon (4) into the left hypochondrium (E) and continues into the left flank (F) and left groin (G) as descending colon (5). From there it continues as sigmoid colon (6) and expands as rectum (7) into the anal canal (8) in the pubic (H). The umbilical (I) is not transversed by the large intestine. Illustration based on (Drake et al., 2005) 12
- Figure 3: Overview of the AMIGO suits: (1) MRI room, (2) Operating room, (3) PET-CT room (NCIGT, 2013) 13
- Figure 4: Applicator used in gynecological brachytherapy: (1) needles, (2) obturator, (3) template (© BWH-SPL, 2012)..... 14
- Figure 5: T2-weighted MR images recorded in the course of gynecological brachytherapy: (1) axial view, (2) sagittal view, (3) coronal view (© TUM-MIMED, 2012, MRI data from (Egger et al., 2012e)) 15
- Figure 6: General workflow of a radiology treatment plan; Clinical Target Volume (CTV), Organ-At-Risk (OAR); altered from (Bille and Schlegel, 2002)..... 16
- Figure 7: Schematic depiction of oncological and radiotherapeutic volumes in treatment planning: (1) Gross Tumor Volume (GTV), (2) Clinical Target Volume (CTV), (3) Irritated Volume (IV), (4) Planning Target Volume (PTV), (5) Organ-At-Risk, illustration based on (Kauffmann et al., 2006)..... 17
- Figure 8: Interstitial treatment planning: slice-by-slice optimization of radiation dose distribution on tumor (CTV) and sparing adjacent Organs-At-Risk, (1) Tumor, (2) Rectum/sigmoid colon, (3) Brachytherapy obturator, (4) 100% isodose line, (5) urinary bladder (illustrated from Kapur et al. (2012), data from Egger et al. (2012e)) 18
- Figure 9: Axial cross section of the anatomical structure of the lower female pelvis: (1) Rectum, (2) Vagina, (3) Urinary Bladder, (4) Fossa Ischionalis, (5) Gluteus Maximus, (6) Tuber Ischiadicum, (7) Os Femoris. Illustration based on (Schünke et al., 2005) 19
- Figure 10: Axial cross section of the lower female pelvis in a T2-weighted TSE image with anatomical structures: (1) Rectum, (2) Vagina & Obturator, (3) Urinary Bladder, (4) Tuber Ischiadicum, (5) Os Femoris, (6) Gluteus Maximus, (7) Fossa Ischionalis, (8) Gynecological Tumor, (9) Brachytherapy Needles (© TUM-MIMED, 2012, MRI data from (Egger et al., 2012e)) 20
- Figure 11: Depiction of the rectum/sigmoid colon in several different data sets of T2-weighted TSE MR images. Its appearance alters in shape, contrast and grey value distribution in no predictable manner (© TUM-MIMED, 2012, MRI data from (Egger et al., 2012e)) 21
- Figure 12: Sequence of a manual segmentation of the rectum/sigmoid colon by using the Draw Effect Tool included in 3D Slicer. The object in (1) is outlined slice by slice by a draw effect tool (2), (3) and the enclosed area is stored (4) (© TUM-MIMED, 2012, MRI data from (Egger et al., 2012e))..... 23
- Figure 13: After outlining of all respective organ slices, the volume is calculated and displayed: (1) Rectum/Sigmoid colon in blue, (2) Tumor in red, (3) Urinary Bladder in green (© BWH-SPL, 2012, MRI data from (Egger et al., 2012e))..... 24

Figure 14: Segmentation result of the rectum/sigmoid colon by the simple region growing algorithm: (1) Raw image, (2) First Seed Point, (3) Second Seed Point, (4) Segmentation Result (© TUM-MIMED, 2012, MRI data from (Egger et al., 2012e))	27
Figure 15: Segmentation result of the rectum/sigmoid colon by the Grow-Cut algorithm: (1) Raw Image, (2) Cropped Region of Interest, (3) Initialization Scribbles: Background (yellow), Object (green), (4) Segmentation Result (© TUM-MIMED, 2012, MRI data from (Egger et al., 2012e))	28
Figure 16: Segmentation of the rectum/sigmoid colon based on a data tree algorithm implemented in the 3D Slicer EM Segmenter tool. (1) Raw image and cropped region of interest, (2) Segmentation result of the region of interest (© TUM-MIMED, 2012, MRI data from (Egger et al., 2012e))	29
Figure 17: Example of a subjective contour (1) which can be found by an active contour approach (2). Altered from (Kass et al., 1988)	30
Figure 18: Segmentation of the rectum/sigmoid colon by an active contour model implemented in the 3D Slicer Robust Segmenter tool. (1) Raw image, (2) Cropped region of interest, (3) Initialization with 2 label maps, (background: yellow, object: green),(4) Segmentation result (© TUM-MIMED, 2012, MRI data from (Egger et al., 2012e))	31
Figure 19: Common interactive segmentation methodologies where the user provides input information by class scribbles: (1) object (green), background (yellow), (2) object (red), background (blue) (© TUM-MIMED, 2012, MRI data from (Egger et al., 2012e))	33
Figure 20: Illustration of interactive segmentation methodologies: (1) The user draws the object contour with fat brush tool, contour is automatically calculated within this trail, (2) User can improve automatic segmentation result (yellow line) by dragging object control points (yellow dots) (© TUM-MIMED, 2012, MRI data from (Egger et al., 2012e))	33
Figure 21: Object outline (1), drawn user contour (2), scaled user contour serving as template (3) (© TUM-MIMED, 2012)	40
Figure 22: Scaled contour serves as template for a segmentation (4), template position is determined by user-defined seed point (5), segmenation result is calculated (6) (© TUM-MIMED, 2012)	41
Figure 23: The calculated segmentation result (grey) (7) is scaled and serves as template for a next segmentation (blue) (8) (© TUM-MIMED, 2012)	41
Figure 24: User workflow of the presented interactive segmentation algorithm. First, the user traces the object contour. Second, the user skips to a next slice and determines if a deviation to the drawn contour occurs. If not, the user skips to a next slice. If yes, a seed point is set and cut calculated. If the result is satisfying the user skips to a next. If not, the user can either drag a contour point, drag the seed point or reinitialize by redrawing the object contour (© TUM-MIMED, 2012)	42
Figure 25: User traces object outline in slice nr. 0, (1) – (3) (© TUM-MIMED, 2012, MRI data from (Egger et al., 2012e))	43
Figure 26: User skips slices where no noteworthy deviation from the last contour occurs (© TUM-MIMED, 2012, MRI data from (Egger et al., 2012e))	43
Figure 27: Deviation from the previous contour (6), user sets seed point (7), segmentation is calculated (8), improvement by interactive dragging of seed point (9), new calculated segmentation result (10), interactive improvement of contour by dragging contour control point (11)) (© TUM-MIMED, 2012, MRI data from (Egger et al., 2012e))	44

Figure 28: Major deviation of the segmenation result from the object outline (12), reinitilization by drawing new object outline (13), new segmentation result (14)) (© TUM-MIMED, 2012, MRI data from (Egger et al., 2012e)).....	44
Figure 29: System overview: The C++ codes of the InteractiveCut and Boykov Library are implemented in a Microsoft Visual Studio project, which is embedded in a MeVisLab network. The MeVisLab network imports the image and manual segmentation and exports the object contour and voxelized 3D object (© TUM-MIMED, 2013)	45
Figure 30: Implemented MeVisLab® network consisting of 7 disctinct groups (© TUM- MIMED, 2013).....	46
Figure 31: Illustration of the implemented MeVisLab® network and information flow (© TUM-MIMED, 2013)	47
Figure 32: <i>User Contour</i> group (4) handling user interactions (© TUM-MIMED, 2013)	48
Figure 33: Marker group (2) handling all calculated marker outputs (© TUM-MIMED, 2013)	48
Figure 34: <i>Work Panel</i> (3) group, <i>InteractiveCut</i> modul and <i>Image load</i> modul (1) (© TUM- MIMED, 2013).....	49
Figure 35: State transition diagram of the implemented <i>InteractiveCut</i> source code (© TUM- MIMED, 2013).....	50
Figure 36: Illustration of a simple, undirected graph with $n = 5$ nodes and $m = 7$ edges (left) and a multi, directed graph with a parallel edge and a self loop, $n = 4$ nodes and $m = 6$ edges (right) (© TUM-MIMED, 2013)	52
Figure 37: A simple, undirected Graph G consisting of two connected components (1,2,3,4,5,6) and (7,8). Note that the G itself is not connected. The set of vertices (3,5,6) represent a subgraph of G (© TUM-MIMED, 2013).....	53
Figure 38: Example of a flow network with the <i>source</i> s and <i>sink</i> t . The flows and capacities are denoted by $f(v_x, v_y), c(v_x, v_y)$ (© TUM-MIMED, 2013).....	54
Figure 39: A cut C in the network example of Figure 38. The subset $S = \{s, 1, 2\}$ (red) is related to the source and the subset $T = \{3, t\}$ (green) is related to the sink. The cut-set C_{ST} consists of the set of edges $\{(2, 3), (3, 1), (1, t)\}$ and a capacity of $cap(S, T) = 2 + 2 = 4$ (© TUM-MIMED, 2013).....	55
Figure 40: Representation of the segmentation task as a graph network from a <i>source</i> s to a <i>sink</i> t . The image is seperated from the background through a minimal cut (© TUM- MIMED, 2013).....	56
Figure 41: Various graph template shapes, template (green and blue), seed point (white), segmenation result (yellow): Raw image (1), square template (2), triangle template (3), heart shaped template (4), dynamic template: user drawn or previous cut, in this case: user drawn template (red) (5) (© TUM-MIMED, 2013, MRI data from (Egger et al., 2012e))	57
Figure 42: Center of mass of different shapes. The position of the center of mass varies depending on the number of markers, although the spanned area stays equal (© TUM- MIMED, 2013).....	59
Figure 43: Illustration of the calculated mass center (green) and centroid of polygon (pink) of two different templates (© TUM-MIMED, 2013).....	60
Figure 44: A given template is scaled by a certain scaling factor s with the centroid of the polygon as the fixed point. The cut in (1) (yellow line) is taken as a template and scaled (2) (green line), which is then used as a template for a next cut (3) (green dots) (© TUM-MIMED, 2013, MRI data from (Egger et al., 2012e))	62
Figure 45: Graph node distribution from a given template and seed point position (© TUM- MIMED, 2013, MRI data from (Egger et al., 2012e)).....	63

Figure 46: Difference between the mass center (green) and the centroid (pink) (1), and corresponding node distribution based on the mass center (2) (© TUM-MIMED, 2013)	63
Figure 47: Illustration of three different graph weight types: xy-weights, z-weights and t-weights (© TUM-MIMED, 2013).....	65
Figure 48: Effect of two types of allocated T-weight capacities. In (1) the transition from intensity low to high areas is preferred, in (2) the transition from high to low intensities is preferred (© TUM-MIMED, 2013, MRI data from (Egger et al., 2012e))	67
Figure 49: Implemented 3 zone strategy for the allocation of t-weights. (1) Cut of a previous slice used as template, (2) Allocation of t-weights according to their zone (3) Resulting cut in zone II (© TUM-MIMED, 2013, MRI data from (Egger et al., 2012e))	68
Figure 50: Effect of graph collapsing (1), Segmentation result with implemented three zone strategy, collapsing prevented (2) (© TUM-MIMED, 2013, MRI data from (Egger et al., 2012e))	68
Figure 51: Illustration of the xy-weight implementation, the effect of the parameter Δ and the resulting costs. Exemplary $\Delta = 1$, $c_{xy} = \infty$: (1) $costs = 2 \times \infty$, (2) $costs = 2 \times \infty$, (3) $costs = 4 \times \infty$ (altered from (Egger, 2012))	69
Figure 52: Illustration of a completely connected and weight assigned graph network (© TUM-MIMED, 2013)	70
Figure 53: Set of object contours: (1) slices skipped, (2) skipped slices interpolated, (3) voxelized object, (4) voxelized object (yellow) superimposed in the patient anatomy (© TUM-MIMED, 2013)	71
Figure 54: Illustration of three different segmentation scenarios and their respective DSC : (1) $DSC(A,B) = 0\%$, (2) $DSC(A,B) = 2 \times V(A \cap B) / (V(A) + V(B))$, (3) $DSC = 100\%$ (© TUM-MIMED, 2013)	75
Figure 55: MeVisLab® network for the computation of the DSC and Hausdorff distance: (1) image loading and preprocessing, (2) DSC calculation, (3) visualization, (4) Hausdorff distance calculation (© TUM-MIMED, 2013)	75
Figure 56: Image loading and preprocessing of the calculated and manual segmentation result for the calculation of the DSC and HD (© TUM-MIMED, 2013)	76
Figure 57: Calculation of the DSC by predefined <i>Algorithm</i> modules (© TUM-MIMED, 2013)	76
Figure 58: Illustration of the Hausdorff distance for two sets A and B where $h(A,B) \neq h(B,A)$ (© TUM-MIMED, 2013)	77
Figure 59: MeVisLab® module used for calculation of the Hausdorff distance (© TUM-MIMED, 2013).....	77
Figure 60: Experimental evaluation of the InteractiveCut methodology with MeVisLab® (© TUM-MIMED, 2013, MRI data from (Egger et al., 2012e)).....	78
Figure 61: Segmentation results of the rectum/sigmoid colon. For (2) and (4) the red area indicates the InteractiveCut result, the green area the expert manual segmentation result. (5) voxelized manual segmentation, (6) voxelized InteractiveCut segmentation (© TUM-MIMED, 2013, MRI data from (Egger et al., 2012e))	81
Figure 62: A concave shape can challenge the algorithm due to its seed point rooted star-like node distribution. (2) manual segmentation (green), InteractiveCut segmentation (red), (3) and (4) illustrate strong bending of the object length axis where strong object shape changes can occur (© TUM-MIMED, 2013, MRI data from (Egger et al., 2012e))	82
Figure 63: Comparison of segmentation result performed manually (green) and with the InteractiveCut methodology (red). For (2), the dark, air filled area as well as the	

bright, contrast medium filled area is included in the segmentation (© TUM-MIMED, 2013, MRI data from (Egger et al., 2012e)).....	85
Figure 64: Due to the star like node distribution, segmentation challenges for the InteractiveCut algorithm occur where the object shape is strongly convex or concave (© TUM-MIMED, 2013, MRI data from (Egger et al., 2012e))	86

Glossary

AAM	Active Appearance Models
AMIGO	Advanced Multimodality Image Guided Operating Suite
BWH	Brigham & Women's Hospital, Boston, USA
DLL	Dynamic Link Library
DSC	Dice Similarity Coefficient
EBRT	External-Beam Radiation Therapy
GRE	Gradient Echo
GV	Grey Value
HC	Homogeneous Coordinates
HD	Hausdorff Distance
ICRU	International Commission on Radiation Units and Measurements
IGBT	Image Guided Brachytherapy
Nrrd	Nearly Raw Raster Data
OAR	Organ at Risk
RSS	Robust Statistics Segmenter
SP	Seed Point
SPL	Surgical Planning Laboratory, Harvard Medical School, Boston
TrueFisp	Fast Imaging With Steady State Precession
TSE	Turbo Spin Echo

Publication

Rectum Segmentation in MR-guided Gynecologic Brachytherapy Data

Tobias Lüddemann^a, Jan Egger^b

^a Technical University of Munich (TUM), Munich, Germany

^b University Hospital of Marburg (UKGM), Marburg, Germany



Background

Among all cancer types, gynecological malignancies - including endometrial, vaginal/vulvar and cervical cancers - belong to the 4th most frequent type of cancer among women [1]. Besides chemotherapy and external beam radiation, brachytherapy is the standard procedure for the treatment of these malignancies. In the progress of treatment planning, segmentation of the tumor as the target volume as well as segmentation of adjacent organs at risks is crucial to accomplish an optimal radiation distribution to the tumor while simultaneously preserve healthy tissue. This contribution presents the initial results of contouring the rectum with a novel interactive graph-based segmentation method based on a user-defined template.

Methods

The proposed method uses a graph-based segmentation scheme [2] and extends it to an interactive approach (named *Interactive-Cut*) with a user-defined template. In summary, the scheme creates a directed 2D graph, followed by the minimal cost closed set computation on the graph [3], resulting in an optimal outlining of the rectum. Thereby, the graph's center can be interactively dragged to compute a further segmentation and optimize the result. Figure 1 demonstrates the interactive segmentation process: original dataset (A), interactive moving of the graph's center (B-E) with *real-time* feedback of the rectum contour (red) and resulting segmentation (F) after a satisfying outline of the rectum has been achieved.

Results

Six intraoperative T2-weighted magnetic resonance imaging (MRI) datasets acquired with a Siemens 3T scanner at the Brigham and Women's Hospital (BWH) have been used for this initial study [4, 5]. Segmentation of the rectum could successfully be performed in all cases. For visual side-by-side inspection Figure 2 presents three manual segmentations (A, C and E, blue) and the corresponding interactive segmentations (B, D and F, red). For all segmentations the same template has been used (blue dots in the right images) and no parameter definitions were required from the user. However, a satisfying rectum contour could always be found within seconds for every plane.

Conclusion

In this contribution, we tested a novel interactive graph-based approach - called *Interactive-Cut* - to segment the rectum with a user-defined template. Our long-term objective is to support the time-consuming process of manual rectum outlining for gynecologic brachytherapy and our initial 2D results show already promising results. Areas of future work include a comprehensive evaluation via the Dice Similarity Coefficient (DSC) and an extension of the algorithm to 3D.

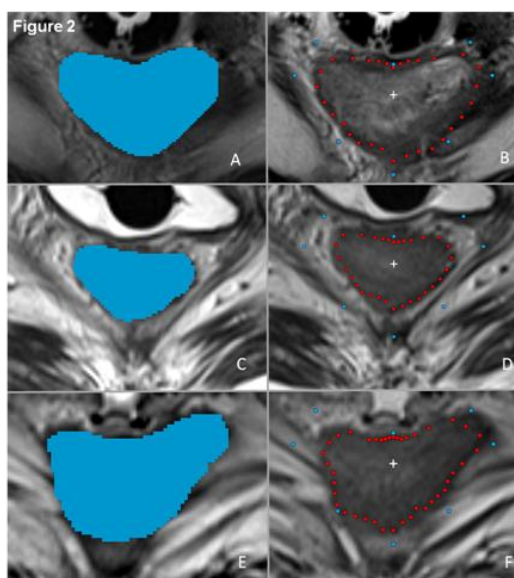
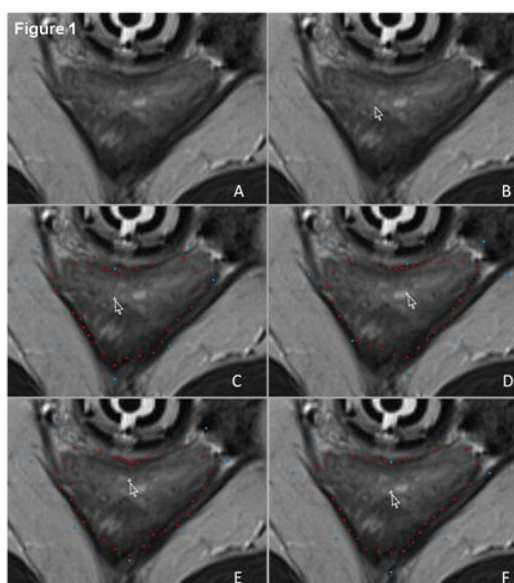
References

1. American Cancer Society, Cancer Statistics, 2012.
2. J. Egger, et al. Template-Cut: A Pattern-Based Segmentation Paradigm. Sci Rep., Nature Publishing Group (NPG), 2012;2:420. Epub 2012 May 24.
3. Y. Boykov & V. Kolmogorov. An Experimental Comparison of Min-Cut/Max-Flow Algorithms for Energy Minimization in Vision. IEEE Transactions on Pattern Analysis and Machine Intelligence, 26(9), pp. 1124-1137, 2004.
4. J. Egger, et al. GYN Data Collection. NCIGT, online available: <http://www.spl.harvard.edu/publications/item/view/2227>
5. T. Kapur, et al. 3-T MR-guided brachytherapy for gynecologic malignancies. Magn Reson Imaging., 2012 Aug 13. [Epub ahead of print]

Acknowledgements

The authors would like to thank Neha Agrawal for performing the manual segmentations. The authors would also like to thank Fraunhofer MeVis in Bremen, Germany, for their collaboration and especially Professor Hahn for his support.

The British Gynaecological Cancer Society Annual Scientific Meeting in conjunction with the Irish Gynaecological Cancer Society
The Waterfront, Belfast, Northern Ireland • 20th - 21st June, 2013.



Bibliography

- ARTAN, Y. Interactive Image Segmentation Using Machine Learning Techniques. Computer and Robot Vision (CRV), 2011 Canadian Conference on, 2011. IEEE, 264-269.
- BABALOLA, K., PATENAUDE, B., ALJABAR, P., SCHNABEL, J., KENNEDY, D., CRUM, W., SMITH, S., COOTES, T., JENKINSON, M. & RUECKERT, D. 2008. Comparison and evaluation of segmentation techniques for subcortical structures in brain MRI. *Medical Image Computing and Computer-Assisted Intervention–MICCAI 2008*, 409-416.
- BILLE, J. & SCHLEGEL, W. 2002. *Medizinische Strahlenphysik : mit 37 Tabellen*, Berlin [u.a.], Springer.
- BIRKBECK, N., COBZAS, D., JAGERSAND, M., MURTHA, A. & KESZTYUES, T. An interactive graph cut method for brain tumor segmentation. Applications of Computer Vision (WACV), 2009 Workshop on, 2009. IEEE, 1-7.
- BLAKE, A., ROTHER, C., BROWN, M., PEREZ, P. & TORR, P. 2004. Interactive image segmentation using an adaptive GMMRF model. *Computer Vision-ECCV 2004*, 428-441.
- BOURKE, P. 2007. Calculating the area and centroid of a polygon, 1988. Accessed on February, 11.
- BOYKOV, Y. & KOLMOGOROV, V. 2004. An experimental comparison of min-cut/max-flow algorithms for energy minimization in vision. *Pattern Analysis and Machine Intelligence, IEEE Transactions on*, 26, 1124-1137.
- BOYKOV, Y. & VEKSLER, O. 2006. Graph cuts in vision and graphics: Theories and applications. *Handbook of mathematical models in computer vision*. Springer.
- BOYKOV, Y. Y. & JOLLY, M.-P. Interactive graph cuts for optimal boundary & region segmentation of objects in ND images. Computer Vision, 2001. ICCV 2001. Proceedings. Eighth IEEE International Conference on, 2001. IEEE, 105-112.
- CABEZAS, M., OLIVER, A., LLADÓ, X., FREIXENET, J. & BACH CUADRA, M. 2011. A review of atlas-based segmentation for magnetic resonance brain images. *Computer methods and programs in biomedicine*, 104, e158-e177.
- CHANG, Q., ZHANG, B. & LIU, R. Texture analysis method for shape-based segmentation in medical image. Image and Signal Processing (CISP), 2011 4th International Congress on, 2011. IEEE, 1146-1149.
- COMMUNITY, S. 2013. *Simple Region Growing* [Online]. Available: http://www.slicer.org/slicerWiki/index.php/Modules:Simple_Region_Growing-Documentation-3.6 [Accessed March 7th 2013].
- CORSO, J. J., SHARON, E., DUBE, S., EL-SADEN, S., SINHA, U. & YUILLE, A. 2008. Efficient multilevel brain tumor segmentation with integrated bayesian model classification. *Medical Imaging, IEEE Transactions on*, 27, 629-640.

- CRUM, W. R., CAMARA, O. & HILL, D. L. 2006. Generalized overlap measures for evaluation and validation in medical image analysis. *Medical Imaging, IEEE Transactions on*, 25, 1451-1461.
- DAVIES, E. R. 2012. Computer and machine vision : theory, algorithms, practicalities. 4. ed. Amsterdam [u.a.]: Elsevier.
- DELONG, A., GORELICK, L., SCHMIDT, F., VEKSLER, O. & BOYKOV, Y. Interactive segmentation with super-labels. *Energy Minimization Methods in Computer Vision and Pattern Recognition*, 2011. Springer, 147-162.
- DIESTEL, R. 2005. Graph theory. 2005. Springer-Verlag.
- DING, L. & YILMAZ, A. 2010. Interactive image segmentation using probabilistic hypergraphs. *Pattern Recognition*, 43, 1863-1873.
- DORIA D., C. S. 2010. Interactive Graph Cut Segmentation. *The Insight Journal*.
- DRAKE, R. L., VOGL, W., MITCHELL, A. W. M. & GRAY, H. 2005. *Gray's anatomy for students : [online access + interactive extras ; studentconsult.com]*, Philadelphia, Pa. [u.a.], Elsevier.
- EGGER, J. 2012. Intraoperative Visualisierung multimodaler Daten in der Neurochirurgie.
- EGGER, J., AGRAWAL, N., BLEVINS, T., FARHAT, N., PERNELLE, G., CHEN, X., GAO, Y., WELLS, W., PENZKOFER, T., KAPUR, T. & VISWANATHAN, A. 2012a. Segmentation of Pelvic Structures for Gynecological Brachytherapy.
- EGGER, J., COLEN, R. R., FREISLEBEN, B. & NIMSKY, C. 2012b. Manual refinement system for graph-based segmentation results in the medical domain. *J Med Syst*, 36, 2829-39.
- EGGER, J., DUKATZ, T., FREISLEBEN, B. & NIMSKY, C. 2012c. Ein semiautomatischer Ansatz zur Flächenbestimmung von Wirbeln in MRT-Aufnahmen. *Bildverarbeitung für die Medizin 2012*, 274-279.
- EGGER, J., FREISLEBEN, B., NIMSKY, C. & KAPUR, T. 2012d. Template-cut: a pattern-based segmentation paradigm. *Sci Rep*, 2, 420.
- EGGER, J., KAPUR, T., FEDOROV, A., PIEPER, S., MILLER, J. V., VEERARAGHAVAN, H., FREISLEBEN, B., GOLBY, A. J., NIMSKY, C. & KIKINIS, R. 2013. GBM Volumetry using the 3D Slicer Medical Image Computing Platform. *Scientific Reports*, 3.
- EGGER, J., KAPUR, T. & VISWANATHAN, A. 2012e. *GYN Data Collection* [Online]. NCIGT. Available: <http://www.spl.harvard.edu/publications/item/view/2227> [Accessed November 17th, 2012].
- ELSA, D. A., OLIVIER, C., EMMANUEL, M., ENDER, K., LAURENT, C. & HUGUES, D. 2010. Glioma Dynamics and Computational Models: A Review of Segmentation, Registration, and In Silico Growth Algorithms and their Clinical Applications.

- ELSAYES, K. M., STAVETEIG, P. T., NARRA, V. R., LEYENDECKER, J. R., LEWIS, J. S. & BROWN, J. J. 2006. MRI of the peritoneum: spectrum of abnormalities. *American journal of roentgenology*, 186, 1368-1379.
- FORD, L. & FULKERSON, D. 1962. Flows in networks. 1962. *Princeton U. Press, Princeton, NJ*.
- GAO, Y., KIKINIS, R., BOUIX, S., SHENTON, M. & TANNENBAUM, A. 2012. A 3D Interactive Multi-object Segmentation Tool using Local Robust Statistics Driven Active Contours. *Medical Image Analysis*.
- GIBBONS, A. 1985. *Algorithmic graph theory*, Cambridge University Press.
- GODSE, A. 2008. *Computer Graphics*, Technical Publications
- GREENE, F. L., COMPTON, C. C., FRITZ, A. G., SHAH, J. P. & WINCHESTER, D. P. 2006. *AJCC cancer staging atlas*, Springer New York, NY.
- HAAS, B., CORADI, T., KUNZ, P., SCHOLZ, M. & REDDICK, R. C. Smart Segmentation™—A White Paper.
- HAAS, B., CORADI, T., SCHOLZ, M., KUNZ, P., HUBER, M., OPPITZ, U., ANDRÉ, L., LENGKEEK, V., HUYSKENS, D. & VAN ESCH, A. 2008. Automatic segmentation of thoracic and pelvic CT images for radiotherapy planning using implicit anatomic knowledge and organ-specific segmentation strategies. *Physics in medicine and biology*, 53, 1751.
- HECKBERT, P. S. 1994. *Graphics gems IV*, Boston etc., AP Professional.
- HEIMANN, T., THORN, M., KUNERT, T. & MEINZER, H. 2004. New methods for leak detection and contour correction in seeded region growing segmentation. *International Archives of Photogrammetry and Remote Sensing*, 35.
- HUYSKENS, D., MAINGON, P., VANUYTSEL, L., REMOUCHAMPS, V., ROQUES, T., DUBRAY, B., HAAS, B., KUNZ, P., CORADI, T. & BÜHLMAN, R. 2008. a qualitative and a quantitative analysis of an auto-segmentation module for prostate cancer.
- JACKOWSKI, M. P., GOSHTASBY, A. & SATTER, M. Interactive tools for image segmentation. *Medical Imaging'99*, 1999. International Society for Optics and Photonics, 1063-1074.
- JÄHNE, B. 2005. *Digitale Bildverarbeitung*, Springer.
- JESORSKY, O., KIRCHBERG, K. J. & FRISCHHOLZ, R. W. Robust face detection using the hausdorff distance. *Audio-and video-based biometric person authentication*, 2001. Springer, 90-95.
- JUNGnickel, D. 2005. *Graphs, networks and algorithms*, Springer.
- JÜRGENLIEMK-SCHULZ, I. M., LANG, S., TANDERUP, K., DE LEEUW, A., KIRISITS, C., LINDEGAARD, J., PETRIC, P., HUDEJ, R. & PÖTTER, R. 2010. Variation of treatment planning parameters (D90 HR-CTV, D_{2cc} for OAR) for

- cervical cancer tandem ring brachytherapy in a multicentre setting: Comparison of standard planning and 3D image guided optimisation based on a joint protocol for dose-volume constraints. *Radiotherapy and Oncology*, 94, 339-345.
- KALINIC, H. Atlas-based image segmentation: A Survey.
- KAMDI, S. & KRISHNA, R. 2011. Image Segmentation and Region Growing Algorithm. *International Journal*, 1.
- KAPUR, T., EGGER, J., DAMATO, A., SCHMIDT, E. J. & VISWANATHAN, A. N. 2012. 3-T MR-guided brachytherapy for gynecologic malignancies. *Magnetic Resonance Imaging*.
- KASS, M., WITKIN, A. & TERZOPOULOS, D. 1988. Snakes: Active contour models. *International journal of computer vision*, 1, 321-331.
- KAUFFMANN, G. W., MOSER, E., SAUER, R. & BOCK, R. 2006. *Radiologie*, München, Elsevier.
- KHOTANLOUA, H., COLLIOTB, O., ATIFC, J. & BLOCHA, I. 2009. 3D brain tumor segmentation in MRI using fuzzy classification, symmetry analysis and spatially constrained deformable models. *Fuzzy Sets and Systems*, 160, 1457-1473.
- KNAUER, U. 2011. *Algebraic Graph Theory: Morphisms, Monoids and Matrices*, De Gruyter.
- KOLMOGOROV, V. 2010. *Max-flow/Min-cut* [Online]. Available: <http://vision.csd.uwo.ca/code/> [Accessed November 14th, 2013].
- KULKARNI, M. & NICOLLS, F. 2009. Interactive image segmentation using graph cuts. *Pattern Recognition Association of South Africa*, 99-104.
- LECHSEL, G. 2007. Interactive Segmentierungsverfahren im Rahmen der adaptiven Strahlungstherapie.
- LETTEBOER, M. M., OLSEN, O. F., DAM, E. B., WILLEMS, P. W., VIERGEVER, M. A. & NIESSEN, W. J. 2004. Segmentation of tumors in magnetic resonance brain images using an interactive multiscale watershed algorithm. *Academic radiology*, 11, 1125-1138.
- LI, K., WU, X., CHEN, D. Z. & SONKA, M. 2006. Optimal surface segmentation in volumetric images-a graph-theoretic approach. *Pattern Analysis and Machine Intelligence, IEEE Transactions on*, 28, 119-134.
- MANNAN, F. Interactive Image Segmentation.
- MARTINEZ, F., ACOSTA, O., DRÉAN, G., SIMON, A., HAIGRON, P., DE CREVOISIER, R. & ROMERO, E. 2012. Segmentation of pelvic structures from planning CT based on a statistical shape model with a multiscale edge detector and geometrical likelihood measures. *Image-Guidance and Multimodal Dose Planning in Radiation Therapy*, 26.
- MAZONAKIS, M., DAMILAKIS, J., VARVERIS, H., PRASSOPOULOS, P. & GOURTSOYIANNIS, N. 2001. Image segmentation in treatment planning for prostate

- cancer using the region growing technique. *The British Journal of Radiology*, 74, 243-248.
- MEASUREMENTS, I. C. O. R. U. 1999. *Prescribing, recording, and reporting photon beam therapy*, International Commission on Radiation Units and Measurements.
- MEVISLAB. 2012. *MeVisLab Reference Manual* [Online]. Available: www.mevislab.de.
- MORRIS, D. 1998. *Cancer: A comprehensive clinical guide*, Taylor & Francis.
- MUNDT, A. J., YASHAR, C. M. & MELL, L. K. 2011. *Gynecologic Cancer*, Demos Medical Publishing.
- NCIGT. 2013. *AMIGO - IGTWeb* [Online]. Available: <http://www.ncigt.org/pages/AMIGO> [Accessed January 15th, 2013].
- NEUBERT, A., FRIPP, J., SHEN, K., SALVADO, O., SCHWARZ, R., LAUER, L., ENGSTROM, C. & CROZIER, S. Automated 3D Segmentation of Vertebral Bodies and Intervertebral Discs from MRI. *Digital Image Computing Techniques and Applications (DICTA)*, 2011 International Conference on, 2011. IEEE, 19-24.
- NICKISCH, H., ROTHER, C., KOHLI, P. & RHEMANN, C. Learning an interactive segmentation system. *Proceedings of the Seventh Indian Conference on Computer Vision, Graphics and Image Processing*, 2010. ACM, 274-281.
- PALEY, M. & ROS, P. 1997. MRI of the gastrointestinal tract. *European radiology*, 7, 1387-1397.
- PASQUIER, D., LACORNERIE, T., VERMANDEL, M., ROUSSEAU, J., LARTIGAU, E. & BETROUNI, N. 2007. Automatic segmentation of pelvic structures from magnetic resonance images for prostate cancer radiotherapy. *International journal of radiation oncology, biology, physics*, 68, 592-600.
- PEKAR, V., MCNUTT, T. R. & KAUS, M. R. 2004. Automated model-based organ delineation for radiotherapy planning in prostatic region. *International journal of radiation oncology, biology, physics*, 60, 973.
- PHAN, R. & ANDROUTSOS, D. Interactive video GrowCut: A semi-automated video object segmentation framework using cellular automata. *Electrical and Computer Engineering (CCECE)*, 2011 24th Canadian Conference on, 2011. IEEE, 000081-000084.
- POHL, K. M., BOUIX, S., NAKAMURA, M., ROHLFING, T., MCCARLEY, R. W., KIKINIS, R., GRIMSON, W. E. L., SHENTON, M. E. & WELLS, W. M. 2007. A hierarchical algorithm for MR brain image parcellation. *Medical Imaging, IEEE Transactions on*, 26, 1201-1212.
- PRASTAWA, M., BULLITT, E., HO, S. & GERIG, G. 2004. A brain tumor segmentation framework based on outlier detection. *Medical Image Analysis*, 8, 275-283.
- ROTHER, C., KOLMOGOROV, V. & BLAKE, A. Grabcut: Interactive foreground extraction using iterated graph cuts. *ACM Transactions on Graphics (TOG)*, 2004. ACM, 309-314.

- SCHMIDT, F. R., TOPPE, E. & CREMERS, D. Efficient planar graph cuts with applications in computer vision. *Computer Vision and Pattern Recognition*, 2009. CVPR 2009. IEEE Conference on, 2009. IEEE, 351-356.
- SCHÜNKE, M., SCHULTE, E., SCHUMACHER, U., RUDE, J., VOLL, M. & WESKER, K. 2005. *Prometheus : LernAtlas der Anatomie*, Stuttgart [u.a.], Thieme.
- SIEGEL, R. D. N. A. J. 2012. *Cancer Statistics 2012. CA: a cancer journal for clinicians*. American Cancer Society.
- SINDEYEV, M. & KONUSHIN, V. A novel interactive image matting framework. *GraphiCon*, 2008. 41-45.
- SLICER-COMMUNITY. 2013a. *3D Slicer* [Online]. Available: <http://www.slicer.org/> [Accessed March 7th 2013].
- SLICER-COMMUNITY. 2013b. *EM Segmenter* [Online]. Available: <http://slicer.spl.harvard.edu/slicerWiki/index.php/Modules:EMSegmenter-3.6> [Accessed March 13th 2013].
- SLICER-COMMUNITY. 2013c. *Robust Statistics Segmenter* [Online]. Available: <http://www.slicer.org/slicerWiki/index.php/Modules:RobustStatisticsSegmentation-3.6> [Accessed March 12th 2013].
- STEGER, S. & SAKAS, G. 2012. Fist: Fast interactive segmentation of tumors. *Abdominal Imaging. Computational and Clinical Applications*, 125-132.
- TORTORA, G. J. & DERRICKSON, B. H. 2008. *Principles of anatomy and physiology*, Wiley.
- VARIAN, I. 2013. *Eclipse - Radiation Therapy Planning* [Online]. Available: http://www.varian.com/us/oncology/radiation_oncology/eclipse [Accessed March 5th 2013].
- VEZHNEVETS, V. & KONOUCHE, V. 2005. "GrowCut"-Interactive Multi-Label ND Image Segmentation By Cellular Automata.
- VISWANATHAN, A. N. 2011. *Gynecologic radiation therapy novel approaches to image-guidance and management*, Heidelberg, Springer.
- VISWANATHAN, A. N. & ERICKSON, B. A. 2010. Three-dimensional imaging in gynecologic brachytherapy: a survey of the American Brachytherapy Society. *International Journal of Radiation Oncology* Biology* Physics*, 76, 104-109.
- WANG, F., WANG, X. & LI, T. Efficient label propagation for interactive image segmentation. *Machine Learning and Applications*, 2007. ICMLA 2007. Sixth International Conference on, 2007. IEEE, 136-141.
- WELS, M., CARNEIRO, G., APLAS, A., HUBER, M., HORNEGGER, J. & COMANICIU, D. 2008. A discriminative model-constrained graph cuts approach to fully automated pediatric brain tumor segmentation in 3-D MRI. *Medical Image Computing and Computer-Assisted Intervention-MICCAI 2008*, 67-75.

- WEST, D. B. 2001. *Introduction to graph theory*, Prentice hall Englewood Cliffs.
- ZOU, K. H., WARFIELD, S. K., BHARATHA, A., TEMPANY, C., KAUS, M. R., HAKER, S. J., WELLS III, W. M., JOLESZ, F. A. & KIKINIS, R. 2004. Statistical validation of image segmentation quality based on a spatial overlap index^{> 1}: scientific reports. *Academic radiology*, 11, 178-189.
- ZUKIC, D., VLASÁK, A., DUKATZ, T., EGGER, J., HORÍNEK, D., NIMSKY, C. & KOLB, A. Segmentation of Vertebral Bodies in MR Images. *Vision, Modeling & Visualization*, 2012. The Eurographics Association, 135-142.